

Electronic Structure of Selected Materials  
by Means of the QSGW method  
within the LAPW+LO framework

Dissertation zur Erlangung des akademischen Grades  
Doctor rerum naturalium (Dr. rer. nat.)

im Fach: Physik

Spezialisierung: Theoretische Physik

eingereicht an der

Mathematisch-Naturwissenschaftlichen Fakultät  
der Humboldt-Universität zu Berlin

von

MSc. Frau Nora Salas-Illanes  
geboren am 16.10.1984 in Santiago de Chile

Präsidentin der Humboldt-Universität zu Berlin  
Prof. Dr.-Ing. Dr. Sabine Kunst

Dekan der Mathematisch-Naturwissenschaftlichen Fakultät  
Prof. Dr. Elmar Kulke

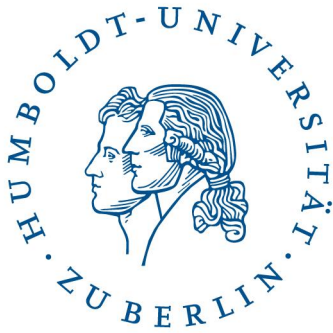
---

Gutachter/innen:

- 1.
- 2.
- 3.

Tag der mündlichen Prüfung:





**Electronic Structure of Selected Materials  
by Means of the QSGW method  
within the LAPW+LO framework**

Nora Salas-Illanes

under supervision of

Univ. Prof. Dr. Dr. h.c. Claudia Draxl

Dissertation submitted in part fulfillment of the requirements  
for the degree of Doctor of Philosophy (PhD) at  
Humboldt-Universität zu Berlin, October 2018





I declare that I have completed the thesis independently using only the aids and tools specified. I have not applied for a doctor's degree in the doctoral subject elsewhere and do not hold a corresponding doctors degree. I have taken due note of the Faculty of Mathematics and Natural Sciences PhD Regulations, published in the Official Gazette of Humboldt-Universitt zu Berlin no. 42 on July 11 2018.

Ich erkläre, die Dissertation selbstständig und nur unter Verwendung der angegebenen Hilfen und Hilfsmittel angefertigt zu haben. Ich habe mich nicht anderwärts um einen Doktorgrad in dem Promotionsfach beworben und besitze keinen entsprechenden Doktorgrad. Die Promotionsordnung der Mathematisch-Naturwissenschaftlichen Fakultät, veröffentlicht im Amtlichen Mitteilungsblatt der Humboldt-Universität zu Berlin Nr. 42 am 11. Juli 2018, habe ich zur Kenntnis genommen.

Nora Salas-Illanes (2018)

The copyright of this thesis rests with the author and is made available under a Creative Commons Attribution Non-Commercial No Derivatives licence. Researchers are free to copy, distribute or transmit the thesis on the condition that they attribute it, that they do not use it for commercial purposes and that they do not alter, transform or build upon it. For any reuse or redistribution, researchers must make clear to others the licence terms of this work.



## Summary

Materials shape the modern world: they appear everywhere in our daily life. To respond to new challenges, we need to understand and explore materials, bringing us a step closer to ground-breaking technologies. Our goal is to comprehend what governs the material's properties, in order to tailor them to meet our needs. Many properties, *e.g.* bandgaps, electronic density distribution, and chemical bonds, are determined by the electronic structure. In quantum mechanics, we find many answers to the description of the electronic structure, but we need to translate this knowledge into practice.

Most predictions regarding materials follow from computational physics, in particular density-functional theory (DFT). This theory, based on quantum mechanics, returns ground-state properties, such as the ground-state electron density. However, it fails to provide excited-state energies and, consequently, bandgaps. Therefore, to describe excited states we have to recourse to a higher degree of theory. One can make use of *many-body perturbation theory* (MBPT). MBPT takes into account many-body effects explicitly, whereas in the practical implementations of DFT, these interactions are approximated by a mean-field where particles move independently from each other. Within MBPT, the most popular framework is the *GW* approximation (GWA), where electrons are described as *quasiparticles* (QP). These are electrons “dressed” with their interaction with all other electrons, screening the electrostatic repulsion between electrons, and giving rise to the *screened* Coulomb interaction  $W$ . This screening affects the propagation of the QP, described by a one-body Green's function  $G$ . The difference in energy between a non-interacting particle and a QP is called the self-energy,  $\Sigma$ . In GWA, the product of the Green function  $G$  and  $W$ , returns  $\Sigma$ , leading to the true excitation energy of the QP. In principle, the GWA is self-consistent, where all quantities are related to each other, directly or indirectly. Unfortunately,  $G$  is unknown and therefore, it is usually approximated by a non-interacting propagator operator  $G_0$ .

Alternatively to self-consistent *GW*, DFT results can be corrected once by adding a term containing  $\Sigma$ , known as  $G_0W_0$ . However, the electronic structure calculated through  $G_0W_0$  shows a starting-point dependence with respect to the initial DFT results. Self-consistency can solve this source of error.

This PhD project consists in the implementation of the self-consistent quasiparticle *GW* (QSGW) in the **exciting** code. This software package uses the all-electron linearized augmented plane-wave (LAPW) method, treating every electron on equal footing. Starting from DFT, the QSGW method optimizes the one-particle Hamiltonian through a self-consistent search for an optimized exchange-correlation potential. At the end of the iterative process, the QSGW method provides eigenfunctions and eigenvalues of the QPs. Considering nine crystalline solids, we present their electronic structure by means of QSGW. We present the bandstructures and density of state diagrams, comparing QSGW results to DFT and  $G_0W_0$  results. In addition, we study the electronic charge density and wavefunction in selected materials.



## Zusammenfassung

Materialien formen die moderne Welt: Sie umgeben uns in unserem alltäglichen Leben. Auf neue Herausforderungen zu reagieren erfordert, dass wir Materialien verstehen und erforschen, und uns so schrittweise bahnbrechenden Technologien nähern. Unser Ziel dabei ist zu verstehen, wodurch die Materialeigenschaften bestimmt sind, um diese dann nach unseren Bedürfnissen maßzuschneidern. Viele Materialeigenschaften wie Bandlücken, Elektronendichteverteilung und chemische Bindungen werden durch elektronische Zustände bestimmt. Die Quantenmechanik hält die Antworten zur Beschreibung der elektronischen Struktur bereit, aber es bedarf einer Übersetzung dieses Wissens in die Praxis.

Die meisten Vorhersagen in Bezug auf Materialien entstammen der rechnergestützten Physik, insbesondere der Dichtefunktionaltheorie (DFT). Diese auf der Quantenmechanik beruhende Theorie ermittelt Grundzustandseigenschaften wie z.B. die Grundzustandselektronendichte. Sie kann jedoch keine Energien —und damit auch keine Bandlücken— von angeregten Zuständen liefern. Um angeregte Zustände zu beschreiben, bedarf es daher einer höherstufigen Theorie. Die *Vielteilchen-Störungstheorie* (MBPT) lässt sich zu diesem Zwecke nutzen. Die MBPT enthält explizit die Wechselwirkungen der Elektronen untereinander, während in der DFT-Implementierung diese Wechselwirkungen durch ein mittleres Feld, in welchem sich die Teilchen unabhängig voneinander bewegen, genähert werden.

Im Rahmen von MBPT ist das üblichste Verfahren die *GW*-Näherung (GWA), worin Elektronen als *Quasiteilchen* (QP) beschrieben werden. Diese QP sind Elektronen, die die Wechselwirkungen mit allen anderen Elektronen mit sich tragen. Diese Wechselwirkung schirmt die elektrostatische Abstoßung zwischen den Elektronen ab und erzeugt somit eine *abgeschirmte* Coulomb-Wechselwirkung. Dieser Abschirmungseffekt beeinflusst die Bewegung der QP, was sich durch die Einteilchen-Greenfunktion  $G$  beschreiben lässt. Der Energieunterschied zwischen einem nicht-wechselwirkenden Teilchen und einem QP wird als Selbstenergie  $\Sigma$  bezeichnet. In GWA ergibt sich  $\Sigma$  als Produkt aus  $G$  und  $W$  und führt zu der wahren Anregungsenergie von QP. In Prinzip ist GWA selbstkonsistent und alle Größen stehen entweder direkt oder indirekt in Beziehung zueinander.  $G$  ist jedoch leider unbekannt und wird üblicherweise durch den nicht-wechselwirkenden Propagator  $G_0$  genähert.

Alternativ zu selbstkonsistentem *GW* kann DFT durch Addition eines Terms korrigiert werden, welcher  $\Sigma$  enthält, was mit  $G_0W_0$  bezeichnet wird. Allerdings zeigt die mit  $G_0W_0$  berechnete elektronische Struktur eine Anfangswertabhängigkeit in Bezug auf die ursprünglichen DFT-Ergebnisse. Selbstkonsistenz kann diese Fehlerquelle beheben.

Diese Doktorarbeit beinhaltet die Implementierung von selbstkonsistentem Quasiteilchen-*GW* (QSGW) im `exciting` Code. Dieses Software-Paket benutzt die Linearized-Augmented-Plane-Wave-Methode (LAPW), welche alle Elektronen gleichberechtigt behandelt. Beginnend mit DFT optimiert die QSGW-Methode den Einteilchen-Hamiltonoperator durch eine selbstkonsistente Suche eines optimierten Austausch-Korrelationspotentials. Am Ende des iterativen Prozesses liefert die QSGW-Methode Eigenfunktionen und Eigenwerte der QP. Wir präsentieren mit QSGW ermittelte elektronische Strukturen von neun kristallinen Festkörpern. Wir präsentieren die zugehörigen

Bandstrukturen und Zustandsdichtediagramme und vergleichen anhand dieser die QSGW-Ergebnisse mit Ergebnissen von DFT und  $G_0W_0$ . Zusätzlich untersuchen wir die elektronische Ladungsdichte und Wellenfunktion in ausgewählten Materialien.

## Acknowledgements

First and foremost, I want to thank Prof. Claudia Draxl. She was the instigator of this project and her excitement immediately got me on board. Many thanks to Dimitrii Nabok, enabler of the  $G_0W_0$  implementation in **exciting** and my direct support during these years. I also appreciate the help of Andris Gulans, whose contribution proved essential to the improvement of my project.

Bettina Menzel played a key role by keeping a candid eye on the development of my PhD thesis. On this note, I want to turn to the International Max-Planck Research School (IMPRS) for Functional Interfaces. Their funding made possible all of what is exposed in this thesis. Even more, the IMPRS supported my participation in conferences and soft skill seminars.

I want to thank Prof. Mark von Schilfgaard. He introduced me to the method which gives its name to this dissertation, welcomed me in his group for a two-week visit in London and patiently responded to my questions.

To my working group at the Humboldt University, a big thank you for your support!

To my friend Laila Rosato, who brought some of her creative skills into the graphics of this thesis. My friends Denise Misleh, Lorena Pereiras and Fernanda Valdes. Among those close friends I earned from my Physics studies, I would like to thank Mattias Saita, Federico Guerra and Andreas Guidi. A heartfelt thank you to all my friends in different countries, who kept track, tirelessly, of my progress.

Last but not least, I thank my family. Not only deeply supportive and movingly unconditional, but also a proud bunch of very fine people.



Dedicado a Don Julio y Doña Loreto



# Contents

Summary	1
Zusammenfassung	3
Acknowledgements	5
<b>1 Introduction</b>	<b>13</b>
<b>I Theory</b>	<b>15</b>
<b>2 Electronic-Structure Theory</b>	<b>17</b>
2.1 Electronic Many-Body Problem . . . . .	17
2.2 Independent-Particle Approximation . . . . .	19
2.2.1 Hartree-Fock Approximation . . . . .	20
2.2.2 Density-Functional Theory . . . . .	22
2.2.3 Generalized Kohn-Sham Scheme . . . . .	26
<b>3 Many-Body Perturbation Theory</b>	<b>27</b>
3.1 Weakly Interacting Fermions . . . . .	27
3.2 Propagation function in a one-body quantum theory . . . . .	28
3.3 Connecting Non-Interacting and Interacting Systems . . . . .	31
3.3.1 Diagrammatic expansion of $G$ . . . . .	32
3.3.2 Equation of motion for $G$ . . . . .	34
3.4 Hedin's Equations . . . . .	35
3.4.1 One-shot GWA . . . . .	37
<b>4 Quasiparticle Self-Consistent GW</b>	<b>39</b>
4.1 Self-Consistent GW . . . . .	39
4.2 Energy Minimization . . . . .	40
4.3 Independent or Interacting Systems? . . . . .	43
<b>5 Linearized Augmented Planewaves</b>	<b>45</b>
5.1 APW Basis . . . . .	45
5.2 LAPW basis . . . . .	47
5.3 (L)APW+LO basis . . . . .	48
5.4 Core States . . . . .	48
5.5 Mixed Basis Set . . . . .	48
<b>II Results</b>	<b>53</b>
<b>6 Implementation</b>	<b>55</b>
6.1 General Implementation Scheme . . . . .	55
6.2 GWA Equations in Matrix Form . . . . .	56
6.2.1 Coulomb Potential . . . . .	57
6.2.2 Dielectric Matrix . . . . .	60
6.3 Calculation of the Self-Energy . . . . .	60
6.3.1 Correlation Self-Energy . . . . .	61
6.3.2 Exchange Self-Energy . . . . .	62

---

6.3.3	Singularities of the Self-Energy . . . . .	63
6.4	Optimized Hamiltonian in QSGW . . . . .	63
6.5	Parallelization . . . . .	64
6.6	Computational Requirements . . . . .	64
<b>7</b>	<b>Electronic Structure of Selected Materials</b>	
	<b>by Means of QSGW</b>	<b>67</b>
7.1	Materials . . . . .	67
7.2	Computational Details . . . . .	68
7.2.1	Set-up of Local Orbitals . . . . .	69
7.3	Bandstructures and Densities of States . . . . .	70
7.4	Effect of Off-diagonal Matrix Elements . . . . .	80
7.5	Starting-Point Dependence . . . . .	83
7.6	Charge Density . . . . .	85
7.7	Quasiparticle Wavefunctions . . . . .	87
<b>8</b>	<b>Conclusions and Outlook</b>	<b>91</b>
	<b>Appendices</b>	<b>95</b>
<b>A</b>	<b>The Variational Method</b>	<b>97</b>
A.1	Variational Principle . . . . .	97
A.2	Linear Variational Problem . . . . .	97
<b>B</b>	<b>Second Quantization and Pictures in Quantum Mechanics</b>	<b>99</b>
B.1	Fock Space . . . . .	99
B.2	Creation and Annihilation Operators . . . . .	99
B.3	Schrödinger Picture . . . . .	100
B.4	Heisenberg Picture . . . . .	101
B.5	Interaction Picture . . . . .	101
<b>C</b>	<b>Spherical Harmonics</b>	<b>103</b>
<b>E</b>	<b>Pade's Approximants</b>	<b>104</b>
	<b>List of Tables</b>	<b>105</b>
	<b>List of Figures</b>	<b>106</b>
	<b>Bibliography</b>	<b>108</b>





# Chapter 1

## Introduction

Materials play a major role in our daily life. Thus, exploring and understanding their properties and functionalities is not only scientifically exciting, but also an important topic in view of possible applications. Macroscopic properties as well as functions of materials are, to a large extent, governed by what happens on the electronic scale. Prerequisite for any application and possible tailoring of materials is the basic understanding of phenomena on this scale. This is where theoretical physics comes in, particularly quantum mechanics, as it can provide valuable insight into the fundamental particle interactions therein. However, theory requires solving complex equations, which humans alone cannot overcome. To bridge theory and practice, computational materials science develops algorithms, which are designed to solve these complex equations.

Among the rich variety of physical phenomena in materials, many are determined by the electronic structure. Characteristic to every material, it reveals information on the energy of electrons, their effective masses and/or the conductivity and polarizability of the material. This PhD project focuses on the electronic structure of crystalline solids. Studying the electronic structure, we face the many-body Schrödinger equation (SE) which, except from a few simple cases, is impossible to solve exactly, neither analytically nor numerically. The difficulty of its solution lies in the large number of variables. Therefore, it has been necessary to develop alternative methods which can solve the many-body problem.

A first approximation to the many-body SE is to treat the ions as static charged particles, known as the *Born-Oppenheimer approximation*, hence the only variables are the electronic coordinates [1]. Even if this approximation simplifies the many-body problem to a many-electron problem, the solution remains unknown. Hohenberg and Kohn demonstrated that the knowledge of the electron density is enough to derive the properties of a system of electrons and nuclei in a solid, therefore the energy of the system can be written as a functional of the density [2]. This way, Hohenberg and Kohn established the *density-functional theory* (DFT). For the past decades, DFT has been the most popular numerical method to calculate properties of many-electron systems [3, 4]. In practice, DFT is implemented within the Kohn-Sham (KS) scheme, which decomposes the many-body problem into one-body equations, where we select the  $N$  solutions representing the state of a non-interacting, *fictitious* particles with lowest energies. In this scheme, the electron-electron interaction is approximated to a mean-field exchange-correlation potential,  $v_{xc}$ . The KS equations are solved iteratively, updating the electronic density after every iteration until the change in density, and hence energy, between consecutive iterations is below some tolerance. For a large number of materials, DFT provides accurate results for ground-state properties, in particular those derived from the total energy. In theory, DFT only describes the groundstate (GS) and this theory is not justified for high-energy states. In addition, the system of fictitious particles presented by the KS scheme does not provide real one-electron energies. Despite these drawbacks, the band structure calculated with DFT gives a first insight in the electronic structure of the system.

In order to access the one-electron energies for excited states, we have to go beyond DFT. For this purpose, one can use *many-body perturbation theory* (MBPT). Within MBPT, electrons are described as *quasiparticles* (QP). These are electrons “dressed” with their interaction with all other electrons, which translates into a screening of the electrostatic repulsion between charges, turning the strong Coulomb interaction into a weak screened Coulomb interaction,  $W$ . The propagation of the QP, described by a one-body Green’s function  $G$ , is affected by this screening. The QP acquires an energy, called the *self-energy*  $\Sigma(\omega)$ , due to the perturbation it causes in the system

---

when moving through the solid. Unfortunately, the explicit formula for the full self-energy is very complex. In order to describe QPs, we express this dynamical potential through approximations. The state-of-the-art in MBPT is implementing the *GW approximation* (GWA) for quasiparticle calculations [5]. In GWA,  $\Sigma$  is the integral of the product  $GW$ .

Central to the GWA, the Green's function provides the true propagation of the electron upon its removal from or addition to the system in the GS [6]. Unfortunately,  $G$  is a complicated object defined by the eigenstates of the interacting QP, which are unknown. In practice,  $G$  of the interacting QP is approximated to a single-particle, non-interacting Green's function,  $G_0$ . Usually,  $G_0$  is calculated using the wavefunctions and energies given by an independent particle scheme. This initial Green's function can be updated by solving the Hedin's equations iteratively. Alternatively,  $G_0$ , together with the screened Coulomb interaction  $W$ , can provide a self-energy  $\Sigma$ , which serves as a perturbative correction to the KS eigenvalues, known as one-shot  $GW$  or  $G_0W_0$  [7]. The eigenvalues from the independent particle scheme can be regarded as good starting point for the perturbative calculations. The  $G_0W_0$  method has proven success for calculating band gaps. However,  $G_0$  build upon KS results will depend on the calculated energies and eigenstates provided by the chosen  $v_{xc}$ . The resulting quasiparticle bandgaps calculated through the  $G_0W_0$  method show considerable variations depending on the underlying approximation to  $v_{xc}$ . This phenomenon is known as *starting-point dependence* [8, 9].

A solution to the starting-point dependence is performing the *quasiparticle self-consistent GW* (QS $GW$ ) method [10–12]. In the realm of GWA, we express all operators, *e.g.*,  $W$  and  $\Sigma$ , based on the interacting  $G$ , although this is unknown. The QS $GW$  method pursues the search for the “best” possible candidate for  $G_0$ , that is the closest to the interacting  $G$ . To carry out the optimization of the Green's function, we make use of the QS $GW$  method to calculate an optimized exchange-correlation potential self-consistently, replacing the approximated  $v_{xc}$  in the Hamiltonian. This iterative optimization of the Hamiltonian—and consequently of the Green's functions—corresponds to the minimization of the difference between the Hamiltonian of the true interacting system and that of non-interacting particles. The strength of this method lies in its consideration of conservation laws, and its practical recipe using already implemented schemes, like KS and  $G_0W_0$ , to build the iterative procedure.

This PhD project consists in the implementation of QS $GW$  in the **exciting** code. In order to describe the one-electron states, this all-electron package uses the basis set as prescribed in the linearized augmented planewave (LAPW) method. The LAPW treats all electrons on equal footing, without the need for pseudopotentials. The first part of this thesis consists in four chapters introducing the theory required for the QS $GW$  method. Chapter 2 presents the many-body problem in general, followed by approximations and concepts used in electronic structure theory. Chapter 3 introduces MBPT and its main concepts, *e.g.*, what a QP is and what the self-energy of the QP embodies. In this chapter, we explain Hedin's equations, leading to the GWA, and the  $G_0W_0$  method. Chapter 4 is dedicated to the QS $GW$  method, in particular the physical and mathematical justification behind the optimized exchange-correlation potential in QS $GW$ , which leads to the optimized  $G_0$ . Closing the theory part, Chapter 5 explains the APW and LAPW methods. It also introduces the concept of local orbitals and the basis set for excited-state calculations.

The implementation of QS $GW$  in **exciting**, presented in detail in Chapter 6, enables the calculation of the electronic structure of a wide range of solids. This goal was successfully met by a careful study of nine semiconductors and insulators, presented in Chapter 7. The results provide (i) features in the electronic structures by means of the all-electron basis, (ii) new findings in view of QS $GW$  within the LAPW method, which is seldom present in the literature, (iii) insight in the role of off-diagonal terms in the self-energy, and (iii) optimized wavefunctions and densities for the considered materials. These aspects allow for a complete study of the electronic structure of the sample set. Having successfully tested our implementation, we can expand the use of the QS $GW$  method in **exciting** to cover other materials in future studies. Finally, we suggest future improvements for our implementation.

# Part I

## Theory



## Chapter 2

# Electronic-Structure Theory

In quantum mechanics, the time-independent Schrödinger equation (SE) describes the stationary states of a many-body system of interacting electrons and nuclei:

$$\hat{\mathcal{H}}\Phi(r, R) = \mathcal{E}\Phi(r, R). \quad (2.1)$$

The Hamiltonian operator  $\hat{\mathcal{H}}$  acts on the wavefunction of the total system,  $\Phi(r, R)$ , returning its energy,  $\mathcal{E}$  [13]. The operator and the wavefunction (WF) depend on both the ensemble of the spatial coordinates of the  $N$  electrons,  $r \equiv \{\mathbf{r}_i, i = 1 \dots N\}$ , and of the  $N'$  nuclei,  $R \equiv \{\mathbf{R}_I; I = 1 \dots N'\}$ . In this dissertation, vectors appear in bold font, where  $\mathbf{r}_i$  and  $\mathbf{R}_I$  denote the position of electron  $i$  and nucleus  $I$ , respectively.

Unfortunately, the solution of the Schrödinger equation involves  $3N + 3N'$  variables, usually a very large number, thus unmanageable. Furthermore, the storage of the complete information regarding the WF, a high dimensional object, is an almost impossible task. The following section shows how science has taken on the challenge to describe many-body systems in solids.

### 2.1 Electronic Many-Body Problem

A common attempt at describing many-particle system in practice is to conduct numerical calculations. As an example, we may employ a mesh storing each *discretized* coordinate in real space entering the WF. Neglecting spin and nuclear coordinates and assuming the WF to be real, for the case of  $N$  electrons in a mesh holding 20 grid points we need  $20^{3N}$  values to describe the electronic WF on the mesh. Illustrating the burden of storage for the case of the oxygen atom, with its 8 electrons, it would require  $1.67 \cdot 10^{31}$  entries for the mentioned grid [14]. Counting 8 bytes of memory per floating-point entry, this amounts to a total of  $\approx 1.34 \cdot 10^{32}$  bytes, or  $1.34 \cdot 10^{20}$  petabytes (PB). Just for comparison, as per today the largest supercomputer in the USA has a 120 PB storage capacity for its file system [15]. The search for an alternative formulation of the SE is imperative! It has therefore been necessary to develop and efficiently implement mathematical methods which can provide approximate solutions to such eigenvalue problems.

The Hamiltonian of the total system,  $\hat{\mathcal{H}}$ , is an Hermitian operator, which, in units of Hartree, can be written as:

$$\hat{\mathcal{H}} = - \sum_i \frac{\nabla_i^2}{2} + \frac{1}{2} \sum_{i \neq j} \frac{1}{|\mathbf{r}_i - \mathbf{r}_j|} - \sum_{i,I} \frac{Z_I}{|\mathbf{r}_i - \mathbf{R}_I|} + \frac{1}{2} \sum_{I \neq J} \frac{Z_I Z_J}{|\mathbf{R}_I - \mathbf{R}_J|} - \sum_I \frac{\nabla_I^2}{2M_I}. \quad (2.2)$$

For nucleus  $I$ , the nuclear mass is  $M_I$ , and  $Z_I$  the atomic number. In Eq. 2.2, the first and second term are the electronic kinetic energy  $\hat{T}$  and the electron-electron interaction  $\hat{U}$ . The third and fourth term are the Coulomb attraction between electrons and nuclei  $\hat{V}_{eN}$ , and the Coulomb repulsion between nuclei  $\hat{V}_{NN}$ . The last term represents the nuclear kinetic energy  $\hat{T}_N$ .

Many contributions throughout the last century made possible to tackle the complexity of the SE. The time-line in Fig. 2.1 depicts a selection of such contributions, all of which introduce theories and approximated solutions to the many-body problem. As for the vast majority of computational

calculations at present, these seminal works are essential to this project. Endless number of books discuss in detail the scientific breakthroughs displayed below, therefore I restrict this section to expose the main ideas guided by their chronological appearance [4, 16–18].

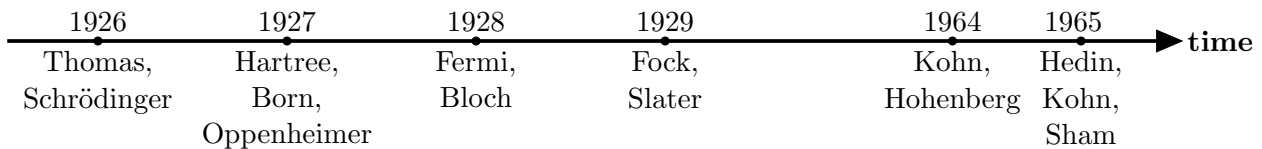


Figure 2.1: Time-line of selected contributions to quantum calculations.

Thanks to its general form, Equation 2.2 is valid for liquid, gas or solid systems. In the latter case, condensed matter physics deals with ions that are *barely moving* in contrast to the surrounding electrons. Taking this into consideration, Max Born and Robert Oppenheimer introduced in 1927 the *Born-Oppenheimer approximation* [1]. The physical meaning behind this approximation is that the time evolution of the nuclei, being much slower than the electronic one, is decoupled from the electronic degrees of freedom. In this approximation, nuclei in solids remain at fixed positions, being the nuclei kinetic energy,  $\hat{T}_N$ , considerably lower than the electronic kinetic energy. The repulsion between nuclei,  $\hat{V}_{NN}$ , becomes then a constant in the Hamiltonian. Summing a constant to an operator increases its eigenvalue by that constant, leaving the eigenfunctions of the operator unchanged. On the other hand, nuclei are assumed to reside in the potential energy surface arising from the fast-moving electrons. Therefore, the total system can be split in two parts: the electronic and nuclear system. The total wavefunction is re-written as a product of an electronic,  $\Psi(r; R)$ , and a nuclear,  $X(R)$ , function:  $\Phi(r, R) = \Psi(r; R) X(R)$ . Based on this approximation, the total Born-Oppenheimer Hamiltonian is written as the sum of the nuclear and electronic Hamiltonian:  $\hat{\mathcal{H}} = \hat{H}_N + \hat{H}_e$ . The present work regards exclusively the electronic Hamiltonian (the subscript  $e$  is left out) and the SE for the electronic system is:

$$\hat{H}(\mathbf{r}_1, \mathbf{r}_2, \dots, \mathbf{r}_N; R) \Psi(\mathbf{r}_1, \mathbf{r}_2, \dots, \mathbf{r}_N; R) = \left[ \hat{T}(r) + \hat{V}(r; R) + \hat{U}(r) \right] \Psi(r; R) = E \Psi(r; R). \quad (2.3)$$

The operators in the electronic Hamiltonian are:

$$\hat{T} = -\frac{1}{2} \sum_i \nabla_i^2 \quad (2.4)$$

$$\hat{V} = \sum_i \hat{v}(\mathbf{r}_i; R) \quad (2.5)$$

$$\hat{U} = \frac{1}{2} \sum_{i \neq j} \frac{1}{|\mathbf{r}_i - \mathbf{r}_j|}, \quad (2.6)$$

where the sums run over all electrons. The operator  $\hat{U}$  represents the internal potential energy given by the Coulomb interaction between electrons. Though the operator  $\hat{V}$  can include any other potential, in this work we only regard the *lattice potential* given by the electron-nucleii interaction. Omitting in the next the explicit dependence on  $R$ , the solution to the electronic Hamiltonian eigenvalue problem is the electronic wavefunction  $\Psi(r)$ , which is normalized, in Dirac's notation, as  $\langle \Psi | \Psi \rangle = 1$ .

The first two terms in the Hamiltonian in Eq. 2.3 do not include interactions among electrons; *i.e.*, together they describe *independent non-interacting particles* exactly. Neglecting electronic interactions, the  $N$ -electron problem boils down to  $N$  single-particle problems, where the  $i$ -th electron in state  $\psi_i(\mathbf{r})$  has energy  $\epsilon_i$ , and the total energy of the non-interacting system is  $E^{\text{IP}} = \sum_i \epsilon_i$ . It would be convenient, however, to include the electron-electron interaction, while keeping the spirit of an independent single-particle description.

the main task of *Electronic-structure theory* is to solve Eq. 2.3. The next section describes the different methods and approximations that (i) solve the all-electron problem through a single-particle approach and (ii) allow for the inclusion of the electron-electron interaction.

## 2.2 Independent-Particle Approximation

In the same year as Born's and Oppenheimer's innovation came to light, Douglas Hartree proposed a self-consistent scheme to solve the SE of a many-electrons system within a single-particle framework [19]. In this paper, he introduced a local effective potential, an approximation to the classic Coulomb potential via a mean-field potential, called *Hartree potential*,  $\hat{v}_H(\mathbf{r})$ . It expresses the electrostatic potential which originates from the electronic density,  $\rho(\mathbf{r})$ . Solving the Poisson equation for this potential  $\nabla^2 \hat{v}_H(\mathbf{r}) = -4\pi\rho(\mathbf{r})$  gives:

$$\hat{v}_H(\mathbf{r}) = \int \frac{\rho(\mathbf{r}')}{|\mathbf{r} - \mathbf{r}'|} d\mathbf{r}'. \quad (2.7)$$

This potential fits in the independent-particle picture, since each electron interacts with this electrostatic potential independently. Together with Eqs. 2.4 and 2.5, we define the effective single-particle Hamiltonian,  $\hat{h}^{\text{eff}}(\mathbf{r})$ , which acting on a single-particle state,  $\psi_{n\mathbf{k}}(\mathbf{r})$ , returns its Hartree-eigenvalue,  $\epsilon_{n\mathbf{k}}^H$ :

$$\hat{h}^{\text{eff}}(\mathbf{r}) \psi_{n\mathbf{k}}(\mathbf{r}) = \left[ -\frac{\nabla_{\mathbf{r}}^2}{2} + \hat{v}(\mathbf{r}) + \hat{v}_H(\mathbf{r}) \right] \psi_{n\mathbf{k}}(\mathbf{r}) = \epsilon_{n\mathbf{k}}^H \psi_{n\mathbf{k}}(\mathbf{r}), \quad (2.8)$$

where  $\mathbf{k}$  is a vector in the unit cell of the reciprocal lattice (first Brillouin zone) and  $n$  the band index. The solutions of the Schrödinger-like equation above are the independent one-electron wavefunctions  $\psi_{n\mathbf{k}}(\mathbf{r})$ .

In crystals, all electrons are subject to the same external potential, where the atoms are organized in a determined fashion, repeating this pattern along the three dimensions in space. In 1928, Felix Bloch added new information to the electronic problem looking at this ordered atomic structure in solids [20]. The *Bloch theorem* says that *if* the potential acting on the single electron follows the periodicity of the lattice, the single-particle eigenfunction  $\psi_{n\mathbf{k}}(\mathbf{r})$  of the effective Hamiltonian can be written as:

$$\psi_{n\mathbf{k}}(\mathbf{r}) = e^{i\mathbf{k}\cdot\mathbf{r}} u_{n\mathbf{k}}(\mathbf{r}), \quad (2.9)$$

with a function  $u_{n\mathbf{k}}(\mathbf{r})$  whose periodicity is that of the lattice. Thus, we can describe the one-electron states as Bloch functions. Yet, the final aim is describing the *total* electronic wavefunction,  $\Psi(r)$ . It is useful to describe  $\Psi(r)$  in terms of single-particle functions  $\psi_{\nu}(\mathbf{r})$ , inserting band index and wave number in the subindex  $\nu$ .

John Slater's contribution in 1929 targets the description of the total electronic WF for an independent particle system, such as the one treated in the Hartree approximation. He proposed a new construction of the WF to properly include the antisymmetry of fermions—the permutation of electronic coordinates brings about a sign change in the total wavefunction—, respecting Pauli's principle, *i.e.*, every one-electron state has a unique set of quantum numbers [21]. In this new architecture of  $\Psi(r)$ , the occupied one-electron functions  $\psi_{\nu}(\mathbf{r})$  are arranged as columns in a matrix. Making up the rows we find the coordinates  $\mathbf{x}_i$  consisting of spin,  $\sigma_i$ , and space coordinates,  $\mathbf{r}_i$ , collected in the set:  $x \equiv \{\mathbf{x}_i = (\mathbf{r}_i, \sigma_i), i = 1, \dots, N\}$ . For  $N$  electrons, the total wavefunction,

$\Psi_{\text{SD}}(x)$ , is the resulting determinant of the matrix:

$$\Psi_{\text{SD}}(x) = \frac{1}{\sqrt{N!}} \begin{vmatrix} \psi_1(\mathbf{x}_1) & \psi_2(\mathbf{x}_1) & \cdots & \psi_N(\mathbf{x}_1) \\ \psi_1(\mathbf{x}_2) & \psi_2(\mathbf{x}_2) & \cdots & \psi_N(\mathbf{x}_2) \\ \vdots & & & \\ \psi_1(\mathbf{x}_N) & \psi_2(\mathbf{x}_N) & \cdots & \psi_N(\mathbf{x}_N) \end{vmatrix} \quad (2.10)$$

The prefactor  $(\sqrt{N!})^{-1}$  is the normalization factor. Each  $\psi_\nu(\mathbf{r})$  is a spin orbital, *i.e.*, a product of the spatial wavefunction and the spin functions. Taking only the spatial part —called *spatial orbital*— into account the probability of finding the electron in the volume element  $d\mathbf{r}$  centered at  $\mathbf{r}$  is  $|\psi_\nu(\mathbf{r})|^2 d\mathbf{r}$ . The set of spatial orbitals is assumed to be orthonormal, the same holds for the spin functions. Having two equal columns in the determinant Eq. 2.1 corresponds to having two electrons occupying the same spin orbital. In this case the determinant is zero, thereby respecting Pauli's principle.

To this point, the developments to solve the independent-particle SE are: (i) including an approximation to the Coulomb interaction via  $\hat{v}_{\text{H}}(\mathbf{r})$ , (ii) incorporating translational symmetry based on Bloch's theorem, and (iii) combining the single-particle functions  $\psi_\nu(\mathbf{r})$  to build the total electronic state using Slater's determinant,  $\Psi_{\text{SD}}(x)$ . The coming sections revise the main two methods to solve the single-particle SE, yet accounting for electronic interactions via mean-field approximations.

### 2.2.1 Hartree-Fock Approximation

In 1929, Vladimir Fock extended the quantum description of the electronic system by including exchange effects in the single-particle Hamiltonian [22]. The exchange operator follows automatically by inserting  $\Psi(x)$  in Eq. 2.3 as a single Slater determinant, constructed by occupied one-electron spin orbitals  $\psi_\nu(\mathbf{x})$ .<sup>1</sup> Fock, already acquainted of Hartree's work, proposed to include the exchange operator in the self-consistent-field method developed by his colleague. This additional potential alongside with the Hartree potential form the basis of what is known as *Hartree-Fock approximation* (HFA).

Exchange effects emerge as the total WF is antisymmetrized, meaning its square amplitude  $|\Psi(x)|^2$  remains invariant to the exchange of space and spin coordinates of two electrons. To reveal the origin of the *exchange* potential, lets take two electrons with coordinates  $\mathbf{r}_1$  and  $\mathbf{r}_2$  —neglecting spin for the rest of the chapter— occupying two orbitals:  $\psi_\nu$  and  $\psi_\mu$ . The Slater determinant for this system is

$$\Psi_{\text{SD}}(r) = \frac{1}{\sqrt{2}} [\psi_\nu(\mathbf{r}_1) \psi_\mu(\mathbf{r}_2) - \psi_\mu(\mathbf{r}_1) \psi_\nu(\mathbf{r}_2)].$$

The expectation value of the Coulomb interaction in Eq. 2.6 with respect to this two-body WF returns four terms. Considering that  $|\mathbf{r}_1 - \mathbf{r}_2| = r_{12} = r_{21}$ , we can interchange integration variables and we reduce the terms to two:

$$\langle \Psi | r_{12}^{-1} | \Psi \rangle = \int \int \psi_\nu^*(\mathbf{r}_1) \psi_\mu^*(\mathbf{r}_2) r_{12}^{-1} \psi_\nu(\mathbf{r}_1) \psi_\mu(\mathbf{r}_2) d\mathbf{r}_1 d\mathbf{r}_2 - \int \int \psi_\nu^*(\mathbf{r}_1) \psi_\mu^*(\mathbf{r}_2) r_{12}^{-1} \psi_\mu(\mathbf{r}_1) \psi_\nu(\mathbf{r}_2) d\mathbf{r}_1 d\mathbf{r}_2.$$

This basic example can be extended for larger determinants, as the operator always acts pairwise on the orbitals. The first term on the right-hand side is the energy given by the averaged interaction between the electron occupying orbital  $\psi_\nu$  and the electron in  $\psi_\mu$ , taking all possible  $\mathbf{r}_1, \mathbf{r}_2$  coordinates. The second double-integral term is the electron exchange energy. For N electrons, each pairwise

<sup>1</sup>Unoccupied orbitals, *i.e.*, excited states, can also be included. For simplicity, this introductory section only takes occupied states into account.

Coulomb interaction contributes with both terms. Unsurprisingly, the kernel in the first double-integral is the Hartree potential  $\hat{v}_H(\mathbf{r})$  introduced in the previous section. Unlike  $\hat{v}_H(\mathbf{r})$ , the second term in the right-hand side is the *exchange* energy of electrons between two orbitals and it does not have a classical counterpart. This last integral is related to the exact-exchange operator or *Fock operator*,  $\hat{\Sigma}_x(\mathbf{r}, \mathbf{r}')$ . Finally, these operators acting on an electron in state  $\psi_\mu(\mathbf{r})$  read:

$$\hat{v}_H(\mathbf{r})\psi_\mu(\mathbf{r}) = \sum_\nu \int \frac{|\psi_\nu(\mathbf{r}')|^2}{|\mathbf{r} - \mathbf{r}'|} \psi_\mu(\mathbf{r}) d\mathbf{r}' = \int \frac{\rho(\mathbf{r}')}{|\mathbf{r} - \mathbf{r}'|} \psi_\mu(\mathbf{r}) d\mathbf{r}' \quad (2.11)$$

$$-\hat{\Sigma}_x(\mathbf{r}, \mathbf{r}')\psi_\mu(\mathbf{r}) = \sum_\nu \int \frac{\psi_\nu^*(\mathbf{r}')\psi_\mu(\mathbf{r}')}{|\mathbf{r} - \mathbf{r}'|} \psi_\nu(\mathbf{r}) d\mathbf{r}'. \quad (2.12)$$

The action of  $\hat{v}_H(\mathbf{r})$  on an electron has an unphysical component, because by interacting with the electronic density, the electron also interacts with itself; this is called *self-interaction error*. But if the exchange and the Hartree potentials act on the electron in  $\psi_\nu(\mathbf{r}')$ , both terms cancel and cure this error.

Often in quantum physics, the Hamiltonian includes operators that are either *local* or *non-local*. An example of the former is  $\hat{v}_H(\mathbf{r})$ , whereas  $\hat{\Sigma}_x(\mathbf{r}, \mathbf{r}')$  is a standard case of the latter. We can calculate the value of the Hartree energy of an electron in  $\psi_\mu(\mathbf{r})$  just by taking a specific point  $\mathbf{r}$ , while  $\hat{\Sigma}_x(\mathbf{r}, \mathbf{r}')$  acting on  $\psi_\mu(\mathbf{r})$  depends on the values of  $\psi_\mu$  throughout space; not only at  $\mathbf{r}$ . Non-locality appears also in the coming chapters and will prove essential to describe delocalized electronic states.

In practice, the one-electron orbital set  $\{\psi_\nu\}$  in the HFA is approximated, so the expectation value of the many-electron Hartree-Fock Hamiltonian,  $\mathcal{H}^{\text{HF}}$ , leads to an upper-bound of the ground-state energy  $E_0$ :

$$E_0 \leq \langle \Psi_0^{\text{HF}} | \mathcal{H}^{\text{HF}} | \Psi_0^{\text{HF}} \rangle = \sum_\nu \int \psi_\nu^*(\mathbf{r}) \left[ -\frac{1}{2} \nabla^2 + v(\mathbf{r}) \right] \psi_\nu(\mathbf{r}) d\mathbf{r} + \frac{1}{2} \sum_{\nu, \mu} \left[ \int \psi_\nu^*(\mathbf{r}) \psi_\mu^*(\mathbf{r}') \frac{1}{|\mathbf{r} - \mathbf{r}'|} \psi_\nu(\mathbf{r}) \psi_\mu(\mathbf{r}') d\mathbf{r} d\mathbf{r}' - \int \psi_\nu^*(\mathbf{r}) \psi_\mu^*(\mathbf{r}') \frac{1}{|\mathbf{r} - \mathbf{r}'|} \psi_\nu(\mathbf{r}') \psi_\mu(\mathbf{r}) d\mathbf{r} d\mathbf{r}' \right], \quad (2.13)$$

where  $\Psi_0^{\text{HF}}(r)$  is the Slater determinant for the ground state in the HFA. The one-half prefactor in front of the square bracket makes up for the double counting of the exchange and Hartree potential between two electrons.

To find the most adequate candidates for the single-particle WF—or spin-orbitals—we minimize Eq. 2.13. As a minimization constrain, the one-electron wavefunctions are subject to orthonormalization:  $\int \psi_\nu^*(\mathbf{r}) \psi_\mu(\mathbf{r}) d\mathbf{r} = \langle \nu | \mu \rangle = \delta_{\nu\mu}$ . Based on the variational method and Lagrange's principle, we define a functional of the spin-orbitals

$$\mathcal{L}[\{\psi\}] = E_0[\{\psi\}] - \sum_{\nu, \mu} \epsilon_{\mu\nu} (\langle \nu | \mu \rangle - \delta_{\nu\mu}),$$

where  $\epsilon_{\nu\mu}$  serves as Lagrange multiplier and  $\delta_{\nu\mu}$  is the Kronecker delta. We minimize  $\mathcal{L}$  by varying the spin orbitals  $\psi_\mu \rightarrow \psi_\mu + \delta\psi_\mu$  and setting the variation on  $\mathcal{L}$  to zero. This does not immediately lead to a standard eigenvalue equation, but through a unitary transformation of the spin-orbitals we

attain a canonical form of the integro-differential Hartree-Fock equation:<sup>2</sup>

$$\left[ -\frac{1}{2}\nabla^2 + \hat{v}(\mathbf{r}) + \hat{v}_H(\mathbf{r}) \right] \psi_\nu^{\text{HF}}(\mathbf{r}) + \int \hat{\Sigma}_x(\mathbf{r}, \mathbf{r}') \psi_\nu^{\text{HF}}(\mathbf{r}') d\mathbf{r}' = \epsilon_\nu^{\text{HF}} \psi_\nu^{\text{HF}}(\mathbf{r}), \quad (2.14)$$

where the term in brackets is  $\hat{h}^{\text{eff}}(\mathbf{r})$  in Eq. 2.8. The operators are functionals of the Hartree-Fock spin-orbitals,  $\psi_\nu^{\text{HF}}(\mathbf{r})$ , which, in turn, are the solutions to these equations. Due to this non-linearity, the problem has to be solved iteratively.

### 2.2.2 Density-Functional Theory

HFA, while treating exchange exactly, it does not account for the correlation between electrons. This section presents an alternative approach to the wavefunction-based HFA, the *density-functional theory* (DFT). This theory maps the many-electron problem into an electronic-density problem.

Since Llewellyn Thomas's and Enrico Fermi's article in 1926, it took many decades to pick up the early development of density functionals to solve the SE [24, 25]. In 1964, Pierre Hohenberg and Walter Kohn delivered a theorem which is the formal justification for the DFT [2]. This theorem does not lay out any form of the single-particle Hamiltonian, but a year later Walter Kohn and Lu Jeu Sham proposed a practical scheme to obtain an effective single-particle SE based on DFT. Currently, there are various software packages aiming at solving scientific problems based on DFT. The success of DFT ascribes to its simplicity and the approximations of the exchange-correlation potentials (sections Sec. 2.2.2 and Sec. 2.2.2). We first explain the theoretical background, followed by an introduction to the one-particle equations in the Kohn-Sham scheme.

#### Hohenberg-Kohn Theorem

According to the Hohenberg-Kohn theorem, all properties of an electron system can be derived from the electronic ground-state density. For  $N$  electrons, the particle density  $\rho(\mathbf{r})$  is the number of electrons per volume at the position  $\mathbf{r}$  in space:

$$\rho(\mathbf{r}) = N \int |\Psi(\mathbf{r}, \mathbf{r}_2, \dots, \mathbf{r}_N)|^2 d\mathbf{r}_2 \cdots d\mathbf{r}_N. \quad (2.15)$$

The density is constrained to the total number of electrons by  $\int \rho(\mathbf{r}) d\mathbf{r} = N$ . Through a simple and elegant proof, Hohenberg and Kohn stated the one-to-one correspondence between  $\rho(\mathbf{r})$  in the groundstate (GS) and the external potential,  $\hat{V}$ . Equivalently, we can say that if the density changes, it also modifies the potential  $\hat{V}$ . Also, we know that by modifying the external potential, for instance by reallocating the nuclei, the electronic quantum state changes accordingly. Therefore, if  $\hat{V}$  is bound to a unique density, so is the ground-state electronic wavefunction,  $\Psi_{\text{GS}}(r)$ .

Since the total ground-state energy,  $E_0$ , depends on both  $\hat{V}$  and  $\Psi_{\text{GS}}(r)$ , it must also be uniquely defined by the density. Finally, we write the ground-state energy, the wavefunction, and the external potential as density functionals, denoted  $E[\rho]$ ,  $\psi[\rho]$ , and  $\hat{V}[\rho]$ , respectively. A functional depends only on the form of the function and not on the function's variable, *i.e.*, leaving the operators depending solely on  $\rho(\mathbf{r})$  and not on the space coordinates. DFT reduces largely the number of variables entering the SE, in contrast to the inclusion of all electronic coordinates in space, as in WF-based methods.

---

<sup>2</sup>The variational principle is summarized in Appendix A.1, and the derivation of the Hartree-Fock equations can be found in full detail in Ref. [23], Chapter 3.

### Kohn-Sham Ansatz

The idea presented by Kohn and Sham consists mainly in regarding an auxiliary system of *fictitious* non-interacting fermions with equal ground-state density as the real system [26]. The total ground-state energy functional of the auxiliary system,  $E_s[\rho]$ , is equal to that of the real system,  $E[\rho]$ , given this property is uniquely defined by the electronic density both systems share. The one-electron wavefunctions in the Kohn-Sham scheme (KS) are one-particle spin-orbitals,  $\psi_\nu^{\text{KS}}(\mathbf{x})$ , called *Kohn-Sham orbitals*. They form the Slater determinant,  $\Psi_{\text{SD}}(x)$ , of the total electronic quantum state and the electronic density:

$$\rho(\mathbf{r}) = \sum_{\nu} |\psi_{\nu}^{\text{KS}}(\mathbf{r})|^2. \quad (2.16)$$

From Eq. 2.4 and Eq. 2.7, and disregarding spin, we take the expectation values of the independent particle kinetic energy,  $T_s$ , and the Coulomb interaction:

$$T_s[\rho] \equiv \langle \Psi_{\text{SD}}(r) | \hat{T} | \Psi_{\text{SD}}(r) \rangle = -\frac{1}{2} \sum_{\nu} \int [\psi_{\nu}^{\text{KS}}(\mathbf{r})]^* \nabla^2 \psi_{\nu}^{\text{KS}}(\mathbf{r}) d\mathbf{r} \quad (2.17)$$

$$\langle \Psi_{\text{SD}}(r) | \hat{U} | \Psi_{\text{SD}}(r) \rangle = \frac{1}{2} \int \frac{\rho(\mathbf{r}) \rho(\mathbf{r}')}{|\mathbf{r} - \mathbf{r}'|} d\mathbf{r} d\mathbf{r}' + E_x. \quad (2.18)$$

Besides the defined density functional  $T_s[\rho]$ , there is an interacting component to the total kinetic energy whose expression remains unknown. Likewise, the Coulomb energy has an unknown contribution which corresponds to correlation effects. In order of appearance, the two terms in the right-hand side of Eq. 2.18 are the Hartree energy,  $E_H$ , and the exchange energy  $E_x$ . KS gathers all exchange-correlation interactions beyond the independent particle approach under the *exchange-correlation density functional*,  $E_{xc}[\rho]$ . In addition to the energy contributions from  $T_s$  and  $E_h$ , there is the expectation value of the external potential in Eq. 2.5. Altogether, they return the expression of the energy as a functional of charge density:

$$E[\rho] = \int \rho(\mathbf{r}) v(\mathbf{r}) d\mathbf{r} - \frac{1}{2} \sum_{\nu} \int \psi_{\nu}^*(\mathbf{r}) \nabla^2 \psi_{\nu}(\mathbf{r}) d\mathbf{r} + \frac{1}{2} \int \frac{\rho(\mathbf{r}) \rho(\mathbf{r}')}{|\mathbf{r} - \mathbf{r}'|} d\mathbf{r} d\mathbf{r}' + E_{xc}[\rho]. \quad (2.19)$$

Analogous to the variational method in the HFA (Sec. 2.2.1), we define a functional

$$\mathcal{L}[\{\psi^*\}] = E[\rho] - \sum_{\nu\mu} \epsilon_{\nu\mu} (\langle \psi_{\nu} | \psi_{\mu} \rangle - \delta_{\nu\mu}),$$

where the constraint in the square brackets is the normalization of Kohn-Sham orbitals and  $\epsilon_{\nu\mu}$  is the Lagrange multiplier. We minimize  $\mathcal{L}$  by varying the spin-orbitals  $\psi_{\nu}^*$  and setting the variation on  $\mathcal{L}$  to zero. Following the variational principle, the minimization of the energy functional in Eq. 2.19 returns:

$$\left[ -\frac{\nabla^2}{2} + \hat{v}(\mathbf{r}) + \int \frac{\rho(\mathbf{r}')}{|\mathbf{r} - \mathbf{r}'|} d\mathbf{r}' + \hat{v}_{xc}(\mathbf{r}) \right] \psi_{\nu}(\mathbf{r}) = \sum_{\mu} \epsilon_{\nu\mu} \psi_{\mu}(\mathbf{r}), \quad (2.20)$$

$$\text{with } \hat{v}_{xc}(\mathbf{r}) = \frac{\delta E_{xc}[\rho]}{\delta \rho}. \quad (2.21)$$

Just like in the HFA, this equation does not have the canonical form of the eigenvalue equation. The Kohn-Sham orbitals undergo a unitary transformation, *i.e.*, rotation, and the matrix of Lagrange

multipliers is diagonalized, leading to the Schrödinger-like *Kohn-Sham equations*:

$$\left[ -\frac{1}{2}\nabla^2 + \hat{v}(\mathbf{r}) + \hat{v}_H(\mathbf{r}) + \hat{v}_{xc}(\mathbf{r}) \right] \psi_\nu^{\text{KS}}(\mathbf{r}) = \epsilon_\nu^{\text{KS}} \psi_\nu^{\text{KS}}(\mathbf{r}). \quad (2.22)$$

To start with, KS orbitals from an initial guess return, through Eq. 2.16, some charge density. This result builds the density functionals, and Eq. 2.22 provides a new set of orbitals. This new set  $\{\psi_\nu^{\text{KS}}\}$  is plugged in Eq. 2.16 and the cycle repeats. This procedure, known as *self-consistency cycle*, lasts till a convergence criteria is met, *e.g.*, a certain threshold in charge density variation between consecutive iterations. Although the densities of the auxiliary and real systems are equivalent, and so their total energies, the one-particle energies  $\epsilon_\nu^{\text{KS}}$  are bare mathematical tools and do not correspond to the real single-state eigenvalues. This will prove crucial for the study of excited states.

$E[\rho]$  is, strictly speaking, *partially* unknown. We have a clear hold on the first three summands at the right in Eq. 2.22. The remainder —unknown interactions— is wrapped in the exchange-correlation energy  $E_{xc}[\rho] = -\int e_{xc}(\mathbf{r}, [\rho]) d\mathbf{r}$ , with  $e_{xc}$  the exchange-correlation energy taken per unit volume.

### Local and Semi-Local Exchange-Correlation Potentials

The numerous approximations to  $e_{xc}$  are classified in what is called the *Jacob's ladder*, depending on the variables entering the function [27]. If  $e_{xc}$  depends only on density, the approximation to the exchange-correlation functional is at the bottom of the ladder. In the next step we find those approximations considering the modulus of the density gradient,  $|\nabla\rho|$ , in addition to the density. The third stage includes functionals of those two variables plus another, *e.g.*, the second-order density gradient. Finally, approximations in the fourth rank include the exact exchange introduced in Sec. 2.2.1 and in higher ranks, they include unoccupied KS orbitals. In this project, we look at approximations in the first, second and fourth levels of the Jacob's ladder. Those depending on  $\rho(\mathbf{r})$ , either by itself or together with its variation in space, are so called *implicit* density functionals. On the other hand, the exact exchange is an *explicit* density functional; although it depends on the density, it cannot be written as a functional of such. Section 2.2.3 deals with explicit approximations. This section shortly summarize the two main implicit approximations, along with important theoretical aspects underlying their performance.

### Local-Density Approximation (LDA)

The *local-density approximation* (LDA) proposes an exchange-correlation functional,  $E_{xc}^{\text{LDA}}[\rho]$ , based on the *homogeneous electron gas* (HEG); a system of interacting electrons under a spatially fixed potential. In this model, the electronic charge distribution is constant in space and neutralized by a positive, uniformly distributed charge density. However, systems treated in DFT show, by and large, an inhomogeneous charge distribution. The approximation lies precisely in treating the inhomogeneous density of the system in question as the density of the HEG,  $\rho_0(\mathbf{r})$ , *locally*. In the LDA, the exchange-correlation energy per volume in the HEG, denoted  $e^{\text{HEG}}$ , has a very short range. The exchange potential per volume,  $v_x^{\text{HEG}}(\mathbf{r})$ , is given by

$$v_x^{\text{HEG}}(\mathbf{r}) = \left. \frac{d e_x^{\text{HEG}}(\rho_0)}{d \rho_0} \right|_{\rho_0=\rho(\mathbf{r})} = -\beta \rho^{1/3}(\mathbf{r}), \quad (2.23)$$

and the low-density limit of the correlation part is

$$v_c^{\text{HEG}}(\mathbf{r}) = \left. \frac{d e_c^{\text{HEG}}(\rho_0)}{d \rho_0} \right|_{\rho_0=\rho(\mathbf{r})} \sim e^{-\alpha r/3}. \quad (2.24)$$

The latter decays exponentially in the asymptotic region of finite systems. In Eq. 2.23 and Eq. 2.24,  $\alpha$  and  $\beta$  are constants. Apart from the low- and high-density limits, the exact correlation potential for the HEG is unknown. Thus it poses a higher challenge than its exchange counterpart, which has a well-known form.  $v_c^{\text{HEG}}(\mathbf{r})$  is usually implemented as an analytic function with some fixed parameters.

This rough approximation predicts bond lengths and lattice constants for a large number of materials surprisingly well. However, LDA performs poorly when it comes to atomization energies and predicting the nature of chemical bonds. In those cases, LDA fails by treating the local charge density as homogeneous, which is rarely the case in nature. Improvements to LDA bring us a step higher in the Jacob's ladder.

### Generalized Gradient Approximation (GGA)

To account for changes in the density distribution, the expression of  $E_{xc}$  may include the modulus of the density gradient,  $|\nabla\rho(\mathbf{r})|$ . Defined within an infinitesimal neighborhood centered at  $\mathbf{r}$ , the gradient, and therefore  $E_{xc}$ , are not purely local. Such *semi-local* functionals, called *generalized gradient approximations* (GGA), are of the general form:

$$E_{xc}^{\text{GGA}}[\rho] = \int f(\rho(\mathbf{r}), |\nabla\rho(\mathbf{r})|) d^3r, \quad (2.25)$$

where the function  $f$  may take up several forms, where each type of  $f$  defines a particular GGA. We focus on the most commonly implemented—including the present work—known as PBE after the name of their authors: Perdew-Burke-Ernzerhof [28]. In this GGA functional, the kernel depends on the local Seitz radius,  $r_s$ , and the relative spin polarization,  $\zeta = (\rho_\uparrow + \rho_\downarrow)/\rho$ , with  $\rho_\uparrow$  for spin-up density and  $\rho_\downarrow$  for spin down (removing coordinate variables for simplicity). We shortly give the general form of  $E_{xc}^{\text{PBE}}$ , given  $e_c^{\text{HEG}}$  and  $e_x^{\text{HEG}}$  were already defined in Sec. 2.2.2. The correlation and exchange energy functionals are:

$$E_c^{\text{PBE}}[\rho] = \int \rho [e_c^{\text{HEG}}(r_s, \zeta) + M(r_s, \zeta, t)] d\mathbf{r} \quad ; \quad E_x^{\text{PBE}}[\rho] = \int \rho e_x^{\text{HEG}}(\rho) F_x(s) d\mathbf{r}. \quad (2.26)$$

The gradient of the density enters in a dimensionless function  $s = |\nabla\rho|/2k_F\rho$ , with  $k_F$  being the modulus of the Fermi wavenumber. Embedded in the function  $M$ , there is the dimensionless density gradient  $t$ , analogous to  $s$ . Likewise, the exchange part includes a damping function  $F_x(s)$ . In addition to the system-dependent variables, the functions  $M$  and  $F$  rely upon a set of constants and universal parameters. These are determined so as to comply with a set of conditions for both the correlation and exchange part.

The function  $M$ , owning a simple algebraic expression, guarantees that when the density gradient is in the (i) slowly varying limit,  $M$  is proportional to a second-order gradient expansion, (ii) rapidly varying limit, correlation will vanish, and (iii) uniform scaling to the high-density limit, the correlation energy scales to a constant. These three conditions also apply to the exchange part and, in addition,  $E_x^{\text{PBE}}$  is subject to further constraints. Most importantly, it recovers both the uniform gas limit when  $s = 0$  and the linear response of the electron gas when  $\zeta = 0$ , *i.e.*, spin-unpolarized. In the words of its authors, the goal of PBE is to satisfy those conditions which are energetically significant. The functions  $M$  and  $F_x$  are mainly tools to reach this goal. PBE outperforms LDA at describing chemical bonds, where the density gradient plays a major role, as in many other properties.

### 2.2.3 Generalized Kohn-Sham Scheme

DFT has had an undeniable success predicting ground-state properties of materials such as total energy and lattice constants. However, the electronic structure calculated with DFT has some serious drawbacks. Because this electronic structure is based on the total density, the electron in the system interacts with all electrons, including itself. The *self-interaction* error largely leads to an underestimation of the bandgap of semiconductors.<sup>3</sup> In addition, the bandgap energy,  $E_g$ , in the KS scheme is typically calculated as the energy difference between two one-electron states: the lowest-unoccupied (LU) and highest-occupied (HO) states. Regarding the LU as an excitation energy,  $E_g$  is no longer a ground-state property, hence it falls beyond the framework of the KS theory. To solve the self-interaction error, the KS theory can be expanded to the *generalized Kohn-Sham* (GKS) scheme. In this approach, the density of the GS follows the same principle as in KS, yet it takes into account long-ranged exchange-correlation effects, as well as non-locality, via an extended exchange-correlation potential.

### Hybrid Functionals

The self-interaction error is partly corrected by *hybrid functionals*—belonging to the fourth level in the Jacob’s ladder—which include a certain amount of exact exchange. Carlo Adamo and Vincenzo Barone modified the PBE functional, introducing a hybrid functional, known as PBE0, which has a fixed ratio of 3 : 1 between semi-local  $E_x^{\text{PBE}}$  and non-local exchange  $\Sigma_x$  [29]. Since the self-interaction error varies among different systems, the share of exact exchange is heavily material-dependent and can be tuned to a specific compound. However, we aim at a parameter-free description of the electronic interactions.

---

<sup>3</sup>As mentioned in Sec. 2.2.1, this error is absent in the HFA.

## Chapter 3

# Many-Body Perturbation Theory

In the independent-particle (IP) schemes, electronic interactions are described by a mean-field potential, which simulates the effect of the surrounding electrons (or holes) on a particle. This simplified picture returns one-electron states and their respective eigenvalues, which may fall short to explain the intricacies of the real system as they approximate many-body effects to a mean-field potential. To assess many-body interactions properly, we must take into account the distortion of the potential in the neighborhood of a particle due to its charge. With this goal in sight, a non-interacting system may evolve to an interacting system in a perturbative manner. This is the task of *many-body perturbation theory* (MBPT). The perturbative techniques in MBPT enable the transition from the simplified KS/HFA particles to a more realistic view of correlated electrons and holes.

To describe the electronic structure of a material in view of the many-body problem, we look at the *propagation* of particles in an interacting many-body system. Instead of accounting for all possible interactions for the particles individually, the interaction between one particle and the rest of the system already gives the information we search for, *i.e.*, the energy spectrum. A powerful tool is the one-body propagator function, called Green's function  $G$ , which returns the probability amplitude of propagation of the particle between two distinctive quantum states, as will be described in Sec. 3.2. Employing perturbation techniques, we are able to express  $G$  using the independent Green's function,  $G_0$ , usually a known object, and the Coulomb interaction, as explained in Sec. 3.3. Finally, the *GW approximation* (GWA) in Sec. 3.4 suggests a formula for the *self-energy*; a dynamical operator that includes exchange-correlation effects between a particle and the rest of the system. Every concept in this chapter covers only the spinless *fermionic* case for  $T = 0$  in the thermodynamic limit. With the exception of field operators, we drop the hat on the operators to simplify the notation.

### 3.1 Weakly Interacting Fermions

Following individually all propagating *bodies* is impossible, as hundreds interact directly with each other. On the other hand, consistent with observations in nature, many-body systems often behave as if they consisted of weakly interacting particles. Therefore, an alternative is to consider the quantities describing the behavior of electrons (or holes) as expectation values with respect to the total state, and treat the particles as weakly interacting *quasiparticles* (QPs).

We find many types of QP in nature, *e.g.*, atomic vibrations in the crystal lattice (phonons), but in this work we focus exclusively on quasidelectrons and quasiholes in crystalline solids. These QPs appear as *elementary excitations*; an independent entity in the system which gathers together the particle and the distortion it causes in its surroundings [30, 31]. In principle, the QP concept is only valid in the neighborhood of the Fermi surface, where excitation energies are close to the chemical potential and can be treated as perturbations to the equilibrium state. An idealized metal serves as explanatory example. Here, a positively charged background neutralizes the uniform distribution of the electronic density,  $\rho$ . By introducing a charge  $Q$  in this system, we create a new potential  $\Phi(\mathbf{r})$ , which induces a change in the density. Compared to the unperturbed electronic density distribution,

$\rho$ , the probed charge changes the density distribution by:

$$\Delta\rho = \frac{[2m(\mu - e\Phi(\mathbf{r}))]^{3/2}}{3\pi^2\hbar^3}, \quad (3.1)$$

where  $m$  and  $e$  are the electron mass and charge, respectively, and  $\mu$  is the chemical potential. We assume  $\mu \gg e\Phi$ , and then expand  $\Delta\rho(\mathbf{r})$  in powers of  $\Phi(\mathbf{r})$  to the lowest order. Thereupon, the Poisson equation,  $\nabla^2\Phi(\mathbf{r}) = -4\pi e\Delta\rho$ , reduces to an ordinary differential equation and the potential, under some<sup>1</sup> constraint, takes the form:

$$\nabla^2\Phi(\mathbf{r}) = \frac{1}{\lambda_{\text{TF}}^2}\Phi(\mathbf{r}) \implies \Phi(\mathbf{r}) = \frac{Q}{r} e^{-r/\lambda_{\text{TF}}}, \quad (3.2)$$

with  $\lambda_{\text{TF}}$  being the *Thomas-Fermi length*. By comparing the decay of the induced potential — exponential at a distance of order  $\lambda_{\text{TF}}$  from  $Q$ — to that of the Coulomb potential (in the order of  $1/r$ ), we attest the presence of screening. The charge  $Q$  will be surrounded by a cloud of opposite charged particles, creating the screening. Consequently, if  $Q$  were a hole, electrons attracted to it form a negatively charged cloud. Vice versa, an electron repels neighboring electrons, creating a vacuum around itself which exposes the ionic background; a positively charged cloud spawns around the electron. The charge  $Q$  plus its surrounding cloud make up the QP. In the following, particles without screening cloud are called *bare* particles. Naturally, when the QP propagates, it brings its cloud along, changing its *effective mass*,  $m^*$ , in relation to the bare particle. Two important aspects are: (i) The point particle  $Q$  acquires a finite size when it forms a QP. (ii) The QP conserves the charge and momentum of the bare particle.

Lev Landau first proposed this treatment of interacting particles as QPs, introducing the *Fermi liquid theory* (FLT) based on liquid  ${}^3\text{He}$  (hence the name) as model for a weakly interacting gas [32]. In 1958, Viktor Silin extended the FLT to electrons, serving electronic structure studies [33]. There exists a one-to-one correspondence between the non-interacting particles and the interacting QPs, as long as the non-interacting system evolves *continuously* —without phase transitions— into the interacting system [34]. It is indeed much easier to deal with weakly interacting QP than with bare electrons, yet it is compelling to find a proper method to describe particle interactions.

## 3.2 Propagation function in a one-body quantum theory

The QP concept simplifies the task of describing many-body interactions, but it renders necessary to develop a mathematical tool to work with. In order to familiarize with the main tool, the Green's functions,  $G$ , we look at a general single-particle propagation. The one-body propagator describes the average behavior of one particle, rather than looking at every detailed individual trajectory. The one-particle propagator is the probability amplitude of a particle at position  $\mathbf{r}$  and time  $t$  will be found at position  $\mathbf{r}'$  at time  $t'$ .

In terms of wavefunctions (WFs), the propagation follows the superposition principle: Each point at the wave front acts like a second emitter. Accordingly, we can describe  $\Psi(\mathbf{r}, t)$  in terms of a propagator  $K(\mathbf{r}, t; \mathbf{r}', t')$  acting on another wavefunction,  $\Psi(\mathbf{r}', t')$ , at an earlier point in time:

$$\Psi(\mathbf{r}, t) = \int K(\mathbf{r}, t; \mathbf{r}', t') \Psi(\mathbf{r}', t') d\mathbf{r}', \quad t > t' \quad (3.3)$$

The kernel  $K(\mathbf{r}, t; \mathbf{r}', t')$ , describing the propagation of the wave function, turns zero when the time

---

<sup>1</sup>We regard solely the immediate vicinity of the injected charge, where other electrons are absent, and assume an homogeneous environment around  $Q$ .

$t'$  lies ahead of  $t$ , *i.e.*,  $t < t'$ , known as the *causality principle*. In the time-dependent Schrödinger equation (SE), the WF can be replaced by the expression at the right in Eq. 3.3. This leads to an homogeneous, first-order differential (in time) equation valid for all  $t > t'$ :

$$\left[ i\hbar \frac{\partial}{\partial t} - H(\mathbf{r}) \right] \Psi(\mathbf{r}, t) = 0 \quad \Longrightarrow \quad \left[ i\hbar \frac{\partial}{\partial t} - H(\mathbf{r}) \right] K(\mathbf{r}, t; \mathbf{r}', t') = 0. \quad (3.4)$$

In the following, we use the above to find the Green's function, following Ref. [35]. Often in quantum mechanics, we are faced with two time-dependent differential equations: inhomogeneous,  $[i\hbar\partial_t - H(\mathbf{r})] \Psi(\mathbf{r}, t) = f(\mathbf{r}, t)$ , and homogeneous,  $[i\hbar\partial_t - H(\mathbf{r})] \psi(\mathbf{r}, t) = 0$ , for which we find a function  $G$  that obeys:

$$[i\hbar \frac{\partial}{\partial t} - H(\mathbf{r})] G(\mathbf{r}, t; \mathbf{r}', t') = i\hbar \delta(\mathbf{r} - \mathbf{r}') \delta(t - t'). \quad (3.5)$$

$G$  is the *Green's function*, named after the mathematician George Green who developed the theory in the early 19th century.  $K$  in Equation 3.4 and  $G$  in Eq. 3.5 are connected because the latter can be a combination of different  $K$ s, together with a step function,  $\theta$ .<sup>2</sup>

In the same way as the time-dependent  $G$  in Eq. 3.5, the time-independent SE has a *time-independent*  $G$  assigned to it:  $[z - H(\mathbf{r})] G(\mathbf{r}, \mathbf{r}'; z) = \delta(\mathbf{r} - \mathbf{r}')$ , being  $z$  a complex variable. The Hamiltonian,  $H(\mathbf{r})$ , is a linear, time-independent differential operator, with eigenvalue problem  $H(\mathbf{r}) \Phi_n(\mathbf{r}) = E_n \Phi_n(\mathbf{r})$ , where  $\{\Phi_n\}$  is a complete set of orthonormal eigenfunctions and  $E_n$  their corresponding eigenvalues, each state labeled with  $n$ . Rewriting  $G$  as an expectation value, in Dirac's notation, we obtain the Green's function in operator form:

$$G(\mathbf{r}, \mathbf{r}'; z) = \langle \mathbf{r} | G(z) | \mathbf{r}' \rangle \quad \Rightarrow \quad G(z) = \frac{1}{z - H}. \quad (3.6)$$

Using the completeness property of  $\{\Phi_n\}$ , we rewrite Eq. 3.6 in the so called *Lehmann representation*:

$$G(\mathbf{r}, \mathbf{r}'; z) = \sum_n \frac{\Phi_n(\mathbf{r}) [\Phi_n(\mathbf{r}')]^*}{z - E_n}. \quad (3.7)$$

Since  $H(\mathbf{r})$  is Hermitian,  $E_n$  is real and thus,  $G(\mathbf{r}, \mathbf{r}', z)$  is an analytic function everywhere in the complex plane except for those values of  $z$  which are real and equal to  $E_n$ . In other words, the poles of  $G(\mathbf{r}, \mathbf{r}', z)$  give the discrete eigenvalues of  $H(\mathbf{r})$ . If the spectrum of  $H(\mathbf{r})$  is continuous, the Green's function in the complex plane presents branch cuts rather than poles.

For the time-dependent  $G$ , we regard time differences —given  $H(\mathbf{r})$  is time-independent— and define the variable  $\tau = t - t'$ . Inserting the Fourier transform of the time-dependent  $G$ , expressed as

$$G(\mathbf{r}, \mathbf{r}'; \tau) = \int \frac{d\omega}{2\pi} G(\mathbf{r}, \mathbf{r}'; \omega) e^{-i\omega\tau}, \quad (3.8)$$

into Eq. 3.5 returns  $(\hbar\omega - H)G(\mathbf{r}, \mathbf{r}', \omega) = \delta(\mathbf{r} - \mathbf{r}')$ . This is equivalent to the time-independent case with  $z = \hbar\omega$ , ergo the Lehmann representation also applies for the time-dependent  $G$ , which is the relevant case for us. In the rest of this thesis  $\hbar = 1$ , treating energies and frequencies indiscriminately, and we remove the explicit  $\mathbf{r}$  dependence of operators in the text.

There are infinite solutions to  $G$ , but we are only interested on those under the same boundary conditions governing  $\psi$  and  $\Psi$ . In solid state physics, it is custom to call propagator operators

<sup>2</sup>The step function inserted in the time derivative gives the  $\delta$ -function entering the definition of  $G$ .

“Green’s function”, though strictly speaking not all propagators are solutions to either differential equations above.

### Frequency Integration

To work with the Fourier transform of  $G$  in frequency space, the integral should converge in the interval  $[-\infty, \infty]$ , but it does not. By dividing the time domain in two, we achieve two convergent integrals:

$$G(\mathbf{r}, \mathbf{r}', \omega) = \int_{-\infty}^0 G(\mathbf{r}, \mathbf{r}', \tau) e^{i\omega\tau + \eta\tau} d\tau + \int_0^{\infty} G(\mathbf{r}, \mathbf{r}', \tau) e^{i\omega\tau - \eta\tau} d\tau, \quad (3.9)$$

where  $e^{\eta\tau}$  is a convergent factor, with  $\eta$  infinitesimally positive. We evaluate the complex Fourier transform in the complex plane with frequencies  $\omega \pm i\eta$ . It is convenient to add the step function  $\theta(\tau)$ , allowing to define two Green’s functions: the *retarded* Green’s function,  $G^R(\omega)$ , which is 0 for  $t' > t$  and an *advanced* Green’s function,  $G^A(\omega)$ , which is 0 for  $t' < t$ .  $G^R(\omega)$  obeys the causality principle and the final state is ahead in time with respect to the initial state. On the contrary, by allowing  $t' > t$ , the new state will be in the past with respect to the initial state. At first counterintuitive, this is the case for holes propagating in a system.

### Green’s Functions in Second Quantization

The physical meaning of  $G$  comes to light by looking at its formulation in second quantization. We define the one-body propagators  $G^>$  and  $G^<$ . These are equivalent to  $K$  in Eq. 3.4, but now the initial state can exist at earlier times than the final state, *i.e.*,  $t' > t$ . Since  $G^{\gtrless}$  involve just one body, we take the average for the whole system in the groundstate,  $\Psi_0$ :

$$G^>(\mathbf{r}, t; \mathbf{r}', t') = -i\langle \Psi_0 | \hat{\psi}(\mathbf{r}, t) \hat{\psi}^\dagger(\mathbf{r}', t') | \Psi_0 \rangle \quad , \quad G^<(\mathbf{r}, t; \mathbf{r}', t') = i\langle \Psi_0 | \hat{\psi}^\dagger(\mathbf{r}', t') \hat{\psi}(\mathbf{r}, t) | \Psi_0 \rangle, \quad (3.10)$$

with field operators in the Heisenberg picture (Eq. B.16).  $G^>$  describes the creation of an electron at  $\mathbf{r}'$  in the groundstate at time  $t'$ , followed by its annihilation at  $\mathbf{r}$  at time  $t$ , whilst  $G^<$  describes the same events in the reverse order. Note that the annihilation of an electron equals the creation of a hole. The probability amplitude of a particle being at a final state starting from a particular initial state is given by both expressions in Eq. 3.10, namely the overlap of both states. Alternatively, we can define these functions as *dynamic* correlation functions which link two fermionic states at different times. The correlated quantities—in the statistical sense—are the field operators.<sup>3</sup>

Since  $G^{\gtrless}$  are solutions to Eq. 3.4, their combinations build the Green’s functions in Eq. 3.5. Based on this principle, we build the retarded and advanced Green’s functions:

$$G^R(\mathbf{r}, t; \mathbf{r}', t') = \theta(t - t') [G^>(\mathbf{r}, t; \mathbf{r}', t') - G^<(\mathbf{r}, t; \mathbf{r}', t')] \quad (3.11)$$

$$G^A(\mathbf{r}, t; \mathbf{r}', t') = \theta(t' - t) [G^<(\mathbf{r}, t; \mathbf{r}', t') - G^>(\mathbf{r}, t; \mathbf{r}', t')]. \quad (3.12)$$

$G^R$  describes the propagation of an electron which can take place by either process described with  $G^{\gtrless}$ .  $G^A$  is analogous to the previous, but for negative times, treating hole propagation. In the rest of this thesis,  $G^{\gtrless}$  do not appear by themselves, since we are interested in solutions to Eq. 3.5, rather we look at retarded or advanced Green’s functions,  $G^{R/A}$ . Both  $G^R$  and  $G^A$  are encapsulated in the time-ordered  $G^T$ , referred to as simply  $G$  from now on.

$$G^T = G(\mathbf{r}, t; \mathbf{r}', t') = -i\langle \Psi_0 | T [\hat{\psi}(\mathbf{r}, t) \hat{\psi}^\dagger(\mathbf{r}', t')] | \Psi_0 \rangle. \quad (3.13)$$

<sup>3</sup>Two quantities are correlated if the product of the expectation value for each quantity differs from the expectation value of the product of both quantities.

The time-order operator  $T$  acts on the field operators, such that the most recent in time stands at the right. In conclusion, the time-dependent SE may have a homogeneous or an inhomogeneous solution,  $\psi$  and  $\Psi$ , respectively, both of which can be described by the same  $G$  obeying Eq. 3.5.

### Unperturbed Green's Function: $G_0$

The time-independent Hamiltonian of an independent particle system, in general  $H_0$ , is a Hermitian, space-symmetric one-body operator. The corresponding eigenstates  $\psi_n^0(\mathbf{r}, t)$  are solutions to  $[i\hbar\partial_t - H_0(\mathbf{r})]\psi_n^0(\mathbf{r}, t) = 0$ . For that SE, the Green's function obeying Eq. 3.5 is the unperturbed one-body Green's function,  $G_0$ . The Lehmann representation for  $G_0$ , with  $z = \omega \pm i\eta$  and single particle eigenvalues  $\epsilon_n^0$ , is diagonal in the basis of  $\psi_n^0$ :

$$G_0(\mathbf{r}, \mathbf{r}'; \omega) = \lim_{\eta \rightarrow 0^+} \sum_n \frac{\psi_n^0(\mathbf{r}, t) [\psi_n^0(\mathbf{r}', t')]^*}{\omega - \epsilon_n^0 + i\eta \operatorname{sgn}(\epsilon_n^0 - \mu)} \quad (3.14)$$

The propagating electron has energy  $\epsilon_n^0 > \mu$ , whereas the hole has energy  $\epsilon_n^0 < \mu$ , and we take the  $\operatorname{sgn}$  function to distinguish both cases.

## 3.3 Connecting Non-Interacting and Interacting Systems

As any  $G_0$  is specific to an independent particle Hamiltonian  $H_0$ , so is  $G$  specific to a Hamiltonian  $H$  describing the whole system. In operator form,  $G$  and  $G_0$  are:

$$G(\omega) = \frac{1}{\omega - H} \quad , \quad G_0(\omega) = \frac{1}{\omega - H_0}. \quad (3.15)$$

The full Hamiltonian can be divided in the non-interacting and an interacting contribution:  $H = H_0 + H_1$ , where  $H_1$  may depend on time. This sum replaces  $H$  in Eq. 3.15, to form the *Dyson equation*:

$$G(\omega) = (\omega - H_0 - H_1)^{-1} = [1 - (\omega - H_0)^{-1}H_1]^{-1} (\omega - H_0)^{-1} = [1 - G_0(\omega)H_1]^{-1} G_0(\omega) \quad (3.16)$$

$$G(\omega) = G_0(\omega) + G_0(\omega)H_1G(\omega), \quad (3.17)$$

Inserting the geometric series,

$$[1 - G_0(\omega)H_1]^{-1} = 1 + G_0(\omega)H_1 + G_0(\omega)H_1G_0(\omega)H_1G_0(\omega) + \dots$$

into the first equation, recasts  $G$  as a sum over terms containing  $G_0H_1$ , called a *Born series*, where these terms describe single, double, etc..., scattering processes, with  $H_1$  being the scattering potential.

The  $G$  above holds the information of everything regarding the single QP in the system. It is instructive to ask what information we are looking for.  $H$  is a complicated unknown object and it encloses the interactions of the whole system. While  $H_0$  is a one-body operator, the same cannot be assumed of  $H_1$ . A deep discussion on the matter is out of the scope of this thesis, but is to be found in detail in Chapter 7 of Ref. [36]. We merely give the basic conclusions: (i) We are only interested in a subsystem of the whole system; the quasiparticles. (ii) QPs are connected to the whole system through a dynamical mean-field that will replace  $H_1$  in Eq. 3.17. (iii) The  $G$  of this subsystem returns solutions to the SE describing QPs, that is to say the set of eigenvectors and eigenvalues,

$\{\psi_n^{\text{QP}}, \epsilon_n^{\text{QP}}\}$ . (iv) From the definition in Eq. 3.13,  $G(\mathbf{r}, t; \mathbf{r}, t^+)$  yields the electronic density  $\rho(\mathbf{r})$ :

$$-iG(\mathbf{r}, t; \mathbf{r}, t^+) = \rho(\mathbf{r}). \quad (3.18)$$

As an example of the above discussion, in the KS picture the object of interest: independent particles in a mean-field. The Green's function for the KS scheme, according to Eq. 3.17, is  $G^{\text{KS}} = G_0 + G_0(v_H(\mathbf{r}) + v_{xc}(\mathbf{r}))G^{\text{KS}}$ . Here the interacting part of the Hamiltonian, *i.e.*,  $H_1$ , is a one-body static potential, and the solutions are the optimized one-electron Kohn-Sham orbitals  $\{\psi_n^{\text{KS}}(\mathbf{r})\}$ . The Kohn-Sham particles are bound to the rest of the system through this  $H_1$ .

We aim at describing QPs, described by  $G$ , starting from a bare particle, for which  $G_0$  is known. To describe the changes in time caused by the propagation of a QP, the interaction potential  $H_1$  needs to include a dynamical screening. We go about this task by treating the interaction as a perturbation in the system, not a trivial assignment since its contribution to the energy is comparable to that of  $H_0$ .

### 3.3.1 Diagrammatic expansion of $G$

As pointed out in Sec. 3.1, the transition from the non-interacting system to the interacting one has to preserve the original total momentum and the individual propagation of the particles. As a gedankenexperiment, we can picture the Coulomb interaction to be *turned on* adiabatically—slow enough as to remain in equilibrium—among non-interacting particles in the groundstate  $|\Psi_0\rangle$ . When the interaction is fully present, the particles become dressed with their screening cloud and we reach the interacting groundstate,  $|\Psi\rangle$ .<sup>4</sup>

The Heisenberg picture assigns the time evolution to operators, such as the interaction potential,  $V(t)$ , and the field operators, while states are static. This picture relates to the interacting and Schrödinger pictures in that, regardless of the chosen framework, the matrix elements are the same. Since  $G$  in Eq. 3.13 is taken as an expectation value, its formulation in the Heisenberg picture and the interaction picture have equal results. We write these expectation values with respect to the *intermediate* states,  $|\Psi^{\pm\eta}\rangle$ , in the adiabatic turning-on of the interaction, with subscript  $H$  and  $I$  for the Heisenberg and interaction picture, respectively :

$$\langle \Psi_H^{+\eta} | \text{T} \left[ \hat{\psi}(\mathbf{r}, t) \hat{\psi}^\dagger(\mathbf{r}', t') \right] | \Psi_H^{-\eta} \rangle = \langle \Psi_I^{+\eta} | \text{T} \left[ \hat{\psi}_I(\mathbf{r}, t) \hat{\psi}_I^\dagger(\mathbf{r}', t') \right] | \Psi_I^{-\eta} \rangle \quad (3.19)$$

$$= \langle \Psi_0 | U_I^\eta(\infty, t) \text{T} \left[ \hat{\psi}_I(\mathbf{r}, t) \hat{\psi}_I^\dagger(\mathbf{r}', t') \right] U_I^\eta(t, -\infty) | \Psi_0 \rangle \quad (3.20)$$

At times  $t_0 = \pm\infty$ , there is no interaction and the system is in state  $|\Psi_0\rangle$  and at time  $t$  it reaches the intermediate interacting state  $|\Psi^{-\eta}\rangle$  when evolving from the past, and  $|\Psi^{+\eta}\rangle$  coming from the future. Equation 3.20 respects the time ordering by placing the state in the future to the left. As we turn on the interaction, the evolution operator in the interaction picture,  $U_I$ , acts on the state  $|\Psi_0\rangle$ , returning  $|\Psi^{\pm\eta}\rangle$ . Because  $U_I$  depends on the interaction potential, it also changes adiabatically, and we add a superscript  $\eta$ . At the end, we take the limit  $\eta \rightarrow 0$  to recover the interacting groundstate  $|\Psi\rangle$ , and the interaction becomes the full Coulomb interaction. Time-wise, this corresponds to time  $t = 0$ , *i.e.*, the present, and the  $G$  of the interacting groundstate is:

$$G(1, 2) = -i \langle \Psi | \text{T} \left[ \hat{\psi}(1) \hat{\psi}^\dagger(2) \right] | \Psi \rangle = -i \frac{\langle \Psi_0 | \text{T} \left[ \hat{\psi}_I(1) \hat{\psi}_I^\dagger(2) S \right] | \Psi_0 \rangle}{\langle \Psi_0 | S | \Psi_0 \rangle}, \quad (3.21)$$

where the space coordinates  $\mathbf{r}_1$  at time  $t_1$  of particle one are gathered under variable 1, and  $t_1^+ = \lim_{\eta \rightarrow 0^+} t_1 + \eta$ , with  $\eta$  infinitesimal positive. Here, the product of evolution operators

<sup>4</sup>Such a connection of these groundstates is known as the *Gell-Mann-Low Theorem*.

$U_I(-\infty, t)U_I(t, +\infty) = U_I(-\infty, +\infty)$  defines the operator  $S$ . The denominator in Eq. 3.21 fulfills the normalization criteria and avoids divergent phase factors. We expand  $U_I$  according to Eq. B.24, with interaction potential

$$V_I(t) = \frac{1}{2} \int \int \hat{\psi}_I^\dagger(\mathbf{r}, t) \hat{\psi}_I^\dagger(\mathbf{r}', t) v(\mathbf{r}, \mathbf{r}') \hat{\psi}_I(\mathbf{r}', t) \hat{\psi}_I(\mathbf{r}, t) d\mathbf{r} d\mathbf{r}', \quad (3.22)$$

where  $v(1, 1') = \delta(t_1 - t'_1)v(\mathbf{r}_1 - \mathbf{r}'_1)$  is the Coulomb interaction. After the expansion, the numerator in Eq. 3.21 becomes:

$$G_0(\mathbf{r}, t; \mathbf{r}', t') + \sum_{n=1}^{\infty} \left(\frac{1}{2}\right)^n \frac{1}{n!} \int \int d1 d1' \dots \int \int dn dn' v(1, 1') \dots v(n, n') \\ \times G_{2n+1}^0(\mathbf{r}, t, 1, 1', \dots, n, n'; \mathbf{r}', t', 1, 1', \dots, n, n') \quad (3.23)$$

Disregarding the sum in Eq. 3.23, the lowest order approximation to  $G$  is simply  $G_0$ . The next term is the sum of non-interacting, *many-body* Green's functions  $G_{2n+1}^0$ , which describe the propagation of two, three, and more particles. Using *Wick's theorem* (explained extensively in Ref. [37]), higher-order non-interacting Green's functions can be expressed in terms of products of one-body  $G_0$ :

$$G_{2n+1}^0((\mathbf{r}, t), 1, 1', \dots, n, n'; (\mathbf{r}', t'), 1, 1', \dots, n, n') = \sum_{\mathcal{P}} (-1)^{\mathcal{P}} \\ \times G_0((\mathbf{r}, t), (\tilde{\mathbf{r}}, \tilde{t}')) \dots G_0(n, \tilde{n}) G_0(n', \tilde{n}'), \quad (3.24)$$

with  $\mathcal{P}$  the permutation of two indexes,  $\mathcal{P}$  the number of permutations, and  $\tilde{n}$  the permuted indexes. Inserting this definition of  $G_{2n+1}^0$  in Eq. 3.23, the interacting  $G$ , taken as expectation value of independent particle states, depends on an infinite sum over products of one-body  $G_0$  and the Coulomb interaction. This definition shows that the propagations of different (independent) particles are concatenated by the bare Coulomb interaction.

## The Self-Energy

Using Wick's theorem, Eq. 3.23 becomes an infinite sum of Feynman diagrams. Certain diagrams can be split into two simpler diagrams by cutting one line; these lower-order diagrams can be joined by a non-interacting propagator. The lower-order diagrams which are topologically distinct, are called *irreducible* diagrams. The sum of the irreducible diagrams is the *self-energy*,  $\Sigma$ . We define  $\Sigma$  as *the energy of the QP due to the perturbation in the system caused by its own presence*. In other words, it is the kernel which couples the bare quantity  $G_0$  to the dressed solution  $G$ , described in the Dyson equation:<sup>5</sup>

$$G(\omega) = G_0(\omega) + G_0(\omega)\Sigma(\omega)G(\omega). \quad (3.25)$$

Recalling the opening of this section,  $\Sigma$  couples the QPs to the rest of the many-body system. Analogously, we regard a bare quantity, the Coulomb interaction  $v$ , and a dressed dynamical quantity, the *screened Coulomb interaction*  $W$ .

$$W(\omega) = v + vP(\omega)W(\omega) \quad (3.26)$$

<sup>5</sup>The rigorous definition is *proper or irreducible* self-energy. Since we are not working with the reducible type, the discrimination between both does not apply here.



Figure 3.1: The diagram at the right represents the right-hand side of the Dyson equation for  $G$  (black propagation line).  $G_0$  is the grey propagation line and  $\Sigma$  is the dark circle. Analogous, the diagram at the left corresponds to the rhs of the Dyson equation for  $W$  (wiggly line).  $v$  is the dashed line and  $P$  is represented by the dark ellipse.

Weaker than the bare Coloumb interaction  $v$ , the screened Coulomb interaction arises from the screening cloud of the QP. As shown in Fig. 3.1, the coupling kernel between both quantities is the *irreducible* polarizability,  $P$ , defined as the change in charge density due to changes in the total potential.

### 3.3.2 Equation of motion for $G$

To find the explicit function of  $\Sigma$ , we look at the equation of motion of  $G$  in the Heisenberg picture. The derivation on time returns a higher-order Green's function:<sup>6</sup>

$$\left[ i \frac{\partial}{\partial t_1} - H_0(\mathbf{r}_1) \right] G(1, 1') + i \int v(\mathbf{r}_1, \mathbf{r}_2) G_2(1, 2, 1', 2^+) d\mathbf{r}_2 \Big|_{t_2=t_1^+} = \delta(1, 1'). \quad (3.27)$$

$H_0$  includes the kinetic energy potential and the crystal potential, and  $G_2$  is the two-body Green's function. Equation 3.27 is a differential equation which does not comply with the Green's function definition in Eq. 3.5. However, it is still called a Green's function. We can plug in the non-interacting Green's function in the equation of motion, as shown below:

$$\begin{aligned} \left[ i \frac{\partial}{\partial t_1} - H_0(\mathbf{r}_1) \right] G_0(1, 1') = \delta(1, 1') &\implies G_0^{-1} = i \frac{\partial}{\partial t} - H_0 \\ G(1, 1') = G_0(1, 1') - i \int G_0(1, 2) v(2, 3) G_2(2, 3^+, 1', 3^{++}) d2 d3 \end{aligned} \quad (3.28)$$

By inserting  $G_2$  in the equation of motion, a third-order Green's function arises. Any order Green's function depends on a higher-order Green's function, establishing a hierarchy of infinite order. Since we aspire at a solvable form of  $G$ , we need to approximate this family of Green's functions.  $G_2$  represents the contributions to the energy of the QP beyond the non-interacting particle:

$$\begin{aligned} G_2(2, 3^+, 1', 3^{++}) = G(2, 1') G(3^+, 3^{++}) - G(2, 3^{++}) G(3^+, 1') \\ + \int \Gamma(\tilde{2}, \tilde{3}^+, \tilde{1}', 3^{\tilde{++}}) G(2, \tilde{2}), G(3^+, \tilde{3}^+) G(1', \tilde{1}') G(3^{++}, 3^{\tilde{++}}). \end{aligned} \quad (3.29)$$

Taking this definition, the product of  $G_2$  with  $v$  in Eq. 3.28 reveals two known contributions to the self-energy, the Hartree and exact-exchange operators:

$$-i \int v(2^+, 3) G(3, 3^+) d3 = v_H(2) \quad (3.30)$$

$$i \int v(2^+, 3) G(2, 3) d2 d3 = \Sigma_x(2, 3), \quad (3.31)$$

where in the first line we used Eq. 3.18. The third term in Eq. 3.29 carries the interaction among two-body propagations, the vertex function,  $\Gamma$ . Neglecting this interaction,  $G$  agrees with the HFA. However, the part of the self-energy beyond HFA includes important many-body effects described

<sup>6</sup>The derivation of the equation of motion for  $G$  can be found in Refs. [31] and [38].

by  $\Gamma$ . Fortunately, we can brake the complexity of  $\Gamma$  down into several approximations, providing workable solutions for  $G$  and  $\Sigma_c$ .

### 3.4 Hedin's Equations

In 1965, Lars Hedin introduced an approximation to the self-energy based on functionals of  $G$  [5]. It led to a set of equations which calculates the one-body Green's function self-consistently. To do so, Hedin wrote all the quantities involved as an expansion in  $W$ .

Comparing the equation of motion of the one-particle Green's function to the Dyson equation, we collect the unknowns in the self-energy. The interacting one-body Green's function follows the equation:

$$G(1, 1') = G_0(1, 1') + i \int G_0(1, 2) \Sigma(2, 3) G(3, 1') d2 d3. \quad (3.32)$$

The  $\Sigma$  in Eq. 3.32 includes  $v_H$  and  $\Sigma_x$ , plus the contribution from  $\Gamma$ . Hedin did not address this last term directly, whose definition is cumbersome; it involves the sum of all disconnected diagrams. Rather, his paper works with a three-point vertex,  $\tilde{\Gamma}$ , derived through functional derivative methods (explained in Appendix A of Ref. [5]):

$$\tilde{\Gamma}(1, 2; 3) = - \left. \frac{\delta G^{-1}(1, 2)}{\delta U_{eff}(3)} \right|_{U=0} = \delta(12)\delta(13) + \frac{\delta \Sigma(12)}{\delta U_{eff}(3)} \quad (3.33)$$

$$\left. \frac{\delta G(1, 2)}{\delta U(3)} \right|_{U=0} = G(12) G(33^+) - G(1323^+). \quad (3.34)$$

The effective potential,  $U_{eff}$ , is the sum of a test potential  $U$  —set to zero at the end— and the Hartree potential. From Eq. 3.34, we replace  $G_2$  in Eq. 3.28 and end up with  $v(2, 3)[G(12) G(33^+) - \delta_U G(1, 2)]$ . The first term includes the Hartree potential, and the other includes the exchange-correlation self-energy,  $\Sigma_{xc}$ . The derivative of  $G$  in Eq. 3.34 relates to the derivative of  $G^{-1}$  (Eq. A15 in Ref. [5]), so we may also define  $\Sigma_{xc}$  in terms of  $\tilde{\Gamma}$ .

#### Expansion of the Self-Energy

Hedin used the known formula of  $W$  to incorporate the partial derivative of  $G^{-1}$ , summarized here:<sup>7</sup>

$$W(1, 2) = v(1, 2) + i \int v(1, 3) v(2, 4) G(4, 5) \frac{\partial G^{-1}(5, 6)}{\partial U(3)} G(6, 4^+) d3 d4 d5 d6 \quad (3.35)$$

$$= v(1, 2) + \int W(1, 3) P(3, 4) v(2, 4) d3 d4 \quad (3.36)$$

$$\text{using } \frac{\partial}{\partial U(1)} = \int \frac{\partial U_{eff}(2)}{\partial U(1)} \frac{\partial}{\partial U_{eff}(2)} \quad (3.37)$$

$$P(3, 4) = i \int G(4, 5) G(6, 4^+) \frac{\partial G^{-1}(5, 6)}{\partial U_{eff}(3)} d5 d6. \quad (3.38)$$

Equation 3.36 is reminiscent of the Dyson equation for  $W$ . In general, we arrive at  $P$ , defined as  $\partial \rho(1) / \partial U_{eff}(2)$ , by replacing  $\rho$  with  $G$ , and using functional derivative. The functional derivative

<sup>7</sup>The formulation of  $W$  in terms of the density correlation function —which in turn can be defined in terms of  $G$ — was introduced by John Hubbard [39].

in Eq. 3.38 is the  $\tilde{\Gamma}$ , as defined in Eq. 3.33. We can now write  $\Sigma_{xc}$  as

$$\Sigma_{xc}(1, 2) = i \int W(1^+, 3) G(1, 4) \tilde{\Gamma}(4, 2; 3) d3 d4, \quad (3.39)$$

The original product  $v(2, 3)\delta_U G(1, 2)$ , the starting point of this derivation, is equivalent to Eq. 3.39. It is of interest to express  $W$ ,  $P$ , and  $\Sigma_{xc}$  as functionals of  $G$ , relating them to each other. The three-points vertex can be expanded in its derivative of  $\Sigma_{xc}$ . Taking the first two terms of this expansion, the self-energy reads:

$$\Sigma(1, 2) = i G(1, 2) W(1^+, 2) - \int G(1, 3) G(3, 4) G(4, 2) W(1, 4) W(3, 2) d3 d4 + \dots \quad (3.40)$$

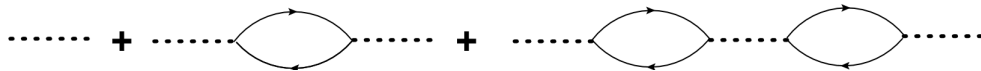
Finally,  $\Sigma_{xc}$ ,  $W$ , and  $P$  are functionals of  $G$  and depend on the bare Coulomb interaction, which has a known expression. Using the Lehman representation,  $G$  can be obtained self-consistently from the QP eigenfunctions,  $\psi^{\text{QP}}$ , or by solving the Dyson equation. In turn,  $\psi^{\text{QP}}$  can be derived from the quasiparticle equation in the frequency, or equivalently, the energy domain:

$$H_0(\mathbf{r}) \psi_{n\mathbf{k}}^{\text{QP}}(\mathbf{r}) + \int \Sigma(\mathbf{r}, \mathbf{r}'; \epsilon_{n\mathbf{k}}^{\text{QP}}) \psi_{n\mathbf{k}}^{\text{QP}}(\mathbf{r}') d\mathbf{r}' = \epsilon_{n\mathbf{k}}^{\text{QP}} \psi_{n\mathbf{k}}^{\text{QP}}(\mathbf{r}). \quad (3.41)$$

This time  $H_0$  includes the Hartree potential, besides the kinetic and crystal lattice potential. This equation was derived by Julian Schwinger in 1951 and then studied for electrons by G. Pratt Jr. [40]. A clear-cut derivation is to be found on pages 353 - 354 of Ref. [41].

### Random Phase Approximation (RPA)

After introducing GWA, the question which prevails is the number of ingoing terms in Eq. 3.40 in order to yield an adequate approximation of the self-energy. The first order approximation to  $\tilde{\Gamma}$  is its diagonal form, *i.e.*, it equals one. This approximation is called the random phase approximation (RPA). Within the RPA, the polarizability is  $P^{\text{RPA}} \equiv GG$ , arriving at a the inverse dielectric function  $\epsilon^{-1} = (1 - P^{\text{RPA}}v)^{-1}$ , which is the Lindhard equation. In diagrammatic form, the first three terms in the expansion of  $W^{\text{RPA}}$  in its Born series,  $W^{\text{RPA}} = v + vP^{\text{RPA}}W = v + vP^{\text{RPA}}v + vP^{\text{RPA}}vP^{\text{RPA}}v + \dots$ , are:



Every term inserts a new electron-hole pair, connected by the bare interaction. Therefore, it is also called the *bubble approximation*. It was first introduced by David Bohm and David Pines in a collection of papers in the early fifties [42–45].<sup>8</sup> The authors explained that the response from electrons to the Coulomb interaction among them consists in a long-ranged collective component and an individual short-ranged screened interaction. The RPA amounts to treating the long-range contributions as an external perturbation.

### GW Approximation (GWA)

Hedin suggested to take  $\tilde{\Gamma}$  as in the RPA; that is neglecting higher order contributions to its expansion. By assuming  $\tilde{\Gamma}(1, 2; 3) = \delta(1, 2)\delta(1, 3)$ , the self-energy reduces to the product of  $G$  and  $W$ . Pointing to this product, this approximation is known as the *GW Approximation* or GWA. In frequency space,

<sup>8</sup>In its early stages, the RPA used planewaves and the authors focused on the exemption of random phases in the sum of exponential terms for response functions, hence the name.

the Fourier transform of Hedin's equations reduces to:

$$P_0(\mathbf{r}, \mathbf{r}'; \omega) = -\frac{i}{2\pi} \int G_0(\mathbf{r}, \mathbf{r}'; \omega + \omega') G_0(\mathbf{r}', \mathbf{r}; \omega') e^{i\omega'\eta} d\omega' \quad (3.42)$$

$$\epsilon(\mathbf{r}, \mathbf{r}'; \omega) = \delta(\mathbf{r}, \mathbf{r}') - \int v(\mathbf{r}, \mathbf{r}_1) P_0(\mathbf{r}_1, \mathbf{r}'; \omega) d\mathbf{r}_1 \quad (3.43)$$

$$W(\mathbf{r}, \mathbf{r}'; \omega) = v(\mathbf{r}, \mathbf{r}') + \int \int v(\mathbf{r}, \mathbf{r}_1) P_0(\mathbf{r}_1, \mathbf{r}_2; \omega) W(\mathbf{r}_2, \mathbf{r}'; \omega) d\mathbf{r}_1 d\mathbf{r}_2 \quad (3.44)$$

$$= \int \epsilon^{-1}(\mathbf{r}, \mathbf{r}_1; \omega) v(\mathbf{r}_1, \mathbf{r}') d\mathbf{r}_1 \quad (3.45)$$

$$\Sigma(\mathbf{r}, \mathbf{r}'; \omega) = \frac{i}{2\pi} \int G_0(\mathbf{r}, \mathbf{r}'; \omega + \omega') W(\mathbf{r}', \mathbf{r}; \omega) e^{i\omega'\eta} d\omega' \quad (3.46)$$

As a common practice, we approximate  $G$  in Eq. 3.42 to lower order, *i.e.*,  $G \approx G_0$ , and write  $P^{\text{RPA}}$  as  $P_0$ .

### 3.4.1 One-shot GWA

Hedin's equations within the RPA approach should, in principle, be solved iteratively. However, it has proven sufficient to correct independent-particle eigenvalues to first-order using the self-energy calculated as in Eq. 3.46 [7]. We build the  $G_0$  from the eigenvectors calculated with some independent-particle scheme, for example the Kohn-Sham method. Doing so, the quasiparticle eigenvalue for a state with band index  $n$  and wave-vector  $\mathbf{k}$  is:

$$\epsilon_{n\mathbf{k}}^{\text{QP}} = \epsilon_{n\mathbf{k}}^{\text{KS}} + \langle \psi_{n\mathbf{k}}^{\text{KS}}(\mathbf{r}) | \text{Re}[\Sigma(\mathbf{r}, \mathbf{r}'; \epsilon_{n\mathbf{k}}^{\text{QP}}) - v_{xc}(\mathbf{r})\delta(\mathbf{r} - \mathbf{r}') | \psi_{n\mathbf{k}}^{\text{KS}}(\mathbf{r}') \rangle, \quad (3.47)$$

where  $v_{xc}(\mathbf{r})$  is the exchange-correlation potential in the independent-particle scheme. The energy-dependence of  $\Sigma$  makes Eq. 3.47 non-linear, but we can expand the self-energy around  $\omega = \epsilon_{n\mathbf{k}}^{\text{KS}}$ :

$$\Sigma(\mathbf{r}, \mathbf{r}'; \epsilon_{n\mathbf{k}}^{\text{QP}}) \approx \Sigma(\mathbf{r}, \mathbf{r}'; \epsilon_{n\mathbf{k}}^{\text{KS}}) + (\epsilon_{n\mathbf{k}}^{\text{QP}} - \epsilon_{n\mathbf{k}}^{\text{KS}}) \frac{\partial \Sigma(\mathbf{r}, \mathbf{r}'; \epsilon_{n\mathbf{k}}^{\text{KS}})}{\partial \omega}. \quad (3.48)$$

We define the renormalization factor, leading to the new quasiparticle energy,  $\epsilon^{\text{QP}}$ :

$$Z_{n\mathbf{k}} = \left[ 1 - \left( \frac{\partial \Sigma(\mathbf{r}, \mathbf{r}'; \epsilon_{n\mathbf{k}}^{\text{KS}})}{\partial \omega} \right) \right]^{-1} \quad (3.49)$$

$$(3.50)$$

$$\epsilon_{n\mathbf{k}}^{\text{QP}} = \epsilon_{n\mathbf{k}}^{\text{KS}} + Z_{n\mathbf{k}} \langle \psi_{n\mathbf{k}}^{\text{KS}}(\mathbf{r}) | \text{Re}[\Sigma(\mathbf{r}, \mathbf{r}'; \epsilon_{n\mathbf{k}}^{\text{KS}}) - v_{xc}(\mathbf{r})\delta(\mathbf{r} - \mathbf{r}') | \psi_{n\mathbf{k}}^{\text{KS}}(\mathbf{r}') \rangle \quad (3.51)$$

This successful method, called one-shot GW or  $G_0W_0$ , improves the independent-particle eigenvalues, approaching experimental results. To justify for the perturbative correction of eigenvalues, Hybertsen and Louie argued that the wavefunctions of the quasiparticle and that of IP schemes have sufficient overlap and can be assumed equal [7].



## Chapter 4

# Quasiparticle Self-Consistent GW

In this chapter, we examine the main subject of this dissertation: the Quasiparticle Self-Consistent GW, QSGW for short. The first section introduces the theoretical framework, succeeded by a section showing the mathematical background to the QSGW. To harmonize the terminology, in the last section we discuss how to categorize this *ab initio* approach.

Before wading in the theory of QSGW, we draw some connections to previous sections in this thesis. The inclusion of the electron-electron interaction,  $v(\mathbf{r}, \mathbf{r}')$  differs greatly among the theories and approximations. For instance, in the independent particle approaches, the direct electronic interaction is replaced by a mean-field.

However, based on the opening argument in Chapter 3, many-body perturbation theory (MBPT) offers a better description of interactions in the system. Theoretically, the *dynamical* exchange-correlation potential in MBPT,  $\Sigma_{xc}(\omega)$ , comes from a universal functional  $\Phi$ ,

$$\Sigma_{xc}(\omega) = 2\pi i \frac{\delta\Phi_{xc}[G]}{\delta G(\omega)}, \quad (4.1)$$

called the Luttinger-Ward (LW) functional, which is the sum of an *infinite* number of “skeleton” diagrams [34]. Here and in the following, we suppress spatial arguments of the quantities involved (with a few exceptions) and regard them as matrices. This infinite sum in the LW theorem can be truncated, thus realizing solvable solutions for the self-energy. One of this solution is the GW Approximation, which works with a sub-set of diagrams in the LW theorem.

Because IP or MBPT methods manage the electrostatic interaction to different degrees of approximations, the picture of the fermion in question changes. A very successful description of interacting fermions are quasiparticles, introduced in Sec. 3.1. When the particle is not surrounded by a screening cloud, we call it *bare* QP and when it does, it is the *dressed* QP. In this regard, the Kohn-Sham particles are bare QPs, and QPs described by Hedin’s equations are dressed QPs. Because the description of the QP falls back to the Hamiltonian, we know that the connotation “bare” or “dressed” reflects the treatment of the Coulomb interaction. Most importantly, the “bare” QP has to have a one-to-one correspondence to the “dressed” QP to follow the Fermi liquid theory, which we exploit in the following.

We aim at evolving the bare QP —with properties given by a known  $G_0$ — into the dressed QP. An alternative is the corrective perturbation in  $G_0W_0$ , but this does not return eigenvectors of the dressed QP and it depends on the underlying IP scheme [11, 46, 47]. In addition,  $G_0W_0$  is not conserving, unlike the GWA. This last aspect is indeed crucial; conservation laws are a reliable measuring stick to judge the adequacy of an approximation. To cure the problems of  $G_0W_0$ , we resort to self-consistency.

### 4.1 Self-Consistent GW

The GWA is in principle self-consistent. Through the Dyson’s equation, we may update the  $G$  —within the random phase approximation (RPA)— using an initial guess for the self-energy, so as to repeat the cycle of Hedin’s equations till convergence, a scheme called *fully self-consistent GW*

(scGW). The  $G$  in scGW is indeed conserving, but unfortunately the screened interaction,  $W(\omega)$ , is not. In the scGW, the RPA polarizability does not fulfill the definition  $\partial\rho/\partial U$  when calculated with the  $G$  from scGW. Likewise, the imaginary part of the diagonal  $\epsilon^{-1}$  also does not fulfill the  $f$ -sum rule, directly linked to particle conservation number [48, 49].<sup>1</sup>

Kotani, Schilfgaarde, and Faleev suggested an alternative self-consistent GW method: the QSGW. Their proposal is best understood through the adiabatic connection of a bare QP, described by a known  $H_0$ , to a dressed QP. The difference between both types of QPs is the interaction potential, yet their one-to-one correspondence allows the non-interacting system to evolve into the interacting one. Prior to the turning-on of the interaction, the bare QPs interact through an effective potential,  $v_{eff}$ , which holds the lattice and Hartree potentials plus an exchange-correlation potential,  $v_{xc}$ . The initial, independent-particle Hamiltonian,  $H_0$ , is made up by the effective and kinetic potentials. To introduce QSGW in general terms, we leave the form of the effective potential in  $H_0$  open to any static, local or non-local, exchange-correlation potential. The authors of QSGW split  $H$  into  $H_0$  and a residual part,  $H_0 - H$ . This last contribution has to be small to be considered a perturbation, thus leaving the movement of the central bare QP unaffected. To search for the smallest possible residual part, we have to search for an *optimal* effective potential. Kotani and coworkers derived the optimal effective potential through a norm-functional formalism, a derivation which we recast according to Ref. [50] in Sec. 4.2. For now, we give the QSGW equation for the optimized exchange-correlation potential entering  $v_{eff}$ :

$$v_{opt}^{xc} = \frac{1}{2} \sum_{ij} |\psi_i\rangle \{ Re[\Sigma_{xc}(\epsilon_i)]_{ij} + Re[\Sigma_{xc}(\epsilon_j)]_{ij} \} \langle \psi_j|, \quad (4.2)$$

For the single-particle states,  $\psi_i$ , we collect band number and  $\mathbf{k}$ -point in the index  $i$ , and the expression  $[ ]_{ij}$  signals matrix elements with respect to these states. Once the new effective potential is available, we can update the Hamiltonian perturbatively and solve the secular equation. With the new  $\{\psi_i\}$ , a new  $v_{eff}$  stands for the next correction to  $H_0$ . After convergence, the single-electron state  $\psi_i$  becomes the quasiparticle wavefunction  $\Psi_i$  with associated eigenvalue  $E_i$ .

Like in all other methods discussed here, QSGW is not exempt of approximations. Because the self-energy in Eq. 4.2 follows the GWA, it inherits the approximations therein; namely, neglecting vertex corrections. In addition, the optimized potential is static, *i.e.*, the evaluation at the two eigenvalues removes the energy dependence of the self-energy, and also hermiticity is forced. Although the neglected imaginary part of the self-energy does have a physical meaning (related to the life-time of QPs), it does not influence the electronic structure.

## 4.2 Energy Minimization

Based on the work and findings of Ismail-Beigi in Refs. [50–52], we explain the background to Eq. 4.2. The optimized exchange-correlation potential,  $v_{opt}^{xc}$ , in the QSGW guarantees that the energy functional of  $G$  reaches its *lowest value* upon variation. The measure by which we define *lowest* is the squared length of the functional derivative. To clarify this minimization procedure, we look at the variation principle behind the KS scheme.

Equation 2.19 defines the energy functional in the KS scheme,  $E[\rho_0]$ , with respect to the non-interacting density,  $\rho_0$ . As explained in Sec. 2.2.2, when the variation of  $E[\rho_0]$  is set to zero, tight to the constraint of normalized eigenvectors, the solution corresponds to the groundstate of the system.

<sup>1</sup>Sum rule:

$$\int_0^{\infty} \omega Im\{\epsilon_{GG}^{-1}(\mathbf{k}, \omega)\} d\omega = -2\pi\rho,$$

being  $\rho$  the electron density. In words: The sum of all excitations (or oscillations in occupation numbers) does not change the overall particle number [18].

Baring in mind the equivalence between  $\rho$  and  $G$ , the definition of  $\Sigma_{xc}$  from the variation of the exchange-correlation functional  $\Phi_{xc}$  in the LW theory (Eq. 4.1) resembles the DFT case. Based on these analogies and the variational principle, it is tempting to copy the procedure in DFT and try to minimize the total energy functional of  $G$  to find the GS of the interacting system. Much like  $\rho_0$  in DFT, the extremizing  $G$  of the energy functional leads to the ground-state energy of the *interacting* system of dressed QPs. To date, the minimization *à la* KS of such functional is, unfortunately, an impossible task. If we were to find the extremizing  $G$ , we cannot tell whether it is physically possible, nor can we say if the solution is unique. Instead of searching for a minimum in the energy functional, we search for the lowest value of the variation.

For now, we assemble the Hartree potential ( $v_H$ ) and a general exchange-correlation potential ( $v_{xc}$ ), local or non-local, in  $U_0$ , building the independent-particle Hamiltonian:  $H_0 = T + V + U_0$ , with kinetic energy  $T$  and lattice potential  $V$ .  $H_0$  returns the independent-particle states  $|n\rangle$  and their corresponding eigenvalue  $\epsilon_n$ . We recast  $G_0$  in the Dyson equation, using these single-particle states as orthonormal basis:

$$G_0(\omega) = (\omega I - H_0)^{-1} = \sum_n \frac{|n\rangle\langle n|}{\omega - \epsilon_n + i\eta \text{sgn}(\epsilon_F - \epsilon_n)}. \quad (4.3)$$

In order to minimize the energy functional of  $G$ , we first need an energy functional. As in Ref. [51], and borrowing the notation therein, we work with the Klein functional:

$$F[G, G_0] = \int_{-\infty}^{\infty} \frac{d\omega}{2\pi i} e^{i\omega 0^+} \text{tr}\{H_0 G_0(\omega) + I - G_0(\omega)^{-1} G(\omega) \quad (4.4)$$

$$+ \ln[G_0(\omega)G(\omega)] - U_0 G(\omega)\} + E_H[\rho] + \Phi_{xc}[G], \quad (4.5)$$

with Hartree energy (re-writting the second term in the rhs of Eq. 2.18)

$$E_H[\rho] = \frac{1}{2} \int \int \rho(\mathbf{r}) v(\mathbf{r}, \mathbf{r}') \rho(\mathbf{r}') d\mathbf{r} d\mathbf{r}' = \frac{1}{2} \int v_H(\mathbf{r}) \rho(\mathbf{r}) d\mathbf{r}. \quad (4.6)$$

At a first glance, and assuming a rigid lattice, the variable components of the energy functional in Eq. 4.5 are  $U_0$  and  $\Sigma_{xc}$ . The former conditions  $H_0$ , also  $G_0$ , but the latter changes  $\Phi_{xc}$  and  $G$ . To find the variation of  $F$  we must keep a component fixed and vary the rest accordingly. Ismail-Beigi proves that  $F$  is independent of variations of  $U_0$  or, equivalent,  $G_0$  [52]. Thus, keeping  $G$  fixed and varying  $G_0$  is no option. As a side remark, this also means that the choice of the initial guess does not influence the outcome. On the other hand, varying  $G$  with a fixed  $G_0$  gives:<sup>2</sup>

$$\delta F|_{G_0} = \int_{-\infty}^{\infty} \frac{d\omega}{2\pi i} e^{i\omega 0^+} \text{tr}\{-G_0^{-1}(\omega) \delta G(\omega) + G^{-1}(\omega) \delta G(\omega) \quad (4.7)$$

$$- U_0 \delta G(\omega)\} + \delta E_H[\rho] + \delta \Phi_{xc}[G]. \quad (4.8)$$

In the following, we leave out the argument  $\omega$  for simplicity. Based on the definitions in Eqs. 4.1 and 4.6, the variation of  $E_H$  and  $\Phi_{xc}$  convey the Hartree potential and the self-energy, respectively, each multiplied by  $\delta G$ . Splitting the independent-particle potential like  $U_0 \delta G = v_H \delta G + v_{xc} \delta G$ , the resulting  $v_H \delta G$  term cancels with  $\delta E_H$ . Factorizing  $\delta G$  out, the square parenthesis in the functional variation reads  $[G^{-1} - G_0^{-1} + \Sigma_{xc} - v_{xc}] \delta G$ . In order to replace  $\delta G$ , we use the Dyson equation with fixed  $G_0$  to parametrize  $G$  by a trial self-energy,  $\Sigma_t$ :

$$G^{-1} = \omega I - T - V_{ion} - v_H - \Sigma_t = G_0^{-1} - [\Sigma_t - v_{xc}] \Rightarrow \delta G = G \delta \Sigma_t G. \quad (4.9)$$

<sup>2</sup>Here we use the relation of determinants  $\delta \text{tr}\{\ln(A)\} = \text{tr}\{A^{-1} \delta A\}$ .

The next challenge is to delimit our search space: what candidate for  $G$  is physically sound? It is reasonable to choose  $G_0$  in order to replace  $G$ , because  $G_0$  is already connected to a physically grounded Hamiltonian. Replacing  $G$  with  $G_0$  reduces the expression in the square parenthesis by nullifying the first two terms in the trace. Replacing  $\delta G_0$  as prescribed in Eq. 4.9, the expression becomes:<sup>3</sup>

$$2\pi i \frac{\delta F}{\delta \Sigma_t} = Tr\{G_0[\Sigma_{xc} - v_{xc}]G_0\} \quad (4.10)$$

$$\text{with } Tr\{A\} = \int_{-\infty}^{\infty} \frac{d\omega}{2\pi i} e^{i\omega 0^+} tr\{A\}. \quad (4.11)$$

Equation 4.10 is indeed the target question: which trial self-energy brings the gradient to its lowest value? We take the square of the length of the matrix in Eq. 4.10, symbolized as  $\|D_0\|^2$ , and calculate its value in the basis of  $|n\rangle$ , advantageous in that  $G_0$  is diagonal in this basis:

$$\|D_0(\omega)\|^2 = \int_{-\infty}^{\infty} \sum_{nl} \frac{|\langle n|\Sigma_{xc}(\omega) - v_{xc}|l\rangle|^2}{[(\omega - \epsilon_n) + \eta^2][(\omega - \epsilon_l) + \eta^2]}. \quad (4.12)$$

$v_{xc}$  is to be freely chosen, aiming at the smallest  $\|D\|^2$  possible. We look inside the sum, and search for the most adequate choice of  $v_{xc}$ , which fulfills our goal for every pair  $(n, l)$  in the integral. The integral transforms in a closed contour integral in the upper-half of the complex plane.<sup>4</sup>

- **Case  $n = l$**

To simplify the notation, and because we center the attention on the poles coming from the denominator, we write the nominator  $N(\omega) = |\langle n|\Sigma_{xc}(\omega) - v_{xc}|n\rangle|$ , with derivative  $N'(\omega) = \langle n|d\Sigma_{xc}(\omega)/d\omega|n\rangle$ . We investigate the poles at  $\epsilon_n + i\eta$ . The denominator is recast in a product,  $[(\omega - \epsilon_n)^2 + \eta^2]^2 = [\omega - \epsilon_n + i\eta]^2[\omega - \epsilon_n - i\eta]^2$  to fit the Cauchy formula

$$2\pi i \frac{d}{d\omega} \left\{ \frac{N^2(\omega)}{[\omega - \epsilon_n + i\eta]^2} \right\} \Big|_{\omega=\epsilon_n+i\eta} = \frac{\pi}{2\eta^3} N^2(\omega) - \frac{i\pi}{\eta^2} N(\omega)N'(\omega). \quad (4.13)$$

The leading term scales as  $\eta^{-3}$ , and the poles coming from  $N(\omega)$  contribute to a lesser extent than the two terms above. The resulting matrix has real and imaginary parts,  $N(\omega) = \langle n|Re[\Sigma_{xc}(\omega)] - v_{xc}|n\rangle + \langle n|Im[\Sigma_{xc}(\omega)]|n\rangle$ . Because the only tunable component,  $\langle n|v_{xc}|n\rangle$ , returns a real number, to make the leading term in the integral reach zero, the imaginary part is necessarily zero. We are left with  $\langle n|Re[\Sigma(\epsilon_n)]|n\rangle = \langle n|v_{xc}|n\rangle$  as the only choice for the lowest square gradient, such that the leading term in Eq. 4.13 disappears, and the only contribution comes from the poles in  $N(\omega)$ , which scale as  $\eta^{-1}$ . Concerning the term  $\propto \eta^{-2}NN'$ , it cancels out when we expand Eq. 4.13 in series in  $\eta$ .

- **Case  $n \neq l$**

We recycle the notation from the previous case, but only now  $N(\omega)$  refers to off-diagonal matrix elements. The denominator provides the largest contribution, namely two poles:  $\epsilon_n + i\eta$  and  $\epsilon_l + i\eta$ . We go about this integral (the same as in Eq. 4.12) following the steps explained

<sup>3</sup>We make use of the cyclicity of the trace:  $tr(G_0\delta\Sigma G_0) = tr(G_0G_0\delta\Sigma)$

<sup>4</sup>We make use of the standard Cauchy integral formula

$$2\pi i f'(a) = \oint \frac{f(z)}{(z-a)^2}$$

in the previous case. The contributions from these two simple poles are:

$$\frac{\pi}{\eta} \frac{N^2(\epsilon_n) + N^2(\epsilon_l)}{(\epsilon_n - \epsilon_l)^2}, \quad (4.14)$$

where we evaluate  $\Sigma_{xc}$  at different energies. For the first term in the numerator, we have  $\langle n | \text{Re}[\Sigma(\epsilon_n)] | l \rangle$  and  $\langle n | v_{xc} | l \rangle$  to the second power, but also  $-2\langle n | v_{xc} | l \rangle \langle n | \text{Re}[\Sigma(\epsilon_n)] | l \rangle$ , since we neglect the imaginary part. Putting both terms in the numerator together, we end up with a quadratic, whose derivative we set to zero. The derivative is greatly simplified by regarding only variable terms, namely those including the matrix elements  $(v_{xc})_{nl} = \langle n | v_{xc} | l \rangle$ :

$$\frac{d}{d(v_{xc})_{nl}} [-2\langle n | v_{xc} | l \rangle (\langle n | \text{Re}[\Sigma(\epsilon_n)] | l \rangle + \langle n | \text{Re}[\Sigma(\epsilon_l)] | l \rangle) + 2\langle n | v_{xc} | l \rangle^2] = 0 \quad (4.15)$$

$$\langle n | v_{xc} | l \rangle = \frac{\langle n | \text{Re}[\Sigma(\epsilon_n)] | l \rangle + \langle n | \text{Re}[\Sigma(\epsilon_l)] | l \rangle}{2} \quad (4.16)$$

For the *special case* of degenerate states, *i.e.*,  $\epsilon_n = \epsilon_l$ , the integral in Eq. 4.12 becomes Eq. 4.13, though the matrix elements are  $\langle n | \Sigma_{xc}(\omega) - v_{xc} | l \rangle$ .

In conclusion, the choice of the optimized potential in QSGW delivers the shortest gradient of the Klein functional. This mathematical formulation treats a general self-energy, which does not necessarily fit the GWA definition.<sup>5</sup> However, in this project we follow the recipe suggested in Ref. [12] and stay within the GWA. The dependence on  $v_{xc}$  to obtain  $\epsilon_n$ , and later  $\Sigma_{xc}$ , leads to non-linearity, implying a self-consistency search for the optimized potential.

### 4.3 Independent or Interacting Systems?

QSGW “scans” the space of non-interacting  $G_0$  to find the best candidate; namely, the closest to  $G$ . If successful, this operation leads to the  $G_0$  for which  $\|D\|$  is minimized, and however close it is to  $G$  it is strictly speaking a non-interacting Green’s function. Despite this, and in order to straighten out the terminology for the coming chapter, we differentiate the initial guess for the Green’s function from the converged one given by the QSGW: the first remains  $G_0$  and the second simply  $G$ . Also,  $G$  is describing “bare” QPs that are very close to their “dressed” counterpart. That is, the IP system evolves to a many-body problem, where interactions between QPs are embedded in the  $\Sigma_{xc}$ .

Also to clarify the wording for the coming chapters, electrons in any mean-field approach are simply called particles. For all other frameworks including many-body effects, such as screening, we refer to quasiparticles. The first purpose is to avoid the adjectives “bare” and “dressed”, its continuous usage may confuse. The second goal is to connect the particles in the IP schemes to the non-interacting, or bare, particles in the Landau-Silin picture.

---

<sup>5</sup>The choice of self-energy is not without preconditions:  $\Sigma_{xc}$  must fulfill Eq. 4.1.



## Chapter 5

# Linearized Augmented Planewaves

In any mean-field approximation, the solution to the single-particle Schrödinger-like equations require a suitable representation of the one-electron states. This Chapter details the representation of the wavefunctions (WF), for groundstate (GS) and excited states calculations. Hereby, we denote the single-particle WF after its  $\mathbf{k}$ -dependency and band index:  $\psi_{n\mathbf{k}}(\mathbf{r})$ .

Since  $\psi_{n\mathbf{k}}(\mathbf{r})$  is an infinitely differentiable function —continuous in an interval—, it can be expressed as a linear combination of an complete basis function set,  $\{\phi_p(\mathbf{r}), p = 1, \dots \infty\}$ , made up by functions which are orthonormal in that interval. In general, the expansion of the  $n$ -th WF for a particular  $\mathbf{k}$ -vector in the first Brillouin zone is:

$$\psi_{n\mathbf{k}}(\mathbf{r}) = \sum_{\mathbf{G}} C_{n\mathbf{G}}^{\mathbf{k}} \phi_{\mathbf{k}+\mathbf{G}}(\mathbf{r}), \quad (5.1)$$

with expansion coefficient  $C_{n\mathbf{G}}^{\mathbf{k}}$  —variational coefficients— and  $\mathbf{G}$  a reciprocal lattice vector. In the following, I discuss three choices of basis set  $\{\phi_{\mathbf{k}+\mathbf{G}}\}$  and the truncation of the series to a finite number. At the end, I examine the treatment of core states and the implementation in **exciting** of a mix basis set for excited states calculations.

### 5.1 APW Basis

Planewaves (PWs), which follow Bloch's theorem for the crystal potential, are an example of a complete basis set. They are suitable for the description of independent particles which can justifiably represent electrons near the Fermi surface. However, the rapid varying potential near the nucleus demands a very large number of PWs for the accurate description of the WF in this region. Alternatively, through an augmentation, *i.e.*, modification of PW, the WF can be carefully represented near the core. This approach is known as *Augmented Planewaves* (APW) method, introduced by Slater in 1937 [53]. He aimed at a better representation of low-energy electrons, for which PW methods converged far too slowly. Although today the APW basis by itself is rarely used, it sets the ground for improved methods, employed here.

The APW basis rests in the similarity between the potential near the nucleus in a periodic crystal and that of the free atom. In the neighborhood around the nucleus, the potential energy becomes infinitively negative and away from the nucleus, it approaches a constant. Dividing the space accordingly, non-overlapping spheres centered at the nucleus delimit the region called *muffin tin* (MT), shown in Fig. 5.1. The center of the sphere is placed at the nucleus and has position  $\mathbf{r}_\alpha$  and radius  $\mathbf{R}_{MT}^\alpha$ , where the subindex  $\alpha$  refers to the atom. Away from the nucleus, the spherical potential varies slowly and it smoothly joins the potential near the next nucleus. Following this space partition, the APW describes the WF inside the spheres as solutions to the atomic SE. These solutions transfer their atomic-like character to the electron wavefunction in this region. Beyond  $\mathbf{R}_{MT}^\alpha$ , linear combinations of PW build the WF, filling the interstitial region (IR) between the MT spheres, called *interstitial PW* (IPW).

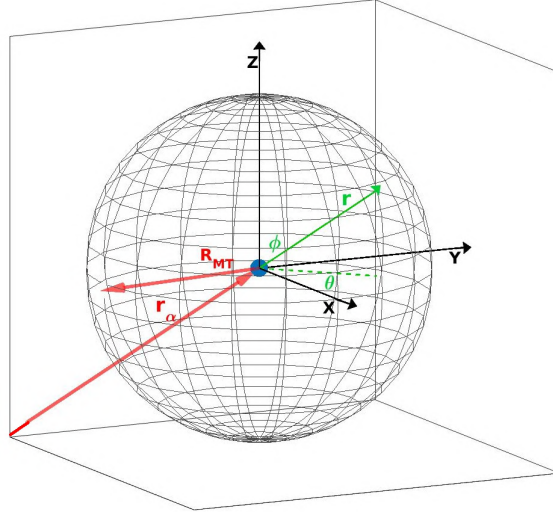


Figure 5.1: 3D representation of space partition of the unit cell in the APW method. Spherical coordinates define angles between arbitrary position vector  $\mathbf{r}$  (green) and  $x$ -axis (black). In red,  $\mathbf{r}_\alpha$  is the position vector of the center of the nucleus,  $\mathbf{R}_{MT}$  is the MT radius. Positions in space are saved in a grid within the MT.

In a unit cell of volume  $\Omega$ , a basis function at position  $\mathbf{r}$  (see Figure 5.1) in the APW method is defined as:

$$\text{APW } \phi_{\mathbf{k}+\mathbf{G}}(\mathbf{r}) = \begin{cases} \frac{1}{\sqrt{\Omega}} e^{i(\mathbf{k}+\mathbf{G})\cdot\mathbf{r}}, & \mathbf{r} \in IR \\ \sum_{l=0}^{\infty} \sum_{m=-l}^{-l} A_{lm\alpha}^{\mathbf{k}+\mathbf{G}} u_{\alpha l}(r', \epsilon_{n\mathbf{k}}) Y_l^m(\hat{\mathbf{r}}'), & \mathbf{r} \in MT \end{cases} \quad (5.2)$$

with  $\mathbf{r}' = \mathbf{r} - \mathbf{r}_\alpha$ , and  $l$  and  $m$  the *azimuthal quantum number* and the *magnetic quantum number*, respectively.  $\hat{\mathbf{r}}'$  is the direction of the  $\mathbf{r}'$  vector given by the angles in Fig. 5.1. The basis set within the MT spheres consists of solutions to the equation:

$$\left[ -\frac{d^2}{dr^2} + \frac{l(l+1)}{r^2} + V_\alpha(\mathbf{r}) - \epsilon_{n\mathbf{k}} \right] r u_{l\alpha}(|\mathbf{r} - \mathbf{r}_\alpha|, \epsilon_{n\mathbf{k}}) = 0, \quad (5.3)$$

and spherical harmonics,  $Y_l^m(\hat{\mathbf{r}}')$ , defined in Eq. C.1.

In Eq. 5.2, the expansion coefficients,  $A_{lm\alpha}^{\mathbf{k}+\mathbf{G}}$ , guarantee the continuity of APW at the sphere boundary, thus they are called *matching coefficients*. To determine  $A$  for a specific  $lm$ -component and  $(\mathbf{k} + \mathbf{G})$ -vector, we set  $\phi^{MT}(\mathbf{R}_{MT}^\alpha) = \phi^{IR}(\mathbf{R}_{MT}^\alpha)$ , since, for continuity, the *value* of both the MT basis function and PW should be equal at the sphere boundary. We arrive at (to simplify,  $\mathbf{R}^{MT}$  is  $\mathbf{R}$ ):

$$A_{lm\alpha}^{\mathbf{k}+\mathbf{G}} = \frac{i^l 4\pi e^{i(\mathbf{k}+\mathbf{G})\cdot\mathbf{R}}}{\sqrt{\Omega} u_{l\alpha}(R, E_{\alpha l})} j_l(|\mathbf{k} + \mathbf{G}|R) [Y_l^m]^*(\widehat{\mathbf{k} + \mathbf{G}}), \quad (5.4)$$

with  $j_l(kr)$  the spherical Bessel function. The sum over  $l$  in Eq. 5.2 is in principle infinite, though, in practice, we truncate it to a finite number,  $l_{max}$ . This parameter is chosen in order to match the maximal numbers of nodes of  $\phi_{\mathbf{k}+\mathbf{G}}$  inside and outside the MT *on the MT surface*. The maximal value of nodes on the MT surface is  $2l_{max}$ , given the inbuilt Legendre polynomial,  $P_l^m$ , from  $Y_l^m(\hat{\mathbf{r}}')$ . In the circumference of the MT,  $2\pi\mathbf{R}_{MT}^\alpha$ , this maximum number of nodes is  $l_{max}/\pi\mathbf{R}_{MT}^\alpha$ . From the opposite side of the MT boundary, the PW has two nodes per unit length (with largest wave-number  $k_{max}$  and shortest period  $2\pi/k_{max}$ ), returning a maximal number of nodes of  $k_{max}/\pi$ . Taking both maximum number of nodes, an acceptable choice for the cutoff is:  $l_{max} = \mathbf{R}_{MT}^\alpha \cdot \mathbf{k}_{max}$  [54].

Preferably,  $\mathbf{R}_{MT}^\alpha$  should not change much among species in the unit cell, making the choice of

$l_{max}$  useful for different atoms. Besides  $l_{max}$ , the number of basis functions is largely determined by the number of PW, given by  $k_{max} = |\mathbf{k} + \mathbf{G}|_{max}$ . To set the cut-off of the PW basis, a reasonable parameter is the dimensionless product  $\mathbf{R}_{MT}^\alpha \cdot |\mathbf{k} + \mathbf{G}|_{max}$ .

An inconvenient aspect of the APW method is the non-linearity of Eq. 5.3 due to the dependence on  $\epsilon_{n\mathbf{k}}$  [55]. Because this energy enters the basis functions, the Hamiltonian also depends on  $\epsilon_{n\mathbf{k}}$ . In principle,  $\epsilon_{n\mathbf{k}}$  is an eigenvalue of the secular equation for the one-particle Hamiltonian, hence unknown *a priori*, and the secular equation becomes a non-linear problem.

Alternatively, we may choose an energy,  $E_l$ , for each  $l$ , entering Eq. 5.3 and fix it. The first disadvantage of this scheme lies in its inability to describe bands with equal  $l$ , but different principal quantum number. It is reasonable to separate core states —highly localized within the MT— from valence states. Unfortunately, this task is not straightforward for poorly localized core electrons, called semi-core states. In addition, some bands, for instance  $d$ -orbitals, in the MT may have non-spherical character, making it impossible to assign a unique  $E_{\alpha l}$  for these cases. A second problem, is the deviation from the band energy,  $\epsilon_{n\mathbf{k}}$ , introduces an error  $O(E_{\alpha l} - \epsilon_{n\mathbf{k}})$  for calculated WF and  $O(E_{\alpha l} - \epsilon)^2$  for the total energy. Also counterproductive to the APW method are the values of  $\epsilon_{n\mathbf{k}}$  for which  $u_{l\alpha}(|\mathbf{r} - \mathbf{r}_\alpha|, \epsilon_{n\mathbf{k}}) = 0$ , known as the *asymptotic problem*, because of the vanishing denominator in Eq. 5.4. Due to these drawbacks, it is desirable to improve upon the APW method, targeting these issues.

## 5.2 LAPW basis

By fixing the energy in Eq. 5.3, we enter an error in the solution, due to the approximation  $\epsilon_{n\mathbf{k}} \approx E_{l\alpha}$ . In 1975, Ole Krogh Andersen proposed the *Linearized Augmented Planewaves* (LAPW) method, which reduces this error in APW [56]. This method introduces the derivation of  $u_{l\alpha}(|\mathbf{r} - \mathbf{r}_\alpha|, \epsilon_{n\mathbf{k}})$  with respect to energy,  $\dot{u}_{l\alpha}(|\mathbf{r} - \mathbf{r}_\alpha|, E_{l\alpha})$ , through a Taylor-like expansion of the radial solution. This approach returns a linearized APW, hence the name of the method. The basis in the interstitial part in LAPW follows Eq. 5.2, while the MT part, using fixed  $E_{\alpha l}$  values, is defined as:

$$\text{LAPW } \phi_{\mathbf{k}+\mathbf{G}}(\mathbf{r}) = \sum_{lm} \left[ A_{lm\alpha}^{\mathbf{k}+\mathbf{G}} u_{l\alpha}(|\mathbf{r} - \mathbf{r}_\alpha|, E_{l\alpha}) + B_{lm\alpha}^{\mathbf{G}+\mathbf{k}} \dot{u}_{l\alpha}(|\mathbf{r} - \mathbf{r}_\alpha|, E_{l\alpha}) \right] Y_l^m(\hat{\mathbf{r}}). \quad (5.5)$$

We evaluate  $u_{l\alpha}$  and its derivative at a fixed  $E_{\alpha l}$ , called *linearization energy*. The functions  $u_{l\alpha}(|\mathbf{r} - \mathbf{r}_\alpha|, E_{l\alpha})$  and  $\dot{u}_{l\alpha}(|\mathbf{r} - \mathbf{r}_\alpha|, E_{l\alpha})$  are orthogonal to each other, facilitating the calculation of the Hamiltonian matrix elements. Analogous to  $A$ , the coefficient  $B$  ensures the continuity of  $\dot{u}_{l\alpha}(|\mathbf{r} - \mathbf{r}_\alpha|, E_{l\alpha})$  at the sphere boundary. Whenever  $u_{l\alpha}(|\mathbf{r} - \mathbf{r}_\alpha|, E_{l\alpha}) = 0$ , its derivative is non-zero, fixing the asymptotic problem of APWs.

To appoint a value to  $E_{\alpha l}$ , we base our criteria on the Wigner-Seitz rules [57]. It is usually taken as the energy of the middle of the band; an average between the top and bottom energies of the band. In **exciting**, given an initial energy, the algorithm scans upwards through a number of equidistant energy values till  $u_{l\alpha}(|\mathbf{r} - \mathbf{r}_\alpha|, \epsilon_{n\mathbf{k}})$  becomes zero at the MT boundary. The  $E_l$  fulfilling this criteria is the top band value. Restarting from this point, the search through energy values takes place downwards, till  $\dot{u}_{l\alpha}(|\mathbf{r} - \mathbf{r}_\alpha|, E_{l\alpha})$  becomes zero. This last energy is the energy at the bottom of the band, and we calculate the average. For occupied states, the values of atomic bands energies are already a good initial value for  $E_l$ , which are employed in **exciting** [58].

For the sake of continuity, the values of both the radial function and its slope match that of the PW at the MT boundary. Adding  $\dot{u}_{l\alpha}(|\mathbf{r} - \mathbf{r}_\alpha|, E_{l\alpha})$  complicates the continuity with respect to APW method, as the LAPW need to match two functions at the MT boundary, not just  $u_{l\alpha}(|\mathbf{r} - \mathbf{r}_\alpha|, \epsilon_{n\mathbf{k}})$ . The inclusion of  $\dot{u}_{l\alpha}(|\mathbf{r} - \mathbf{r}_\alpha|, E_{l\alpha})$  changes the form of the basis functions within the MT, where the LAPW method demands more basis functions to reach a smooth transition from MT to IR [59].

### 5.3 (L)APW+LO basis

LAPW cures many of the mentioned defects in APW, nevertheless semi-core states —*i.e.* extended core states— are troublesome to describe when fixing  $E_l$ . As an example, some states may lie too low in energy to be considered valence states, and at the same time may be too delocalized to be treated as a core state. There is hardly a parameter  $E_l$  which fits the description of those semi-core states at the same time as describing valence states sharing the same  $l$  number. If a certain value for  $E_{\alpha l}$  is suitable to describe a semi-core state, it may already be employed to describe a higher-energy valence state. Likewise, the linearization energy in the (L)APW basis may be far too low for high-energy states, *i.e.*, excited states.

In addition, the difference ( $E_{\alpha l} - \epsilon_{n\mathbf{k}}$ ) accounts for error, although to a lesser extent after linearization of the radial functions. It would be convenient to linearize the MT basis functions in the APW, without the need to increase the number of IPW.

An option is to improve the (L)APW basis functions by adding new functions, called *local orbitals* (LO), with fixed energy parameter [60, 61]. Outside the MT, these functions disappear. This extra set of functions serves particularly well to describe semi-core states *and* excited states, because it employs new energy parameters not included in the LAPW radial functions. Semi-core and valence states are treated on equal footing, by including explicitly the energy of the former state in LOs. For conduction bands, higher linearization energies can be included in LOs, which were not originally present in LAPWs, giving the LAPW+LO basis enough flexibility to tailor the description of excited states. For the APW method, this extra set of functions enables for linearization within the MT, without the augmentation of PWs outside the MT. Local orbitals are defined as:

$$\text{LO } \phi_{\mu}(\mathbf{r}) = \begin{cases} \delta_{\alpha\alpha\mu} \delta_{ll\mu} \delta_{mm\mu} [a_{\mu} u_{l\alpha}(|\mathbf{r} - \mathbf{r}_{\alpha}|, E_{l\alpha}) + b_{\mu} \dot{u}_{l\alpha}(|\mathbf{r} - \mathbf{r}_{\alpha}|, E_{l\alpha})] Y_l^m(\hat{\mathbf{r}}), & r \in MT \\ 0, & r \in I. \end{cases} \quad (5.6)$$

Much like in Sec. 5.2, an expansion of the  $u_{l\alpha}(|\mathbf{r} - \mathbf{r}_{\alpha}|, E_{l\alpha})$  to first-order (or higher-order) derivatives lowers the error in the calculated total energy. Ultimately, second- or higher-order derivatives may also enter the linear combination of Equation 5.6, achieving an  $O(E_{\alpha l} - \epsilon)^8$  error in total energy. The coefficients  $a_{\mu}$  and  $b_{\mu}$  in Eq. 5.6 ensure that  $\text{LO } \phi_{\mu}(\mathbf{r})$  goes to zero at the boundary and that its integral throughout the MT volume equals one. This method, named (L)APW + LO, allows for more flexibility by tailoring basis sets to physically meaningful states at a very low cost; the basis set size increases by a few numbers.

### 5.4 Core States

These low-energy electron states remain within the MT sphere, thus their functions don't need to match a PW of the interstitial region. All-electron schemes, such as (L)APW, usually solve the secular equations for core electrons independently from the rest of the electrons. It is custom to set this eigenvalue problem within boundary conditions resembling the isolated atom. Therefore, the resulting density of core electrons is spherically symmetrical. In this project we treat core electrons explicitly, in the independent particle schemes as well as in the many-body approaches.

### 5.5 Mixed Basis Set

Often the product of two functions  $\psi_{n\mathbf{k}}$  appears in the matrix form of operators in the Hedin's equations. To simplify matters and avoid recalculating these products, we make use of a basis set  $\{\chi_i^{\mathbf{q}}\}$ ; namely the *mix basis set*, or MB for short, to expand the product of WFs [62, 63]. The expansion coefficients are labeled  $M_{nm}^i(\mathbf{k}, \mathbf{q})$ , where  $n$  and  $m$  stand for states of the WFs making up the product, and  $i$  is the index of the MB function. Employing the MB, we represent two-body

operators in matrix form, represented by  $O_{ij}(\mathbf{r}, \mathbf{r}'; \omega)$ , with frequency dependence not necessarily present. The expansion of the wavefunctions product, its coefficients, and the expansion of two-body operators in the MB and its matrix representation are summarized below:

$$\psi_{n\mathbf{k}}(\mathbf{r})\psi_{m\mathbf{k}-\mathbf{q}}^*(\mathbf{r}) = \sum_i M_{nm}^i(\mathbf{k}, \mathbf{q})\chi_i^{\mathbf{q}}(\mathbf{r}), \quad M_{nm}^i(\mathbf{k}, \mathbf{q}) \equiv \int_{\Omega} [\chi_i^{\mathbf{q}}(\mathbf{r})\psi_{m\mathbf{k}-\mathbf{q}}(\mathbf{r})]^*\psi_{n\mathbf{k}}(\mathbf{r}) d\mathbf{r} \quad (5.7)$$

$$O(\mathbf{r}, \mathbf{r}'; \omega) = \sum_{\mathbf{q}} \sum_{ij}^{BZ} \chi_i^{\mathbf{q}}(\mathbf{r})O_{ij}(\mathbf{q}, \omega)[\chi_j^{\mathbf{q}}(\mathbf{r}')]^*, \quad O_{ij}(\mathbf{q}, \omega) = \int_V [\chi_i^{\mathbf{q}}(\mathbf{r})]^* O(\mathbf{r}, \mathbf{r}'; \omega)\chi_j^{\mathbf{q}}(\mathbf{r}') d\mathbf{r} d\mathbf{r}', \quad (5.8)$$

with the whole crystal space  $V = N_c\Omega$  and  $N_c$  the number of unit cells. Within  $V$ , the functions  $\chi_i^{\mathbf{q}}$  are normalized to unity. These functions are Bloch functions, such that  $\chi_i^{\mathbf{q}}(\mathbf{r} - \mathbf{R}) = e^{-i\mathbf{q}\cdot\mathbf{R}}\chi_i^{\mathbf{q}}(\mathbf{r})$ , with  $\mathbf{R}$  a Bravais lattice vector. This property allows for the integration over one unit cell rather than the whole volume.

Following the APW method, the construction of the MB functions employs the space partition between interstitial region (IR) and muffin tin (MT) spheres. A function  $\chi_i^{\mathbf{q}}$  belongs to either the former or the latter space, giving rise to two types of MB functions: (i) products of radial functions together with spherical harmonics or (ii) products of plane waves.

Inside a sphere surrounding an atom labeled  $\alpha$ , the product of two MT basis functions is:<sup>1</sup>

$$u_{\alpha l}^*(r^\alpha)Y_{lm}^*(\hat{\mathbf{r}}^\alpha)u_{\alpha l'}(r^\alpha)Y_{l'm'}(\hat{\mathbf{r}}^\alpha). \quad (5.9)$$

The resulting radial product functions are neither normalized nor orthogonal. An effective method to ensure linear independence among the products of radial functions is to diagonalize their overlap matrix, calculated as an integral over space within the MT:

$$\mathcal{O}_{ll';l_1l'_1} = \int_0^{\mathbf{R}_{MT}^\alpha} u_{\alpha l}(r^\alpha)u_{\alpha l'}(r^\alpha)u_{\alpha l_1}(r^\alpha)u_{\alpha l'_1}(r^\alpha)(r^\alpha)^2 dr^\alpha, \quad (5.10)$$

which will return a set of eigenvalues and eigenvectors,  $\{\lambda_N, c_{ll',N}\}$  [62]. All eigenvalues with values larger than to a certain threshold, correspond to eigenvectors assumed to be linearly dependent and therefore discarded [62]. Next, we build the product of radial functions as a linear combination consisting of the eigenvectors corresponding to selected eigenvalues and radial functions:

$$\nu_{\alpha NL}(r^\alpha) = \sum_{l'} c_{ll',N} u_{\alpha l}(r^\alpha)u_{\alpha l'}(r^\alpha). \quad (5.11)$$

The product of two radial functions  $u_l$  and  $u_{l'}$  is subject to two conditions: (i)  $l$  and  $l'$  fall under a threshold  $l_{max}^{MB}$ , further reducing the MB size, and (ii)  $l$  and  $l'$  meet the triangular condition  $|l - l'| \leq L \leq l + l'$ .

For the angular part, the product of two spherical harmonics can be expanded in a linear combination of spherical harmonics  $Y_L^M$  expressed in Eq. C.3. For each wavevector  $\mathbf{q}$ , and according to crystallographic translations, we arrive at the mixed product basis for the MT:

$$\gamma_{\alpha NLM}^{\mathbf{q}}(\mathbf{r}) = e^{i\mathbf{q}\cdot\mathbf{r}^\alpha} \nu_{\alpha NL}(r^\alpha)Y_L^M(\hat{\mathbf{r}}^\alpha) \quad (5.12)$$

The set  $\{\nu_{\alpha NL}\}$  does not include the derivate of the radial function in Eq. 5.5 due to its negligible

<sup>1</sup>Here,  $\alpha = \alpha'$ , because the product of MT functions from different spheres is zero.

contribution, setting  $B_{lm}^{\mathbf{G}+k}$  in Eq. 5.5 to zero and therefore reducing the LAPW basis set to APW [62]. However, in **exciting** we include the functions  $\dot{u}_{l\alpha}(|\mathbf{r} - \mathbf{r}_\alpha|, E_{l\alpha})$  from local orbitals by absorbing them in the coefficients of the expansion at the left in Eq. 5.7.

For the IR, the product of two IPWs returns a PW, however these PWs are not necessarily orthonormal. Analogous to Eq. 5.10, we calculate the overlap matrix of the plane wave products:

$$\mathcal{O}_{\mathbf{G}\mathbf{G}'} = \frac{1}{\Omega} \int_{\Omega} \theta(\mathbf{r}) e^{i(\mathbf{G}-\mathbf{G}')\cdot\mathbf{r}} d\mathbf{r}. \quad (5.13)$$

The step function  $\theta(\mathbf{r})$  guarantees that the integral is zero if  $\mathbf{r}$  resides outside the IR. In the integral above, we see the Fourier transform of the step function which has the solution:

$$\tilde{\theta}_{\mathbf{G}} = \begin{cases} 1 - \sum_{\alpha} \frac{V_{MT}^{\alpha}}{\Omega}, & \mathbf{G} = 0 \\ -3 \sum_{\alpha} \frac{V_{MT}^{\alpha}}{\Omega} e^{i\mathbf{G}\cdot\mathbf{r}_{\alpha}} \frac{\sin(GR_{\alpha}^{MT}) - GR_{\alpha}^{MT} \cos(GR_{\alpha}^{MT})}{(GR_{\alpha}^{MT})^3}, & \mathbf{G} \neq 0 \end{cases} \quad (5.14)$$

$V_{MT}^{\alpha}$  stands for the volume of the MT. After diagonalizing the overlap matrix  $\mathcal{O}_{\mathbf{G}\mathbf{G}'}$  and dividing each eigenvector by the square root of its eigenvalue,  $\tilde{S}_{\mathbf{G}i} \equiv S_{\mathbf{G}i}/\sqrt{\lambda_i}$ , we arrive at the IPW for each wavevector  $\mathbf{q}$  in the MB:

$$P_i^{\mathbf{q}}(\mathbf{r}) \equiv \frac{1}{\sqrt{\Omega}} \sum_{\mathbf{G}} \tilde{S}_{\mathbf{G}i} e^{i(\mathbf{q}+\mathbf{G})\cdot\mathbf{r}} \theta(\mathbf{r}) \quad (5.15)$$

The sum is truncated at a value  $\mathbf{G}_{max}$ . Finally, the MB is as follows:

$$\{\chi_i^{\mathbf{q}}(\mathbf{r})\} = \{\gamma_{\alpha NLM}^{\mathbf{q}}(\mathbf{r}), P_i^{\mathbf{q}}(\mathbf{r})\}. \quad (5.16)$$

Crucial for the calculation of the self-energy and the polarizability matrix are the expansion coefficients  $M_{nm}^i$ . In order to arrive to those coefficients, one basis function in the MB in the set of Eq. 5.16 enters Eq. 5.7. For the MT region, this reads:

$$M_{nm}^i(\mathbf{k}, \mathbf{q}) \equiv \int_{\Omega} [\gamma_{\alpha NLM}^{\mathbf{q}}(\mathbf{r}) \psi_{m\mathbf{k}-\mathbf{q}}(\mathbf{r})]^* \psi_{n\mathbf{k}}(\mathbf{r}) d\mathbf{r} = \int_{\Omega} \sum_{l_1 m_1} \sum_{l_2 m_2} e^{i\mathbf{q}\cdot\mathbf{r}_{\alpha}} \mathcal{A}_{n\mathbf{k}, \alpha l_1 m_1} \mathcal{A}_{m\mathbf{k}-\mathbf{q}, \alpha l_2 m_2} \nu_{\alpha NL}(r) u_{\alpha l_1}(r) u_{\alpha l_2}(r) Y_{l_1 m_1}(\hat{\mathbf{r}}) Y_{l_2 m_2}(\hat{\mathbf{r}}) Y_{LM}(\hat{\mathbf{r}}) d\mathbf{r}, \quad (5.17)$$

with  $\mathcal{A}_{n\mathbf{k}, \alpha lm} = \sum_{\mathbf{G}} C_{n\mathbf{G}}^{\mathbf{k}} A_{lm\alpha}^{\mathbf{k}+\mathbf{G}}$ , the sum over products of expansion coefficients in Eq. 5.1 and Eq. 5.2. The definition of the Gaunt coefficients in Eq. C.4 replaces the angular integral over the product of the three spherical harmonics. Finally, we have to solve the integral:  $\int_0^{R_{MT}^{\alpha}} \nu_{\alpha NL}(r) u_{\alpha l_1}(r) u_{\alpha l_2}(r) r^2 dr$ .

Conversely, for the interstitial region, the product of two step functions is also a step function and the product of three PWs is a PW as well, simplifying the calculation. The resulting step function is

Fourier transformed according to Eq. 5.14.

$$\begin{aligned}
 M_{nm}^i(\mathbf{k}, \mathbf{q}) &\equiv \int_{\Omega} \frac{1}{\sqrt{\Omega}} \left[ \sum_{\mathbf{G}_1} \tilde{S}_{\mathbf{G}_1 i}^* e^{-i(\mathbf{q}+\mathbf{G}_1)\cdot\mathbf{r}} \psi_{m\mathbf{k}-\mathbf{q}}(\mathbf{r}) \right]^* \psi_{n\mathbf{k}}(\mathbf{r}) d\mathbf{r} = \\
 &\left[ \frac{1}{\sqrt{\Omega}} \right]^3 \sum_{\mathbf{G}_1} \sum_{\mathbf{G}} \sum_{\mathbf{G}'} \theta_{\mathbf{G}} \theta_{\mathbf{G}'} \tilde{S}_{\mathbf{G}_1 i}^* e^{-i(\mathbf{q}+\mathbf{G}_1)\cdot\mathbf{r}} C_{n\mathbf{k},\mathbf{G}} e^{i(\mathbf{G}+\mathbf{k})\cdot\mathbf{r}} C_{m\mathbf{k}-\mathbf{q},\mathbf{G}'}^* e^{-i(\mathbf{G}'+(\mathbf{k}-\mathbf{q}))\cdot\mathbf{r}} \\
 &= \frac{1}{\Omega^{\frac{3}{2}}} \sum_{\mathbf{G}_1 \mathbf{G} \mathbf{G}'} C_{n\mathbf{k},\mathbf{G}} C_{m\mathbf{k}-\mathbf{q},\mathbf{G}'}^* \tilde{\theta}_{\mathbf{G}-\mathbf{G}'-\mathbf{G}_1} \tilde{S}_{\mathbf{G}_1 i}^* \quad (5.18)
 \end{aligned}$$



# Part II

## Results



# Chapter 6

## Implementation

This chapter is dedicated to the implementation of QSGW in **exciting**, exposed in general in Sec. 6.1. Numerical calculations based on any independent particle (IP) scheme —introduced in Sec. 2.2— produce a set of independent-particle eigenfunctions and eigenvalues, denoted  $\{\psi_{m\mathbf{k}}^{\text{IP}}(\mathbf{r}), \epsilon_{m\mathbf{k}}^{\text{IP}}\}$ , by which we obtain an *initial* non-interacting Green’s function, using Eq. 3.14. For the rest, we leave out the argument  $\mathbf{r}$  in the text, but include it in the equations. With these results, we calculate the matrix form of the operators in Hedin’s equations: the screened Coulomb interaction,  $W(\omega)$ , and the polarizability,  $P_0(\omega)$ , followed by the bare Coulomb interaction,  $v$ , and the dielectric function,  $\epsilon(\omega)$ , presented in Sec. 6.2. Section 6.3 details the calculation of the exchange-correlation self-energy,  $\Sigma^{xc}$ , and Section 6.4 addresses the generation of the optimized Hamiltonian in QSGW, whose diagonalization returns eigenvectors, and eigenvalues. At the end of the iterative procedure, *i.e.*, when the variation of the electronic density between consecutive cycles reaches a threshold minimum, we obtain the quasiparticle states and energies,  $\{\psi_{m\mathbf{k}}^{\text{QP}}(\mathbf{r}), \epsilon_{m\mathbf{k}}^{\text{QP}}\}$ .

The **exciting** code implements the (L)APW+LO method (see Chapter 5) for the DFT calculations, treating all electrons on equal footing. As for excited-states calculations, the one-electron wavevectors in the LAPW basis,  $\psi_{m\mathbf{k}}$ , build a new basis set, presented in Sec. 5.5. The large number of basis functions and unoccupied states makes the QSGW method in an all-electron code very involved. Section 6.5 summarizes the parallelization scheme on the  $\mathbf{k}$ -grid, which speeds up calculations.

### 6.1 General Implementation Scheme

The QSGW implementation involves several operators in matrix form, classified in three groups:

- *First group*: Operators within the GS calculations building the IP Hamiltonian,  $H_{\mathbf{k}}^0$ , exposed in the two secular equations: Eq. 2.14 and Eq. 2.22. With the exemption of the Fock exchange operator, the numerical details of these calculations are explained in Ref. [58].
- *Second group*: Non-local operators from Hedin’s equations, implemented in **exciting** as presented in Ref. [64]. Because of their importance and deviations from the original publication, we revise them in the coming sections.
- *Third group*: The non-local, exchange-correlation potential  $v_{opt}^{xc}$  in Eq. 4.2. The matrix elements of this potential, diagonal and off-diagonal, are calculated in the mixed basis (MB), successively undergoing a basis transformation to return to LAPW basis representation.

The general implementation is sketched in Fig. 6.1. The first step in the implementation is to perform IP calculations, which involves operators in the first group, providing the initial vectors and energies. The following step is to construct the operators in the second and third group in matrix form for the first iteration. After having calculated the operators in the three groups for the first time, we replace the exchange-correlation potential in the IP scheme by the new potential  $v_{opt}^{xc}$ , defined in Eq. 4.2. Keeping this potential fixed, we repeat the GS calculations, solving the secular equations with the updated  $H_{\mathbf{k}}^0$ . This last step includes an iterative scheme, here called *inner cycle*. From the eigenvectors and eigenvalues produced in the inner cycle, we re-calculate the operators from the second and third groups in matrix form, and the steps above repeat. This will eventually

enable the transition  $\{\psi_{m\mathbf{k}}^{\text{IP}}(\mathbf{r}), \epsilon_{m\mathbf{k}}^{\text{IP}}\} \rightarrow \{\psi_{m\mathbf{k}}, \epsilon_{m\mathbf{k}}\} \rightarrow \{\psi_{m\mathbf{k}}^{\text{QP}}(\mathbf{r}), \epsilon_{m\mathbf{k}}^{\text{QP}}\}$ . The complete procedure is called the *outer cycle*<sup>1</sup>. Due to the lack of total energy calculations, we take the charge density as the only measure of self-consistency. Finally, if two consecutive iterations in the outer loop bring about a variation in charge density under a certain threshold, we conclude that the  $v_{opt}^{xc}$  is converged.

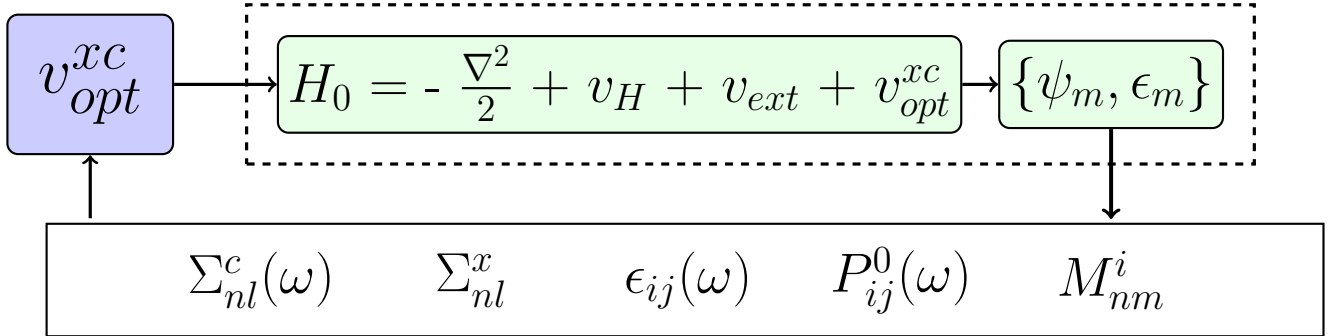


Figure 6.1: Flowchart of the QSGW implementation in `exciting`. The starting point is the independent particle Hamiltonian  $H_0$ . In the first iteration, which is not explicitly included in the figure, exchange-correlation potential and the resulting output  $\{\psi_{m\mathbf{k}}^{\text{IP}}(\mathbf{r}), \epsilon_{m\mathbf{k}}^{\text{IP}}\}$  correspond to an IP scheme. The optimized potential in the violet block, defined in Eq. 4.2, is the central quantity in the QSGW method.

Figure 6.1 presents the implementation of the QSGW in `exciting` in diagrammatic form, where the block outlined with the dashed borders represents the inner cycle. The light-green blocks represent the optimized independent-particle Hamiltonian and also its output, *i.e.* the eigenvectors and eigenvalues. The lower block displays the main quantities in the second group of operators. Every new potential  $v_{opt}^{xc}$  (violet block) is plugged into the Hamiltonian in the GS block. In the first iteration,  $v^{xc}$  corresponds to the exact exchange in the case of HFA, LDA in DFT, and PBE0 for the calculations using hybrid functionals.

For a consistent transition between the inner and outer cycles, operators in the three groups encounter the same calculation parameters. That is, (*i*) the  $\mathbf{k}$ -grid is shared by both cycles, unlike the implementation in Ref. [12], and it is the same as the  $\mathbf{q}$ -grid, (*ii*) the same unoccupied states enter the GS and GWA operators, (*iii*) all core electrons enter in the self-energy operator, in contrast to the all-electron implementation in Ref. [12], (*iv*) The operators from the three groups count with the same basis set parameters, *e.g.*,  $E_{l\alpha}$ ,  $\mathbf{R}_{MT}^\alpha \cdot |\mathbf{k} + \mathbf{G}|_{max}$ . The only exception is that the self-consistency criteria for charge density is much stricter in the inner than the outer cycle.

It is very important to mention that radial functions, and their integrals, are calculated in the first iteration, but otherwise remain fixed. Due to the non-locality of the new potential it is impossible to solve Eq. 5.3. This has been tested in our implementation, by including the updated density from the optimized  $H_{\mathbf{k}}^0$  into the local potential  $V_\alpha$ , but it returns unphysical results. To treat the non-linearity of the product of functions  $u_{l\alpha}(|\mathbf{r} - \mathbf{r}_\alpha|, \epsilon_{n\mathbf{k}})$ , as explained in Sec. 5.5, we discard eigenvalues  $\lambda_N$  of the overlap matrix above  $1 \cdot 10^{-4}$  Ha. In this implementation, we restrict the radial functions entering the MB by a cutoff parameter  $l_{max}^{MB} = 3$ , though without loss of accuracy.

## 6.2 GWA Equations in Matrix Form

In this section, we address the operators in the second group and write them in matrix form. Not every operator is written in the MB representation, as detailed below. For instance,  $G_0(\omega)$  never acquires an explicit matrix form, rather it is multiplied with the correlation part of the screened Coulomb interaction to give rise to a product of coefficients  $M_{nm}^i(\mathbf{k}, \mathbf{q})$ . From Eq. 3.45, the correlation

<sup>1</sup>Kotani, Schilfgaard and Faalev [12] refer to the inner cycle and outer cycle as “inner loop” and “large loop”, respectively.

contribution to the screened interaction is  $W^c(\omega) = W(\omega) - v$ . In matrix form,  $W^c(\omega)$  reads:

$$W_{ij}^c(\mathbf{q}, \omega) = \sum_{l,m} v_{i,l}^{\frac{1}{2}}(\mathbf{q}) [\epsilon_{l,m}^{-1}(\mathbf{q}, \omega) - \delta_{l,m}] v_{m,j}^{\frac{1}{2}}(\mathbf{q}), \quad (6.1)$$

and it depends on the bare Coulomb interaction  $v$  and the dielectric function  $\epsilon(\omega)$ , both examined in the next sections. As a previous step to arrive at the dielectric function, the polarizability is expanded in the MB:

$$P_{i,j}(\mathbf{q}, \omega) = \int_{\Omega} \int_{\Omega} [\chi_i^{\mathbf{q}}(\mathbf{r})]^* P_0(\mathbf{r}, \mathbf{r}'; \omega) \chi_j^{\mathbf{q}}(\mathbf{r}') d\mathbf{r} d\mathbf{r}'. \quad (6.2)$$

According to the random phase approximation (RPA), introduced in Sec. 3.4, we enter the Lehmann representation of  $G_0(\omega)$  in the basis  $\psi_{mk}$  (Eq. 3.14), thus  $P_0(\omega)$  becomes:

$$\begin{aligned} P_0(\mathbf{r}, \mathbf{r}'; \omega) &= -\frac{i}{2\pi} \int G_0(\mathbf{r}, \mathbf{r}'; \omega + \omega') G_0(\mathbf{r}', \mathbf{r}; \omega') e^{i\omega'\eta} d\omega' \\ &= -\frac{i}{2\pi} \int \sum_{n\mathbf{k}} \frac{\psi_{n\mathbf{k}}(\mathbf{r}) [\psi_{n\mathbf{k}}(\mathbf{r}')]^*}{\omega + \omega' - \epsilon_{n\mathbf{k}} - i\eta \operatorname{sgn}(\epsilon_F - \epsilon_{n\mathbf{k}})} \sum_{m\mathbf{k}-\mathbf{q}} \frac{\psi_{m\mathbf{k}-\mathbf{q}}(\mathbf{r}') [\psi_{m\mathbf{k}-\mathbf{q}}(\mathbf{r})]^*}{\omega' - \epsilon_{m\mathbf{k}-\mathbf{q}} - i\eta \operatorname{sgn}(\epsilon_F - \epsilon_{m\mathbf{k}-\mathbf{q}})} e^{i\omega'\eta} d\omega' \\ &= 2 \sum_{n\mathbf{k}} \sum_{m\mathbf{k}'} f_{n\mathbf{k}} (1 - f_{m\mathbf{k}'}) \psi_{n\mathbf{k}}(\mathbf{r}) \psi_{m\mathbf{k}'}^*(\mathbf{r}) \psi_{n\mathbf{k}}^*(\mathbf{r}') \psi_{m\mathbf{k}'}(\mathbf{r}') \cdot \left\{ \frac{1}{\omega - \epsilon_{m\mathbf{k}'} + \epsilon_{n\mathbf{k}} + i\eta} - \frac{1}{\omega + \epsilon_{m\mathbf{k}'} - \epsilon_{n\mathbf{k}} - i\eta} \right\}, \end{aligned} \quad (6.3)$$

where the integration over frequency is carried out analytically, with  $m$  being an occupied state (negative  $i\eta$ ) and  $n$  an unoccupied states (positive  $i\eta$ ). Here we have introduced the variable:  $\mathbf{k}' = \mathbf{k} - \mathbf{q}$ . The factor  $f_{n\mathbf{k}}$  is the occupation number of the state  $n\mathbf{k}$ , and the prefactor 2 makes up for the spin degeneracy. Inserting 6.3 in the MB expansion, and using the definition of  $M_{nm}^i(\mathbf{k}, \mathbf{q})$  in Eq. 5.7, the matrix form of  $P_0(\omega)$  reads:

$$P_{i,j}(\mathbf{q}; \omega) = \frac{1}{N_c} \sum_{\mathbf{k}} \sum_{nm}^{BZ} F_{nm}(\mathbf{k}, \mathbf{q}; \omega) M_{nm}^i(\mathbf{k}, \mathbf{q}) [M_{nm}^j(\mathbf{k}, \mathbf{q})]^*, \quad (6.4)$$

$$\text{with } F_{nm}(\mathbf{k}, \mathbf{q}; \omega) = 2 f_{n\mathbf{k}} (1 - f_{m\mathbf{k}-\mathbf{q}}) \left\{ \frac{1}{\omega - \epsilon_{m\mathbf{k}'} + \epsilon_{n\mathbf{k}} + i\eta} - \frac{1}{\omega + \epsilon_{m\mathbf{k}'} - \epsilon_{n\mathbf{k}} - i\eta} \right\}. \quad (6.5)$$

### 6.2.1 Coulomb Potential

The matrix form of the bare Coulomb interaction in the MB representation reads:

$$v_{ij}(\mathbf{q}) = N_c \int_{\Omega} \int_{\Omega} [\chi_i^{\mathbf{q}}(\mathbf{r})]^* \sum_{\mathbf{R}} v(\mathbf{r}, \mathbf{r}' - \mathbf{R}) e^{-i\mathbf{q}\cdot\mathbf{R}} \chi_j^{\mathbf{q}}(\mathbf{r}') d\mathbf{r} d\mathbf{r}'. \quad (6.6)$$

It has three distinctive contributions, depending on the region of space where  $\chi_i$  resides (displayed in the header of Table 6.1). The matrix elements of  $v_{ij}$  are calculated using two mixed-basis functions in a MT, two PWs, and a function in a MT and a PW.

For the case where  $\mathbf{r}$  and  $\mathbf{r}'$  lie inside the MT, we employ the Laplace expansion provided in Table 6.1, with  $r_<$  representing the smaller value among  $(\mathbf{r}, \mathbf{r}')$  and  $r_>$ , and the larger one. Also within the MT, we define  $\hat{\mathbf{e}}_{\mathbf{q}+\mathbf{G}}$  as the direction of the vector  $\mathbf{q} + \mathbf{G}$  in the overlap integral  $\mathcal{I}^{\text{MT}}$  (Table 6.1). The latter includes the Bessel function  $j_L$ . Otherwise, if at least one of the position

Table 6.1: Most important equations for the three blocks constituting the  $v_{ij}$  matrix.

	$\chi_i \in \text{MT}$	$\chi_i \in \text{MT}$ $\chi_j \in \text{IR}$	$\chi_i \in \text{IR}$
$\frac{1}{ \mathbf{r}-\mathbf{r}' } =$	$\sum_{l=0}^{\infty} \frac{4\pi}{2l+1} \frac{r_{<}^l}{r_{>}^{l+1}} \sum_{m=-l}^l Y_l^m(\hat{\mathbf{r}}) Y_l^{m*}(\hat{\mathbf{r}}')$ <b>Laplace Expansion</b>	$\frac{1}{V} \sum_{\mathbf{q}\mathbf{G}} e^{i(\mathbf{q}+\mathbf{G})\mathbf{r}} \frac{4\pi}{ \mathbf{q}+\mathbf{G} } e^{-i(\mathbf{q}+\mathbf{G})\mathbf{r}'}$ <b>Fourier Expansion</b>	
<b>Overlap</b>	$\mathcal{I}^{\text{MT}} = \frac{1}{\sqrt{\Omega}} \int_{\Omega} [\gamma_{\alpha NLM}^{\mathbf{q}}(\mathbf{r})]^* e^{i(\mathbf{q}+\mathbf{G})\mathbf{r}} d\mathbf{r} =$ $\frac{4\pi}{\sqrt{\Omega}} e^{i\mathbf{G}\cdot\mathbf{r}^{\alpha}} i^L Y_l^{m*}(\hat{\mathbf{e}}_{\mathbf{q}+\mathbf{G}}) \int_0^{\mathbf{R}_{\text{MT}}^{\alpha}} j_L( \mathbf{q}+\mathbf{G} ) \nu_{\alpha NL}(r) r^2 dr$		
<b>Integrals</b>	$\mathcal{I}^{\text{IR}} = \frac{1}{\sqrt{\Omega}} \int_{\Omega} [P_i^{\mathbf{q}}(\mathbf{r})]^* e^{i(\mathbf{q}+\mathbf{G})\mathbf{r}} d\mathbf{r} = \sum_{\mathbf{G}'} \tilde{\theta}_{\mathbf{G}-\mathbf{G}'} \tilde{S}_{\mathbf{G}'i}^*$		

vector lies in the IR, we make use of the Fourier expansion. The most simple case is where both basis functions belong to the IR. In this case, we insert the Fourier expansion in Eq. 6.6, ending up with a sum over  $\mathbf{G}$  containing the product of the second overlap integral in Table 6.1,  $\mathcal{I}^{\text{IR}}$ , its conjugate, and a factor  $4\pi/|\mathbf{q}+\mathbf{G}|$ , and it reads:

$$v_{ij}(\mathbf{q}) = \sum_{\mathbf{G}} \mathcal{I}^{\text{IR}} \frac{4\pi}{|\mathbf{q}+\mathbf{G}|^2} [\mathcal{I}^{\text{IR}}]^*. \quad (6.7)$$

Also straightforward is the case where one position vector belongs to the interstitial region and one to a MT; the mixed case. Here, inserting the Fourier transform in Eq. 6.6 returns the two types of overlap integrals shown in Table 6.1,<sup>2</sup>

$$v_{ij}(\mathbf{q}) = \frac{1}{\Omega} \sum_{\mathbf{q}'\mathbf{G}'} \frac{4\pi}{|\mathbf{q}'+\mathbf{G}'|^2} \sum_{\mathbf{R}} e^{-i(\mathbf{q}-\mathbf{q}')\cdot\mathbf{R}} \mathcal{I}^{\text{MT}} [\mathcal{I}^{\text{IR}}]^* \quad (6.8)$$

$$= \frac{4\pi}{\sqrt{\Omega}} \sum_{\mathbf{G}'} \frac{1}{|\mathbf{q}+\mathbf{G}'|^2} \tilde{S}_{\mathbf{G}'i}^* i^L Y_l^{m*}(\hat{\mathbf{e}}_{\mathbf{q}+\mathbf{G}'}) \int_0^{\mathbf{R}_{\text{MT}}^{\alpha}} j_L(|\mathbf{q}+\mathbf{G}'|) \nu_{\alpha NL}(r) r^2 dr. \quad (6.9)$$

For the mixed case,  $v_{ij} = v_{ji}^*$ . Finally, the most complex case is when both basis functions belong to a MT. We obtain the Coulomb matrix in the MT by replacing  $\chi_i$  with  $e^{i\mathbf{q}\cdot\mathbf{r}^{\alpha}} \nu_{\alpha NL}(r^{\alpha}) Y_{LM}(\hat{\mathbf{r}}^{\alpha})$  in Eq. 6.6. Here, we identify two possibilities: both position vectors,  $\mathbf{r} = \mathbf{r}_1$  and  $\mathbf{r}' = \mathbf{r}_2$ , belong to the same MT sphere or to different MT spheres. The former contains the case  $\mathbf{R} = 0$ , and in the latter case it is possible to separate the spatial integrals. To arrive at the final equations, the derivation employs identities and properties of spherical harmonics, all of which appear in Appendix C. To shorten the lengthy derivation of the equations, we refer to Appendix C in Ref. [65]. In the following, we merely give a basic recipe and lay out the equation for  $v_{ij}$  in the MT.

- Case  $\alpha \neq \alpha'$

We define three variables:  $\mathbf{R}_{\alpha\alpha'} = \mathbf{R} + \mathbf{r}_{\alpha} - \mathbf{r}_{\alpha'}$ ,  $\mathbf{r}_1^{\alpha} = \mathbf{r}_1 - \mathbf{r}^{\alpha}$ , and  $\mathbf{r}_2^{\alpha'} = \mathbf{r}_2 - \mathbf{r}^{\alpha'}$ . Here,  $r_{<} = \mathbf{r}_2^{\alpha'} - \mathbf{r}_1^{\alpha}$  and  $r_{>} = \mathbf{R}_{\alpha\alpha'}$ . For the case  $Y_l^m(\hat{r}_{<})$ , we use the addition theorem in Eq. C.5 to disentangle  $\mathbf{r}_2^{\alpha'}$  from  $\mathbf{r}_1^{\alpha}$  and be left with two separate integrals over the different MT spheres. As usual, integrals over the MT are separated in radial and angular parts. We define the lattice

<sup>2</sup>We exploit two identities to arrive to Eq. 6.9:  $e^{-i\mathbf{G}\cdot\mathbf{R}} = 1$  and  $\sum_{\mathbf{R}} e^{-i(\mathbf{q}-\mathbf{q}')\cdot\mathbf{R}} = N_c \delta_{\mathbf{q}\mathbf{q}'}$ .

structure constant  $\mathcal{S}_{ll'mm'}^{\alpha\alpha'}(\mathbf{q}) = (-1)^l \mathcal{C}_{ll'}^{mm'} \Xi$ , with coefficients  $\mathcal{C}$  defined in Eq. C.6. The lattice sum,  $\Xi$ , for this case is  $\sum_{\mathbf{R} \neq 0} e^{i\mathbf{q} \cdot \mathbf{R}} Y_l^m(\hat{R}_{\alpha\alpha'}) / R_{\alpha\alpha'}^{l+1}$ . Altogether, this leads to

$$v_{ij}(\mathbf{q}) = (-1)^M \mathcal{S}_{LL'MM'}^{\alpha\alpha'} \int_0^{\mathbf{R}_{MT}^\alpha} \nu_{\alpha NL}(r_1^\alpha) (r_1^\alpha)^2 (r_1^\alpha)^L dr_1^\alpha \int_0^{\mathbf{R}_{\alpha'}^{MT}} \nu_{\alpha' NL}(r_2^{\alpha'}) (r_2^{\alpha'})^2 (r_2^{\alpha'})^L dr_2^{\alpha'}. \quad (6.10)$$

- Case  $\alpha = \alpha'$

▷  $\mathbf{R} = 0$

\* The Coulomb matrix reads:

$$v_{ij}(\mathbf{q}) = \frac{4\pi}{2L+1} \int_0^{\mathbf{R}_{MT}^\alpha} \int_{\substack{r_1^\alpha < \\ r_2^\alpha >}}^{r_2^\alpha} \nu_{\alpha NL}(r_1^\alpha) (r_1^\alpha)^2 \nu_{\alpha NL}(r_2^\alpha) (r_2^\alpha)^2 dr_1^\alpha dr_2^\alpha. \quad (6.11)$$

▷  $\mathbf{R} \neq 0$

\* Same as for the case  $\alpha = \alpha'$ , but here we replace  $r_1^\alpha$  with  $r_1$ .

\* The lattice structure constant  $\mathcal{S}$  is the same here as in the previous case, but with  $\Xi = \sum_{\mathbf{R} \neq 0} e^{i\mathbf{q} \cdot \mathbf{R}} Y_l^m(\hat{R}) / R^{l+1}$ .

## Basis Transformation

The Coulomb interaction matrix in the MB has three distinctive blocks, according to the three cases discussed above. A diagonal form of the Coulomb matrix is desirable as it presents convenient mathematical properties: The matrix multiplication simplifies, and the treatment of the singularity at  $\mathbf{q} = 0$  for the dielectric function is limited to the first matrix element (head, abbreviated H) and the first column and row (wings, abbreviated W), while the rest (body, abbreviated B) holds no singularity. Unlike matrices in the MB representation, response-function matrices, and similar quantities, in a PW representation decomposes in head, wings and body. Seeking to recover this advantageous matrix form of response functions, the MB set has to undergo a basis transformation [66]. We start by building a diagonal form of the Coulomb interaction matrix. Since  $v_{ij}$  is a Hermitian operator, its matrix representation in the basis of its eigenvectors is diagonal. We summarize this basis transformation writing vectors in Dirac's notation:

$$|\chi_\mu^{\mathbf{q}}\rangle = \sum_i |\chi_i^{\mathbf{q}}\rangle U_{\mu i}^{\mathbf{q}}. \quad (6.12)$$

We build a transformation matrix by means of the eigenvectors of the Coulomb interaction matrix  $v_{ij}$  (Eq. 6.6). The  $i$ -th component of the  $\mu$ -th eigenvector of  $v_{ij}(\mathbf{q})$  is denoted by  $U_{\mu i}^{\mathbf{q}}$  in Eq. 6.12. In this new basis, the Coulomb matrix  $v_{ij}$  becomes diagonal, hence this basis is called "v-diagonal basis" [66]. We stress that this transformation does not imply an approximation; both Coulomb matrices are equivalent. Regarding the selection of physically significant eigenvectors, we consider eigenvectors whose corresponding eigenvalues fall under a threshold. Since eigenvalues disclose the probability of elastic scattering between two particles, the discarded values have a negligible contribution to the total interaction [66]. In this QSGW implementation, the chosen threshold of, 0.05 Ha, remains fixed, yet with every new iteration a different numbers of eigenvectors is discarded till, after some iterations, the dimension of the v-diagonal stands unchanged.

### 6.2.2 Dielectric Matrix

As previously defined in Eq. 3.43, the dielectric function in the GWA includes an integral over the product of the polarizability and the bare Coulomb interaction. The latter introduces a numerical challenge due to its singularity in reciprocal space as  $\mathbf{q}$  goes to zero. We go about this divergence carefully by symmetrizing the dielectric function. The symmetrization is carried out using the  $v$ -diagonal basis, where matrix elements in this representation carry the subscripts  $\mu\nu$ . The H, W, and B structure of the dielectric matrix follows from this representation of the Coulomb interaction. Conveniently, the divergence for the gamma point appears only in H and W (see previous section), and we treat it with the  $\mathbf{k} \cdot \mathbf{p}$ -perturbation technique [67], leading to:

$$H(0, \omega) = 1 - \frac{4\pi}{N_c \Omega} \sum_{\mathbf{k}} \left[ \sum_n \delta(\epsilon_F - \epsilon_{n\mathbf{k}}) \frac{(\mathbf{p}_{n\mathbf{k}} \cdot \hat{\mathbf{q}}_0)^2}{\omega^2} + \sum_{n \neq n'} F_{nn'}(\mathbf{k}, 0; \omega) \left| \frac{\mathbf{p}_{nn'\mathbf{k}} \cdot \hat{\mathbf{q}}_0}{\epsilon_{n'\mathbf{k}} - \epsilon_{n\mathbf{k}}} \right|^2 \right] \quad (6.13)$$

$$W_\mu(0, \omega) = - \left[ \sqrt{\frac{4\pi}{\Omega}} \right] \frac{1}{N_c} \sum_{\mathbf{k}} \sum_{n' \neq n} F_{nn'}(\mathbf{k}, 0; \omega) \frac{\mathbf{p}_{nn'\mathbf{k}} \cdot \hat{\mathbf{q}}_0}{\epsilon_{n'\mathbf{k}} - \epsilon_{n\mathbf{k}}} \tilde{M}_{nm}^\mu(\mathbf{k}, 0) \quad (6.14)$$

$$B_{\mu\nu}(0, \omega) = \delta_{\nu\mu} - \frac{1}{N_c} \sum_{\mathbf{k}} \sum_{n' n} F_{nn'}(\mathbf{k}, 0; \omega) \tilde{M}_{nm}^\mu(\mathbf{k}, 0) \left[ \tilde{M}_{nm}^\nu(\mathbf{k}, 0) \right]^* . \quad (6.15)$$

For all  $\mathbf{q}$  points, we use the matrix form in the  $v$ -diagonal representation, with the polarizability given in Eq. 6.4:

$$\epsilon_{ij}(\mathbf{q}, \omega) = \delta_{ij} - \sum_{lm} v_{il}^{\frac{1}{2}}(\mathbf{q}) P_{lm}(\mathbf{q}, \omega) v_{mj}^{\frac{1}{2}}(\mathbf{q}) \quad (6.16)$$

$$= \delta_{ij} - \frac{1}{N_c} \sum_{\mathbf{k}} \sum_{nm} \sum_{lm} F_{nm}(\mathbf{k}, \mathbf{q}; \omega) v_{il}^{\frac{1}{2}}(\mathbf{q}) M_{nm}^l(\mathbf{k}, \mathbf{q}) [M_{nm}^m(\mathbf{k}, \mathbf{q})]^* v_{mj}^{\frac{1}{2}}(\mathbf{q}) \quad (6.17)$$

$$= \delta_{ij} - \frac{1}{N_c} \sum_{\mathbf{k}} \sum_{nm} F_{nm}(\mathbf{k}, \mathbf{q}; \omega) \tilde{M}_{nm}^i(\mathbf{k}, \mathbf{q}) \left[ \tilde{M}_{nm}^j(\mathbf{k}, \mathbf{q}) \right]^* . \quad (6.18)$$

Equation 6.18 holds a contraction between the square root of the Coulomb matrix and the coefficients  $M_{nm}^i(\mathbf{k}, \mathbf{q})$ , in the  $v$ -diagonal basis representation:

$$\tilde{M}_{nm}^\nu(\mathbf{k}, \mathbf{q}) \equiv \sum_{\mu} \sqrt{v_{\nu\mu}(\mathbf{q})} M_{nm}^\mu(\mathbf{k}, \mathbf{q}) . \quad (6.19)$$

Using this form will prove highly efficient. The square-root of a symmetric matrix is given by the square root of its eigenvalues, which we already have from the diagonalization procedure.

## 6.3 Calculation of the Self-Energy

Finally, we arrive at the main object of interest: the self-energy. In this section, we explain the implementation of its two distinct contributions: the correlation self-energy —being the most demanding in terms of computational costs— and the exchange term. The latter is calculated as suggested by Betzinger and coworkers [68]. Both self-energies include a mixing of states, embodied in the off-diagonal terms of the respective matrices. Expectations values taken with respect to two different states, say  $n$  and  $l$ , make up the upper triangle of the self-energy matrix, the lower one is given exploiting hermiticity. In the following, these off-diagonal elements are denominated  $nl$ -terms.

### 6.3.1 Correlation Self-Energy

We compute  $\Sigma(\omega)$  according to Eq. 3.46, taking into account that we deal with the correlation term of the screened Coulomb potential,  $W^c(\omega)$ . Keeping track of the function's arguments, we replace  $G_0(\omega + \omega')$  with Eq. 3.14, followed by the insertion of the MB expansion of  $W^c(\omega)$ , and finally we employ the definition of  $M_{nm}^i(\mathbf{k}, \mathbf{q})$  in Eq. 5.7. Following these steps, the matrix elements of the correlation self-energy,  $\Sigma_{nl\mathbf{k}}^c(\omega) = \langle \psi_{n\mathbf{k}} | \Sigma(\omega) | \psi_{l\mathbf{k}} \rangle$  become:

$$\Sigma_{nl\mathbf{k}}^c(\omega) = \frac{i}{2\pi} \sum_{m\mathbf{k}'} \int \int \int \frac{[\psi_{n\mathbf{k}}(\mathbf{r})]^* \psi_{m\mathbf{k}'}(\mathbf{r}) W_0^c(\mathbf{r}', \mathbf{r}; \omega) \psi_{l\mathbf{k}}(\mathbf{r}') [\psi_{m\mathbf{k}'}(\mathbf{r}')]^*}{\omega + \omega' - \tilde{\epsilon}_{m\mathbf{k}'}} d\omega' d\mathbf{r} d\mathbf{r}' \quad (6.20)$$

$$= \frac{i}{N_c 2\pi} \sum_{m\mathbf{q}} \sum_{ij} \int \int \int \frac{\chi_i^{\mathbf{q}}(\mathbf{r}) [\psi_{n\mathbf{k}}(\mathbf{r})]^* \psi_{m\mathbf{k}'}(\mathbf{r}) W_{ij}^c(\mathbf{q}, \omega) \psi_{l\mathbf{k}}(\mathbf{r}') [\psi_{m\mathbf{k}'}(\mathbf{r}') \chi_j^{\mathbf{q}}(\mathbf{r}')]^*}{\omega + \omega' - \tilde{\epsilon}_{m\mathbf{k}'}} d\omega' d\mathbf{r} d\mathbf{r}' \quad (6.21)$$

$$= \frac{1}{N_c} \frac{i}{2\pi} \sum_{\mathbf{q}} \sum_m \sum_{i,j} \int_{-\infty}^{\infty} \frac{[M_{nm}^i(\mathbf{k}, \mathbf{q})]^* W_{i,j}^c(\mathbf{q}, \omega') M_{lm}^j(\mathbf{k}, \mathbf{q})}{\omega + \omega' - \tilde{\epsilon}_{m\mathbf{k}-\mathbf{q}}} d\omega'. \quad (6.22)$$

In the above equation,  $\mathbf{k}' = \mathbf{k} - \mathbf{q}$ , and the tilde above the  $\epsilon$  signals that the sign function is included, *i.e.*,  $\tilde{\epsilon}_{n\mathbf{k}} \equiv \epsilon_{n\mathbf{k}} + i\eta \text{sgn}(\epsilon_F - \epsilon_{n\mathbf{k}})$ . The product  $M^* W^c M$  is the most involved calculation in our implementation. We replace  $W_{i,j}^c(\mathbf{q}, \omega)$  with the right hand side of Eq. 6.1, making use of the  $v$ -diagonal basis and the contraction in Eq. 6.19, and obtain:

$$MWM = \sum_{\mu\nu} [\tilde{M}_{nm}^{\mu}(\mathbf{k}, \mathbf{q})]^* [\epsilon_{\mu\nu}^{-1}(\mathbf{q}, \omega') - \delta_{\mu\nu}] \tilde{M}_{lm}^{\nu}(\mathbf{k}, \mathbf{q}). \quad (6.23)$$

For the off-diagonal matrix elements, the product  $MWM$  is a three-dimensional tensor whose size depends on the number of frequencies, number of states (unoccupied, valence, and core states) and total number of  $nl$ -terms.

### Frequency Integration

Since the self-energy carries the product of two functions with singularities, its calculation poses a numerical challenge. The scientific community has developed several ways to go about this frequency-dependent calculation. The integral in Eq. 6.22 can be carried out directly on the real axis [69], or by means of contour deformation [63, 70]. Our method of choice is the analytic continuation [71]. The convolution integral over frequency in Eq. 6.22 has poles infinitesimally close to the real axes. To achieve accurate results requires a large number of frequencies. In **exciting**, we compute  $\Sigma^c(\omega)$  in reciprocal space and on the imaginary axis, and we change the integration variable to  $i\omega$  [72, 73]. This is justified since (i) it has been shown that if  $G$  is determined on the imaginary axis, it is thus also on the real axis [74], and (ii)  $W(w) = W(iw)$ . Given the inversion symmetry of  $W_{i,j}^c(\mathbf{q}, i\omega) = W_{i,j}^c(\mathbf{q}, -i\omega)$  on the imaginary axis, and using

$$\frac{i}{2\pi} \int_{-\infty}^{\infty} \frac{1}{\omega + i\omega' - \epsilon + i\eta \text{sgn}(\epsilon_F - \epsilon)} d(i\omega') = -\frac{1}{2\pi} \int_0^{\infty} \left[ \frac{1}{\omega + i\omega' - \epsilon} + \frac{1}{\omega - i\omega' - \epsilon} \right] d\omega',$$

we arrive at:

$$\Sigma_{nl\mathbf{k}}^c(i\omega) = \frac{1}{N_c} \frac{1}{\pi} \sum_{\mathbf{q}} \sum_m \sum_{i,j} [M_{nm}^i(\mathbf{k}, \mathbf{q})]^* \int_0^{\infty} \frac{(\epsilon_{m,\mathbf{k}-\mathbf{q}} - i\omega) W_{i,j}^c(\mathbf{q}, i\omega')}{(\epsilon_{m,\mathbf{k}-\mathbf{q}} - i\omega)^2 + \omega'^2} d\omega' M_{lm}^j(\mathbf{k}, \mathbf{q}). \quad (6.24)$$

It is clear that in the case of  $\omega = \omega'$  and  $\epsilon_{m,\mathbf{k}-q} = 0$ , the integrand above becomes singular. For small values of  $\epsilon_m$ , we avoid direct numerical integration. To achieve a smooth integrand in Eq. 6.24, we add and subtract the following term [75]:

$$\frac{1}{2\pi} \int_0^\infty \frac{(\epsilon_{m,\mathbf{k}-q} - i\omega)W_{i,j}^c(\mathbf{q}, i\omega)}{(\epsilon_{m,\mathbf{k}-q} - i\omega)^2 + \omega'^2} d\omega' = \frac{1}{2} \text{sgn}(\epsilon_{m,\mathbf{k}-q})W_{i,j}^c(\mathbf{q}, i\omega). \quad (6.25)$$

Finally, we arrive at the correlation self-energy:

$$\begin{aligned} \Sigma_{nl\mathbf{k}}^c(i\omega) = \frac{1}{N_c} \frac{1}{2\pi} \sum_{\mathbf{q}}^{BZ} \sum_m \sum_{i,j} [M_{nm}^i(\mathbf{k}, \mathbf{q})]^* \int_0^\infty \frac{2(\epsilon_{m,\mathbf{k}-q} - i\omega)[W_{i,j}^c(\mathbf{q}, i\omega') - W_{i,j}^c(\mathbf{q}, i\omega)]}{(i\omega - \epsilon_{m,\mathbf{k}-q})^2 + \omega'^2} d\omega' M_{lm}^j(\mathbf{k}, \mathbf{q}) \\ + \frac{1}{2} \text{sgn}(\epsilon_{m,\mathbf{k}-q})W_{i,j}^c(\mathbf{q}, i\omega). \end{aligned} \quad (6.26)$$

To solve the semi-infinite integral of the form  $\mathbb{I} = \int_0^\infty f(\omega')d\omega'$  we use the double Gaussian quadrature. We split the integration interval into two subintervals, *i.e.*, from 0 to  $\omega_0$  and from  $\omega_0$  to  $\infty$ . The integration depends on the choice of  $\omega_0$ , as shown in Ref. [64]. Therefore, we evaluate the parameter  $\omega_0$  at different values and choose the most suitable for the number of frequency points entering the numerical integration. Each of the subintervals in the integral,

$$\mathbb{I} = \mathbb{I}_1 + \mathbb{I}_2 = \frac{\omega_0}{2} \int_{-1}^1 f\left[\left(u+1\right)\frac{\omega_0}{2}\right] du + 2\omega_0 \int_{-1}^1 f\left[\frac{2\omega_0}{u+1}\right] (u+1)^{-2} du, \quad (6.27)$$

can be computed using the standard Gaussian quadrature [76]. For the first interval  $\mathbb{I}_1$ , we perform a change of variables:  $u = 2\omega'/\omega_0 - 1$  and  $d\omega' = \omega_0/2 du$ . For the second interval  $\mathbb{I}_2$ , the change of variables is  $u = 2\omega_0/\omega' - 1$  and  $d\omega' = -2\omega_0/(u+1)^2 du$ . The correlation self-energy is then mapped onto the real axis by means of Pade's Approximants, as described in Appendix E.

### 6.3.2 Exchange Self-Energy

Analogous to the correlation part, we take the expectation value of the exchange self-energy with respect to two one-electron states,  $n$  and  $l$ . We replace  $G_0(\omega)$  with Eq. 3.14 and use the expansion of  $v$  in MB functions, finally employing the contracted form of  $M_{nm}^i(\mathbf{k}, \mathbf{q})$  in the  $v$ -diagonal basis:<sup>3</sup>

$$\Sigma_{nl\mathbf{k}}^x = \frac{i}{2\pi} \sum_{m\mathbf{k}'} \int \int \int \frac{[\psi_{n\mathbf{k}}(\mathbf{r})]^* \psi_{m\mathbf{k}'}(\mathbf{r}) v(\mathbf{r}', \mathbf{r}) \psi_{l\mathbf{k}}(\mathbf{r}') [\psi_{m\mathbf{k}'}(\mathbf{r}')]^*}{\omega + \omega' - \tilde{\epsilon}_{m\mathbf{k}'}} e^{i\omega'\eta} d\omega' d\mathbf{r} d\mathbf{r}' \quad (6.28)$$

$$= - \sum_{m\mathbf{k}'} \int \int f_{m\mathbf{k}'} [\psi_{n\mathbf{k}}(\mathbf{r})]^* \psi_{m\mathbf{k}'}(\mathbf{r}) v(\mathbf{r}', \mathbf{r}) \psi_{l\mathbf{k}}(\mathbf{r}') [\psi_{m\mathbf{k}'}(\mathbf{r}')]^* d\mathbf{r} d\mathbf{r}' \quad (6.29)$$

$$= - \frac{1}{N_c} \sum_{\mathbf{q}}^{BZ} \sum_{\nu} \sum_m^{occ} [\tilde{M}_{nm}^{\nu}(\mathbf{k}, \mathbf{q})]^* \tilde{M}_{lm}^{\nu}(\mathbf{k}, \mathbf{q}). \quad (6.30)$$

The occupation number,  $f$ , for state  $m\mathbf{k}'$  is replaced by one since all states  $m$  are occupied. From Eq. 6.29, we see that the exchange self-energy is the expectation value of the Fock operator.

<sup>3</sup>The integral over frequency is only non-zero for occupied states,

$$\int \frac{e^{i\omega'\eta}}{\omega' - \epsilon_{m\mathbf{k}'} + i\eta \text{sgn}(\epsilon_F - \epsilon_{m\mathbf{k}'})} d\omega' = 2\pi\theta(\epsilon_F - \epsilon_{m\mathbf{k}'}).$$

### 6.3.3 Singularities of the Self-Energy

The self-energy has poles coming from  $G_0$ , but also singularities from the Coulomb potential in the limit  $\mathbf{q} \rightarrow 0$ . Here we describe the treatment of the first term, *i.e.*,  $\mathbf{q} = 0$ , within the sum in the self-energy and define the singularity terms. **exciting** makes use of the technique proposed by Masidda and coworkers, where auxiliary functions  $F_1$  and  $F_2$  are added to  $\Sigma^{xc}$  when  $\mathbf{q} = 0$  [77]. These auxiliary functions have singularities similar to the Coulomb interaction.

$$F_1(\mathbf{q} \rightarrow 0) = \frac{1}{q} + \sum_{\mathbf{G} \neq 0} \frac{e^{-\beta|\mathbf{q}+\mathbf{G}|^2}}{|\mathbf{q}+\mathbf{G}|} \quad , \quad F_2(\mathbf{q} \rightarrow 0) = \frac{1}{q^2} + \sum_{\mathbf{G} \neq 0} \frac{e^{-\beta|\mathbf{q}+\mathbf{G}|^2}}{|\mathbf{q}+\mathbf{G}|^2}, \quad (6.31)$$

where the parameter  $\beta$  in **exciting** (and also in other codes) is  $\beta = (\Omega/6\pi^2)^{1/3}$ . With this two auxiliary functions, we calculate the prefactors

$$C_{s1} = \frac{\Omega}{(2\pi)^2\beta} - \frac{1}{N_c} \sum_{\mathbf{q}} \frac{e^{-\beta|\mathbf{q}+\mathbf{G}|^2}}{|\mathbf{q}+\mathbf{G}|} \quad , \quad C_{s2} = \frac{\Omega}{(2\pi)^2} \sqrt{\frac{\pi}{\beta}} - \frac{1}{N_c} \sum_{\mathbf{q}} \frac{e^{-\beta|\mathbf{q}+\mathbf{G}|^2}}{|\mathbf{q}+\mathbf{G}|^2} \quad (6.32)$$

which, multiplied by the singularity terms, may be added to the self-energy at  $\mathbf{q} = 0$ . Both contributions to the self-energy, in Eq. 6.26 and in Eq. 6.30, contain a sum over  $\mathbf{q}$ -points. Following the treatment exposed in detail in Ref. [64], we separate the first term in the sum over  $\mathbf{q}$ -points from the rest. For this term, in the exchange self-energy  $\Sigma^x$ , we add one term:

$$\frac{4\pi}{\Omega} C_{s2}, \quad (6.33)$$

and two to  $\Sigma^c$ :

$$C_{s2} \frac{4\pi}{\Omega} (H(0, \omega))^{-1} \quad (6.34)$$

$$C_{s1} \sqrt{\frac{4\pi}{\Omega}} \sum_{\mu \neq 0} \left[ (W_\mu(0, \omega))^{-1} \tilde{M}_{nn}^\mu(\mathbf{k}, 0) + (W_\mu(0, \omega))^{-1} [\tilde{M}_{nn}^\mu(\mathbf{k}, 0)]^* \right], \quad (6.35)$$

where we include the inverse of the head and wings, defined in Eq. 6.13 and Eq. 6.14, respectively.

## 6.4 Optimized Hamiltonian in QSGW

Once we arrive at the matrix form of the correlation self-energy in Eq. 6.26 and the exchange self-energy in Eq. 6.30, we sum these matrices, forcing hermiticity as an approximation [12]. This final matrix cannot be inserted into the Hamiltonian as such, because the matrix form of the Hamiltonian is represented in the LAPW basis,  $\{\phi_{\mathbf{k}+\mathbf{G}}\}$ , as:

$$H_{\mathbf{G}\mathbf{G}'}^{\mathbf{k}} = \langle \phi_{\mathbf{k}+\mathbf{G}} | -\frac{1}{2} \nabla_{\mathbf{r}}^2 + v(\mathbf{r}) + v_{\text{H}}(\mathbf{r}) + v_{xc}(\mathbf{r}) | \phi_{\mathbf{k}+\mathbf{G}'} \rangle, \quad (6.36)$$

where the one-body operators are described in Chapter 2, while  $v_{xc}^{opt}$  is not represented in the LAPW basis. In **exciting**, the secular equation for the Hamiltonian matrix in the LAPW representation is

$$\mathbf{H}^{\mathbf{k}} \mathbf{C}^{\mathbf{k}} = \mathbf{E}^{\mathbf{k}} \mathbf{S}^{\mathbf{k}} \mathbf{C}^{\mathbf{k}}, \quad (6.37)$$

with the overlap matrix

$$S_{\mathbf{G}\mathbf{G}'}^{\mathbf{k}} = \langle \phi_{\mathbf{k}+\mathbf{G}} | \phi_{\mathbf{k}+\mathbf{G}'} \rangle, \quad (6.38)$$

where  $\mathbf{C}$  is the matrix formed by the expansion coefficients in Eq. 5.1, and  $\mathbf{E}$  is the matrix holding the  $n$  eigenvalues for a specific  $\mathbf{k}$ -point [58].

To replace  $v_{xc}$  in Eq. 6.36 with  $v_{opt}^{xc}$  (in the following we drop *opt* and *xc*, being understood we deal with this specific potential) and solve Eq. 6.37, we need to perform a basis transformation from the basis set  $\{\psi_{n\mathbf{k}}\}$  to  $\{\phi_{\mathbf{k}+\mathbf{G}}\}$ , to obtain the matrix elements  $v_{\mathbf{G}\mathbf{G}'}^{\mathbf{k}}$ . To change the basis of a matrix representation, we need a matrix  $\mathbf{U}$  such that  $v_{\mathbf{G}\mathbf{G}'}^{\mathbf{k}} = \mathbf{U}^{-1} v_{nl} \mathbf{U}$ . In our case,  $\mathbf{U}$  is the product of the overlap matrix and the vector of the expansion coefficients, detailed in Ref. [68]:

$$v_{\mathbf{G}\mathbf{G}'}^{\mathbf{k}} = \sum_{nl} \left[ \sum_{\mathbf{G}''} \left( S_{\mathbf{G}\mathbf{G}''}^{\mathbf{k}} \right)^* C_{n\mathbf{G}''}^{\mathbf{k}} \right] v_{nl}^{\mathbf{k}} \left[ \sum_{\mathbf{G}''} \left( C_{l\mathbf{G}''}^{\mathbf{k}} \right)^* S_{\mathbf{G}''\mathbf{G}'}^{\mathbf{k}} \right]. \quad (6.39)$$

## 6.5 Parallelization

The **exciting** code uses the *message passing interface* (MPI) parallelization. Every MPI process belongs to a specific *rank*, which can host one or many MPI processes. Following the categories in Sec. 6.1, the operators in the first group are  $\mathbf{k}$ -dependent, making the parallelization over  $\mathbf{k}$ -points the most suitable scheme. We distribute the numerical tasks among several ranks, depending on memory and computational-power requirements. The code assigns a specific  $\mathbf{k}$ -point to one rank, and it will solve the tasks related to that particular point, including the diagonalization of the Hamiltonian. At the end of the inner cycle, one rank collects the information of all MPI processes.

This scheme is also valid for the second group of operators. However, as expressed in the matrix form of the operators, there is a sum over  $\mathbf{q}$ -points, and we distribute the MPI tasks according to the  $\mathbf{q}$ -grid. At the end of the loop, the code gathers the contributions of each  $\mathbf{q}$ -point under the corresponding  $\mathbf{k}$ -point.

The analytic continuation is carried out *after* the loop over  $\mathbf{k}$ -points. Specifically for the QSGW implementation, the analytic continuation of the correlation self-energy is parallelized. The need to do so clearly stems from the large number of off-diagonal matrix elements. The QSGW requires the evaluation of every  $\Sigma_{nl\mathbf{k}}$  term at energies  $\epsilon_{n\mathbf{k}}$  and  $\epsilon_{l\mathbf{k}}$ , as shown in Eq. 4.2. Therefore, we parallelize this portion of the code again over  $\mathbf{k}$ -points. Likewise, the basis transformation of the optimized potential matrix (Sec. 6.4) is also parallelized over  $\mathbf{k}$ -points.

## 6.6 Computational Requirements

In **exciting**, the  $nl$ -terms of the self-energy pose the greatest computational burden in QSGW calculations. For any material, the QSGW calculation for  $N$  empty and  $M$  occupied (including core) states, demands computing  $[(N + M + 1)^2 - (N + M + 1)] / 2$  off-diagonal terms in the self-energy matrix. These terms are calculated for each MPI process, *i.e.*, each  $\mathbf{k}$ -point, separately, and finally gathered in one matrix. Equation 6.24 shows the product of three matrices  $MWM$ , which in turn is a three dimensional complex matrix of size (number of  $nl$ -terms  $\times$   $(N+M)$   $\times$  number of frequencies). Since the columns in the matrix  $v_{\mu\nu}$  do not include all eigenvectors of  $v_{ij}$ , the dimensions in the  $v$ -diagonal basis can be lowered by as many eigenvalues fall under the threshold. This translates in a smaller matrix size of  $\tilde{M}_{nm}^{\nu}(\mathbf{k}, \mathbf{q})$ , as defined in Eq. 6.19.

Time-wise, the *central processing unit* (CPU) works on the tasks uninterruptedly till it reaches the point after which the calculation resumes from the last performed iteration, if not converged. Taking into account all of the iterations till convergence and the number of CPUs, we estimate the

run time for boron nitride, the most demanding material in our sample set. The calculation for BN employs a large basis set, which, using 128 CPUs, requires ten iterations to reach convergence. For this calculation, we distributed the 64 MPI processes evenly on 8 nodes, each with 16 logical and 16 physical cores and 128 GB memory space.

Table 6.2: Computational requirements for QSGW calculations in the case of BN. For the matrix elements in the correlation self-energy, saved as complex numbers—they count as double floating points—each entry takes up 16 bytes of memory.

Total nr. states	Total nr. <i>nl</i> -terms	Total nr. MB functions	Memory [GB] for <i>MWM</i> 64 <b>k</b> -points	CPU time [hours] per iteration
357	53956	1069	587.8	8832

Each QSGW calculation demands a different workload, depending on the material and its set-up. In this project, we assess the task distribution and memory allocation demands for each individual material according to the resources available. While Table 6.2 displays numbers for BN, the workload distribution and CPU time for different materials may look very different.



## Chapter 7

# Electronic Structure of Selected Materials by Means of QSGW

The implementation of the QSGW method in `exciting` aims at acquiring information from all-electron calculations on electronic structures of different types of materials. From the analysis of our results, a large share of the information derives from bandstructures and densities of states, discussed in Sec. 7.3. From a method-development perspective, a closer look at individual aspects of the QSGW method uncovers additional particularities of the material. To exploit this aspect, Section 7.4 deals with contributions from the off-diagonal terms of the self-energy to the overall bandstructure by comparing QSGW calculations with the full self-energy matrix and with the diagonal terms only. To underline the inter-band interactions behind the off-diagonal matrix elements, we call them *nl-terms*, where  $n$  and  $l$  are two band indexes. The *nl-terms* are absent in the widely used  $G_0W_0$ , and their role in QSGW is also discussed in literature, with varying opinions [50, 78, 79]. The off-diagonal contributions also affect the curvature of the bands, and hence the electron effective masses, presented in Sec. 7.4.

Another interesting aspect in QSGW is the starting-point (in)dependence, reviewed in Sec. 7.5, which we study by analyzing QSGW results from different initial mean-field potentials. In this account, we compare results among different materials and also against  $G_0W_0$  results. To complete this investigation on electronic structure by means of QSGW, we take into consideration the initial and converged wavefunctions (WFs). In Sec. 7.6, we study the density re-distribution taking place when calculations performed using the Kohn-Sham (KS) scheme are performed using the QSGW method instead. The electron density differences in space expose the impact of the many-body iterative scheme on the allocation of the charge given by KS, and how far or close is the initial result to QSGW. In the final section, we deal with the WFs, mainly the differences between electronic states calculated using the KS scheme and the QSGW method. As an introduction, the following sections present the choice of materials and the computational details for the QSGW calculations.

### 7.1 Materials

To cover different features of electronic structures, our sample set consists of nine materials, ranging from small bandgap semiconductors to insulators, and heterogeneous and homogeneous compounds. These are the semiconductors SiC, Si, BN, C (diamond), GaAs, the non-magnetic oxides MgO and CaO, the salt LiF, and the noble element Ar in bulk form. In Table 7.1, the computational parameters are displayed for each material with their corresponding lattice parameters.

Table 7.1: Selected materials together with their structure types and lattice parameters,  $a$ , and the corresponding input parameters that enter the calculations. Here we use the abbreviation  $RGK$  for  $R_{\text{MT}}|\mathbf{G} + \mathbf{k}|_{\text{max}}$ .

	Structure type	$a(\text{\AA})$	$RGK$	$R_{\text{MT}}$ (bohr)	Nr. of empty states	Nr. of $nl$ -terms	MB size at $\Gamma$
SiC	zinc blende	4.340 [80]	11	1.6	350	46360	1460
Si	diamond	5.431 [81]	10	2.1	300	48828	1373
BN	zinc blende	3.615 [82]	11	1.4	350	53956	1315
MgO	rocksalt	4.211 [83]	11	1.6	350	54946	1443
CaO	diamond	4.810 [84]	11	Ca 2.0 O 1.8	350	43956	1383
LiF	rocksalt	4.010 [80]	11	1.6	400	45753	1275
Ar	fcc	5.260 [82]	11	2.75	350	60378	741
C	diamond	3.567 [85]	10	1.4	300	46360	1143
GaAs	zinc blende	5.653 [86]	11	2.2	350	42195	1779

## 7.2 Computational Details

For this project, the selected semiconductors and insulators are taken in bulk form, having all cubic structure. The lattice constants  $a$ , listed in Table 7.1, are taken from experiment. Calculations based on many-body perturbation theory, *i.e.*,  $G_0W_0$  and QSGW, were performed on a  $4 \times 4 \times 4$   $\mathbf{k}$ -point grid ( $\mathbf{k}$ -grid), whereas independent particle (IP) calculations employed a  $6 \times 6 \times 6$   $\mathbf{k}$ -grid. Whenever a MBPT method is applied on top of eigenvalues and eigenvectors from an IP approach, we denote it  $MBPT@IP$ . In general, the underlying IP calculations employ the LDA potential, dropping the label  $@LDA$  unless the starting-point dependence is probed.

The basis functions in the (L)APW+lo method depend on the muffin tin (MT) radius,  $R_{\text{MT}}$ , which —apart from calcium oxide<sup>1</sup>— is taken to be the same for both elements in binary compounds. The number of planewaves is determined by  $R_{\text{MT}}|\mathbf{G} + \mathbf{k}|_{\text{max}}$ , abbreviated as  $RGK$  in Table 7.1, which we chose to be 10 or 11, values that guarantee high numerical precision. The radial functions depend on the maximum azimuthal number,  $l_{\text{max}}^{\text{APW}}$ , here set to 12 for all materials. Apart from these parameters, those specific to the mixed basis (MB), detailed in Sec. 6.1, also restrict the number of radial functions. The final size of the MB is given in Table 7.1 for the  $\Gamma$  point.

For the integration over frequency, we take 32 frequencies into account for the calculations of the self-energy, and  $\omega_0 = 1$  Ha is chosen in the double Gaussian quadrature algorithm (see Eq. 6.27). For the  $nl$ -terms in the self-energy matrix, we choose an energy threshold,  $\epsilon_{nl}^{\text{max}}$ ; only states  $n$  and  $l$  with energies below  $\epsilon_{nl}^{\text{max}}$  build the upper triangle of the self-energy.  $\epsilon_{nl}^{\text{max}}$  is chosen so that the  $nl$ -terms always include the first 300 states. Based on our tests, disregarded higher-energy states have no effect on the final result. The second-last column in Table 7.1 displays the final number of  $nl$ -terms.

<sup>1</sup>For the calcium atom, the description of the nodal structure of  $4p$ -orbitals required either a large amount of PWs or a large  $R_{\text{MT}}$ , for which we chose the latter option. For the oxygen atom, a smaller radius sufficed.

In general, for QSGW calculations, the bandgap energy and the energies at the valence band maximum (VBM) and conduction band minimum (CBM) converge after the same number of iterations, as shown in Fig. 7.1. The required number of iterations to reach convergence in QSGW varies considerably among materials; bulk argon takes only five iterations to converge, while BN requires eleven and Si nine.

To test the convergence with respect to the number of unoccupied states, we calculated argon with 300, 350, 360, and 400 empty states. The calculation using 300 empty states returns  $E_g = 15.30$  eV, while all the other calculations give  $E_g = 15.33$ . Similarly, for LiF we performed calculations using 300, 350, 400, and 450 empty states. The calculation employing 300 unoccupied states returns  $E_g = 17.03$ . Among the other numbers of empty states for LiF, the bandgap energy changes in very small numbers till it reaches  $E_g = 17.10$  for the two largest numbers of empty states.

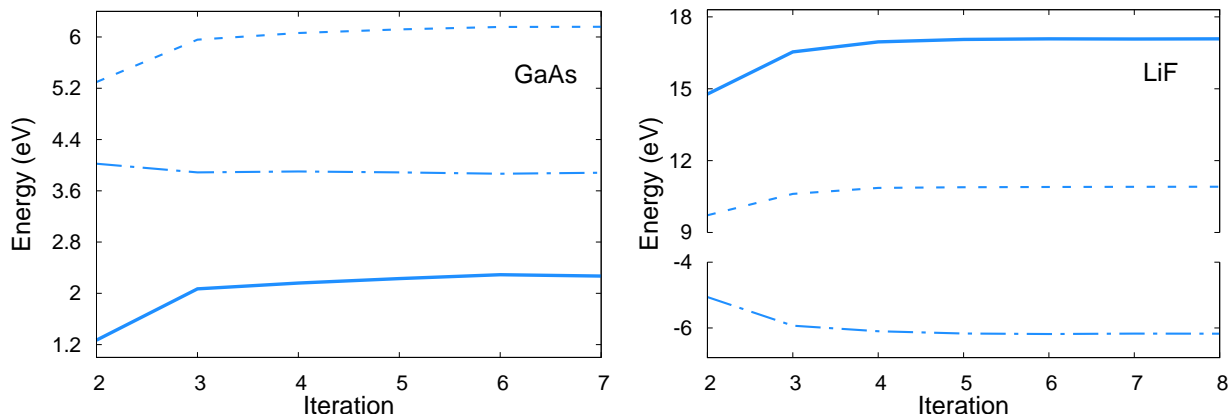


Figure 7.1: Convergence of the bandgap energy (solid line), and the band energies of the VBM (dotted dashed line) and of the CBM (dashed line) for the QSGW calculations. The first iteration corresponds to the initial KS calculation and is not shown in the plots.

### 7.2.1 Set-up of Local Orbitals

For all calculations —IP and MBPT schemes— a number of local orbitals (LO) adhere to the (L)APW basis set. Based on previous calculations with **exciting**, eigenvalues corrected by the  $G_0W_0$  scheme show convergence with 3 meV precision with respect to LOs when six  $l$ -channels are included, therefore we set  $l_{max}^{LO} = 6$  for all materials [87]. Since the radial functions are fixed in QSGW, the choice of linearization energies,  $E_{l\alpha}$ , requires special care. Through the optimization process indicated in Sec. 5.2, following the Wigner-Seitz rules, we search for  $E_{l\alpha}$  and tailor the (L)APW+LO basis set for each atom with a specific  $R_{MT}$ .

As an example, Table 7.3 presents the set-up of LOs for the first three  $l$ -channels for GaAs. Adjusting the notation we use in Chapter 5, we write  $r = |\mathbf{r} - \mathbf{r}_\alpha|$  and leave out the subscript  $\alpha$ , adding instead the band index  $n$  to the linearization energy,  $E_{nl}$ . Otherwise the formulation in Table 7.3 follows Chapter 5. Besides the search process *prior* to the calculations, the linearization energies carrying a  $t$  —it stands for *search set to true*— undergo an extra optimization in the first QSGW iteration. For  $l^{LO} = 3 \dots 6$  in GaAs, local orbitals have the same linear combination as in  $l^{LO} = 0$  (Table 7.3), though the number of LOs for the two highest  $l^{LO}$ -values reduces to *two* per channel. In average, the number of LOs for each material is roughly half of those employed in the GaAs case, as displayed in Table 7.2.

Table 7.2: Total number of local orbitals per unit cell for each material considered in this work.

	SiC	Si	BN	GaAs	MgO	CaO	LiF	Ar	C
Nr. of LOs	155	164	138	312	168	136	140	127	146

Table 7.3: Configuration of LOs in GaAs for the first three  $l$ -channels. For each atom, in the left column there is the set-up of the LOs and at the right the linearization energy value  $E_{nl}$  (Ha) for state  $n$  and angular momentum  $l$ .

$l$	Ga		As	
$s$	$a_\mu u_0(r, E_{10}) + b_\mu \dot{u}_0(r, E_{10})$	$E_{10} = 0.1500^t$	$a_\mu u_0(r, E_{10}) + b_\mu \dot{u}_0(r, E_{10})$	$E_{10} = -0.3000^t$
	$a_\mu u_0(r, E_{20}) + b_\mu \dot{u}_0(r, E_{20})$	$E_{20} = 5.1427$	$a_\mu u_0(r, E_{20}) + b_\mu \dot{u}_0(r, E_{20})$	$E_{20} = 4.4889$
	$a_\mu u_0(r, E_{30}) + b_\mu \dot{u}_0(r, E_{30})$	$E_{30} = 12.8164$	$a_\mu u_0(r, E_{30}) + b_\mu \dot{u}_0(r, E_{30})$	$E_{30} = 11.9675$
$p$	$a_\mu u_1(r, E_{11}) + b_\mu \dot{u}_1(r, E_{11})$	$E_{11} = 0.1500^t$	$a_\mu u_1(r, E_{11}) + b_\mu \dot{u}_1(r, E_{11})$	$E_{11} = 0.1500$
	$a_\mu u_1(r, E_{21}) + b_\mu \dot{u}_1(r, E_{21})$	$E_{21} = 5.7991$	$a_\mu u_1(r, E_{21}) + b_\mu \dot{u}_1(r, E_{21})$	$E_{21} = 5.1086$
	$a_\mu u_1(r, E_{31}) + b_\mu \dot{u}_1(r, E_{31})$	$E_{31} = 13.3397$	$a_\mu u_1(r, E_{31}) + b_\mu \dot{u}_1(r, E_{31})$	$E_{31} = 12.5606$
$p$	$a_\mu u_2(r, E_{12}) + b_\mu \dot{u}_2(r, E_{12})$	$E_{12} = -0.4000^t$	$a_\mu u_2(r, E_{12}) + b_\mu \dot{u}_2(r, E_{12})$	$E_{12} = -1.1500$
	$a_\mu u_2(r, E_{22}) + b_\mu \dot{u}_2(r, E_{22})$	$E_{22} = 2.0859$	$a_\mu u_2(r, E_{12}) + a'_\mu u_2(r, E_{22})$	$E_{22} = 0.1500$
	$a_\mu u_2(r, E_{31}) + b_\mu \dot{u}_2(r, E_{31})$	$E_{32} = 6.7683$	$a_\mu u_2(r, E_{22}) + b_\mu \dot{u}_2(r, E_{22})$	

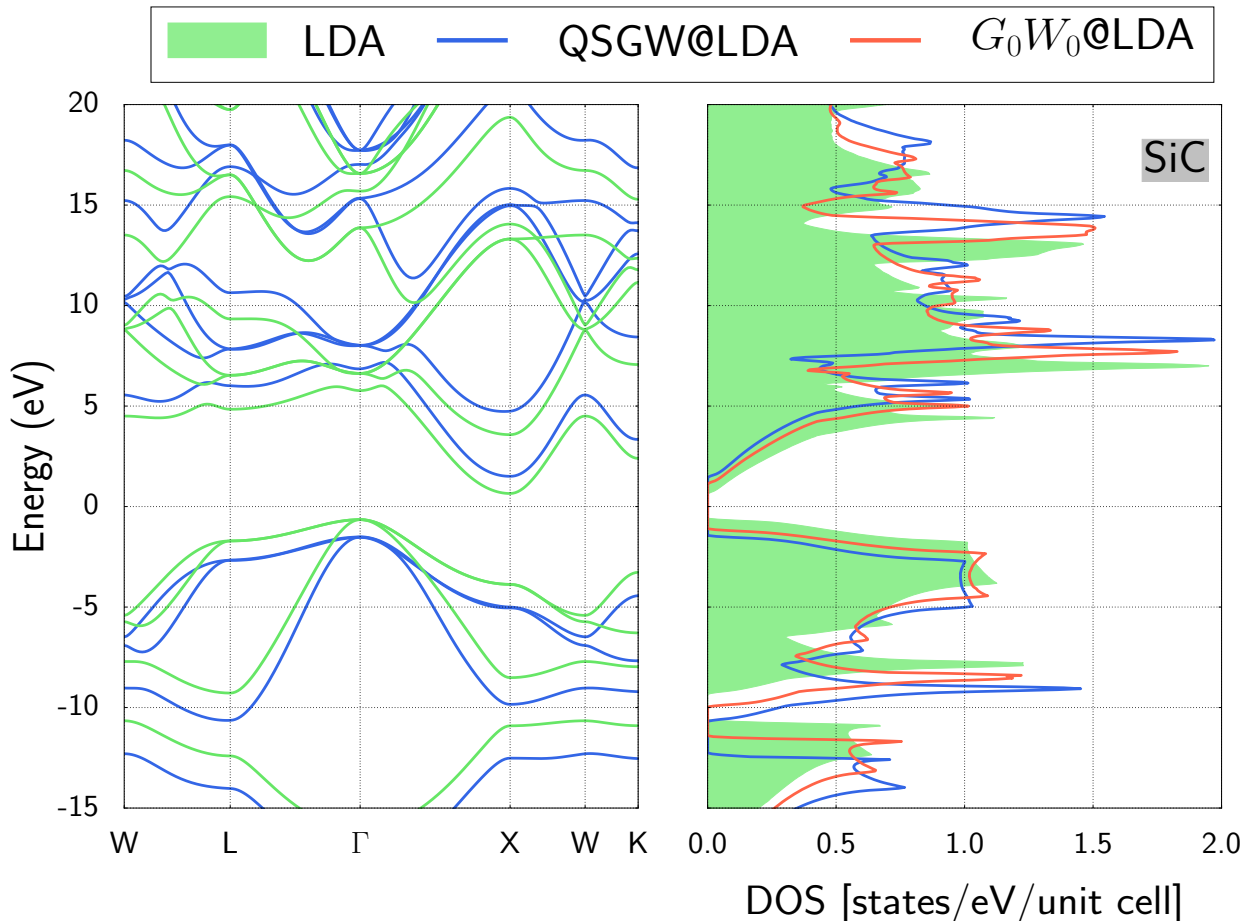
### 7.3 Bandstructures and Densities of States

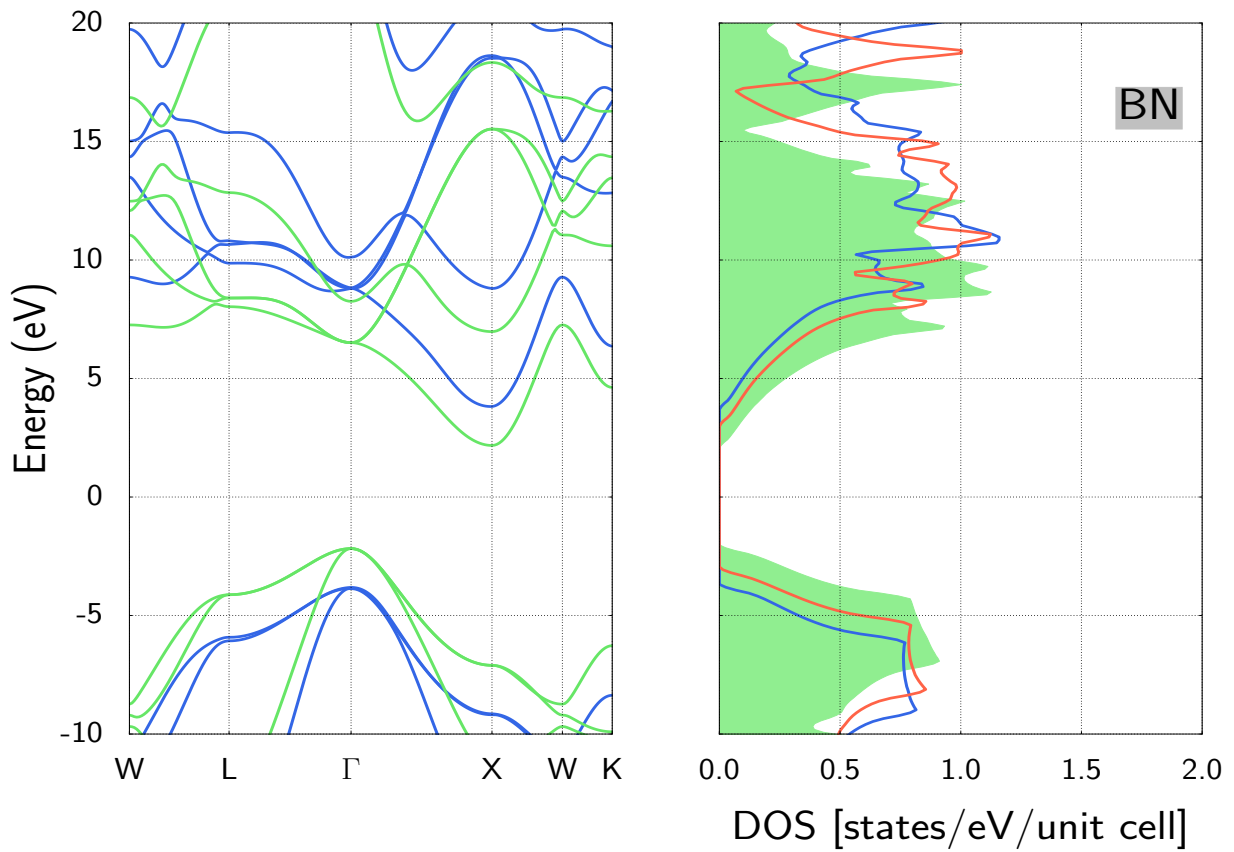
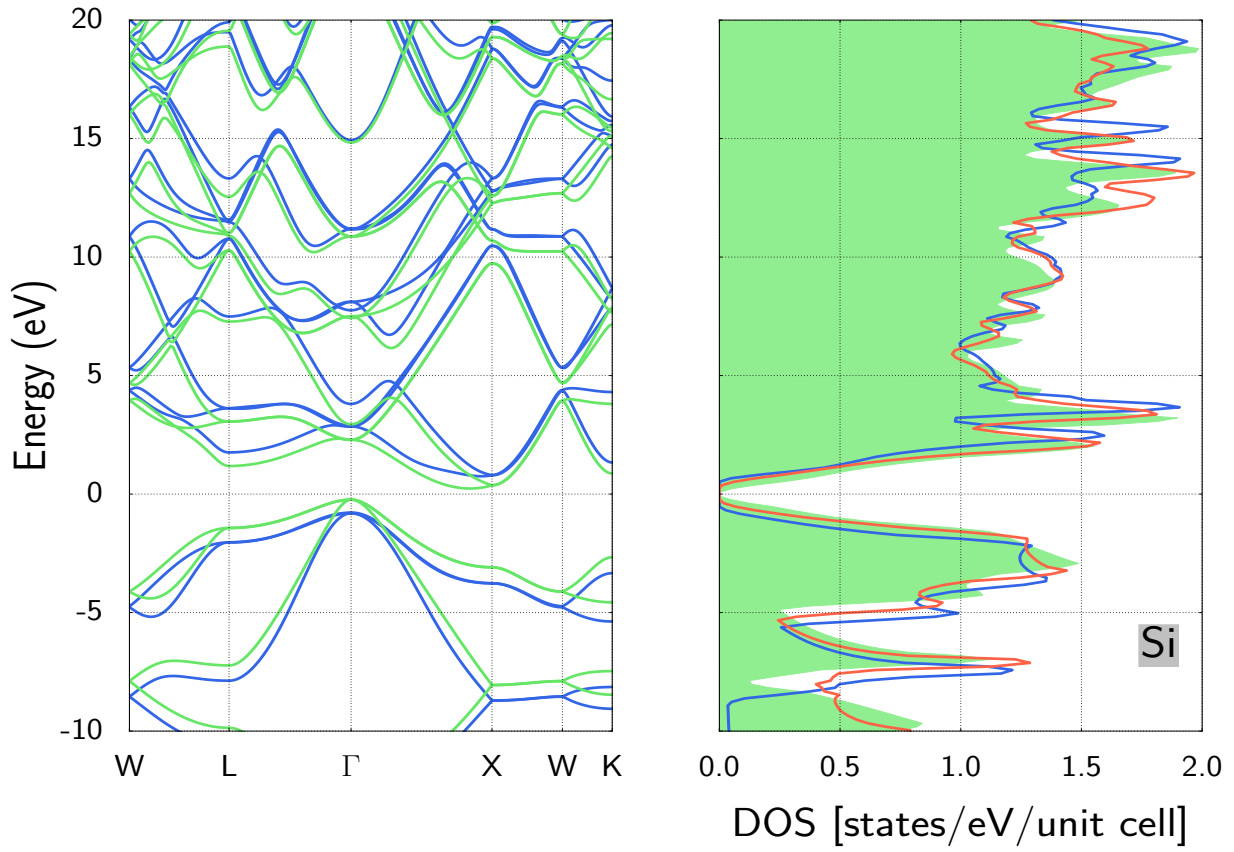
To obtain the electronic structure from  $G_0W_0$  and QSGW results on a denser  $\mathbf{k}$ -grid than the used in the calculations, we interpolate the results using maximally localized Wannier functions [88–90]. This interpolation has already been used for QSGW results, with very good results [91, 92]. The creation of the Wannier orbitals and the subsequent calculation of bandstructure and DOS diagrams uses the Wannier interpolation scheme as implemented in **exciting**, which also calculates effective masses at the CBM and the VBM [93, 94].

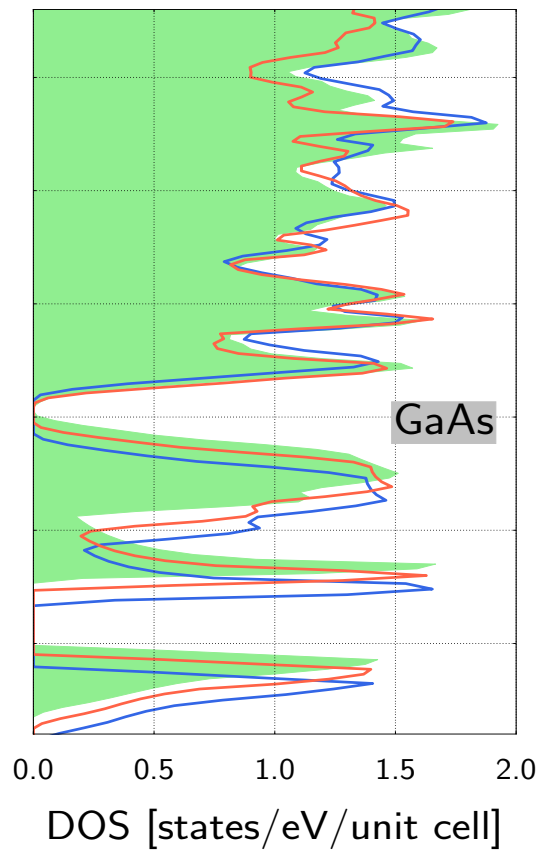
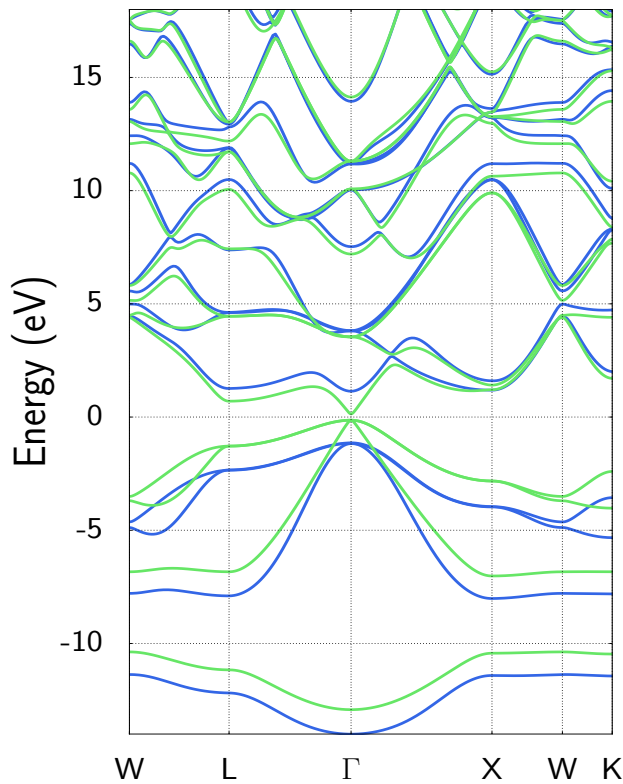
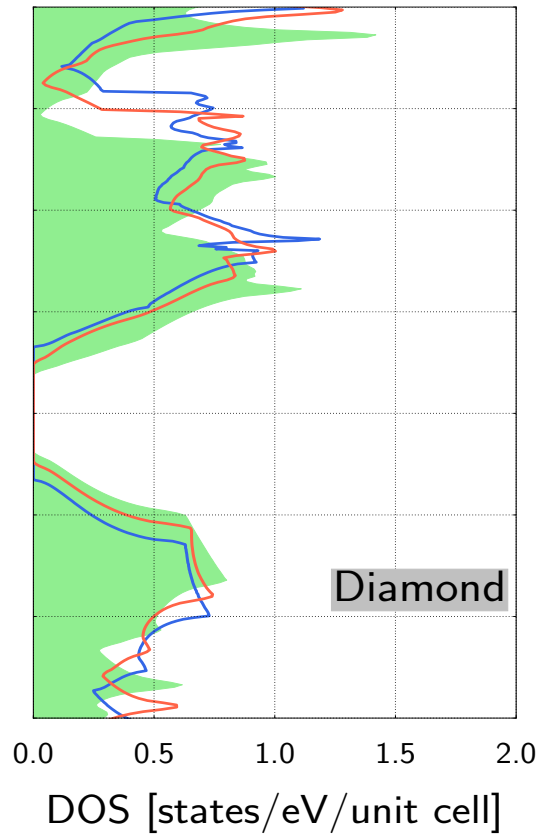
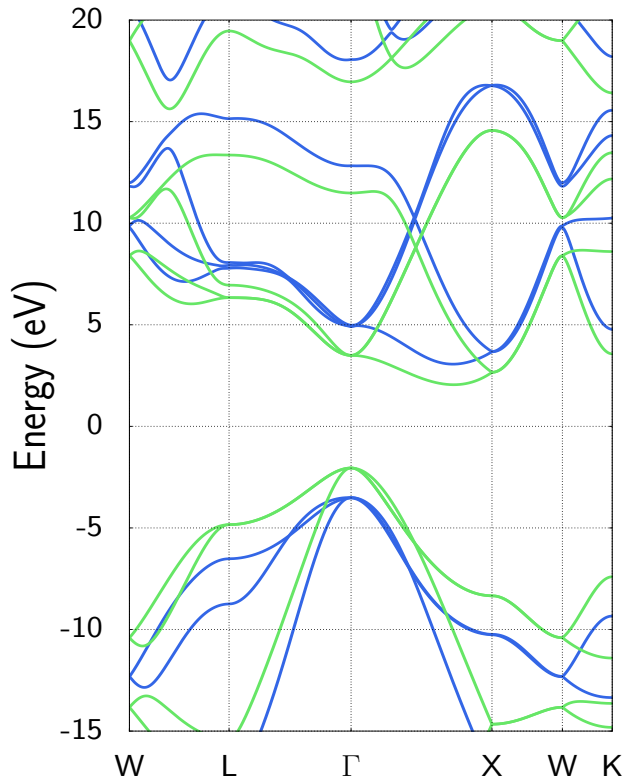
CHAPTER 7. ELECTRONIC STRUCTURE OF SELECTED MATERIALS  
BY MEANS OF QSGW

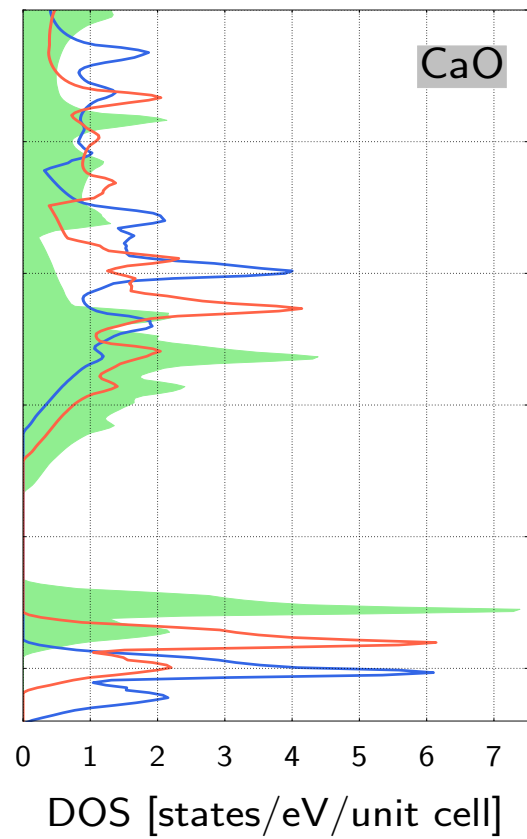
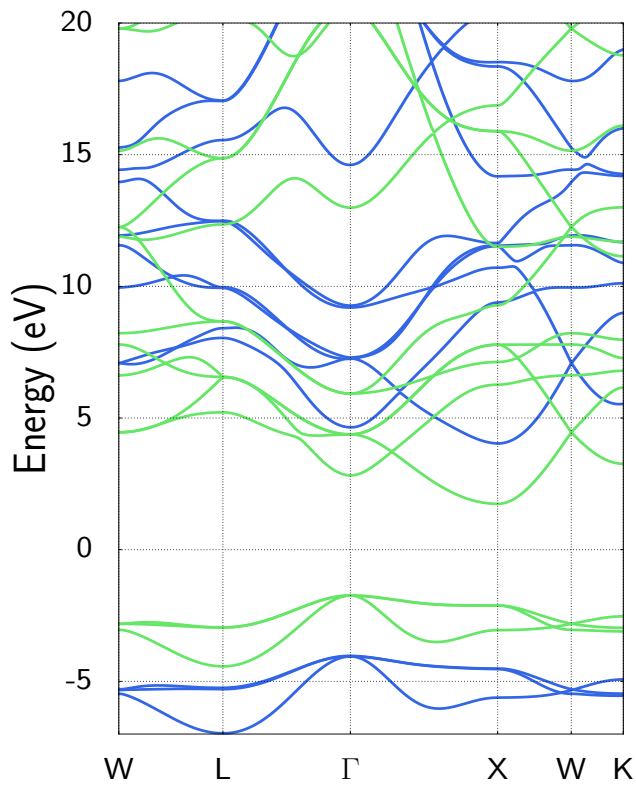
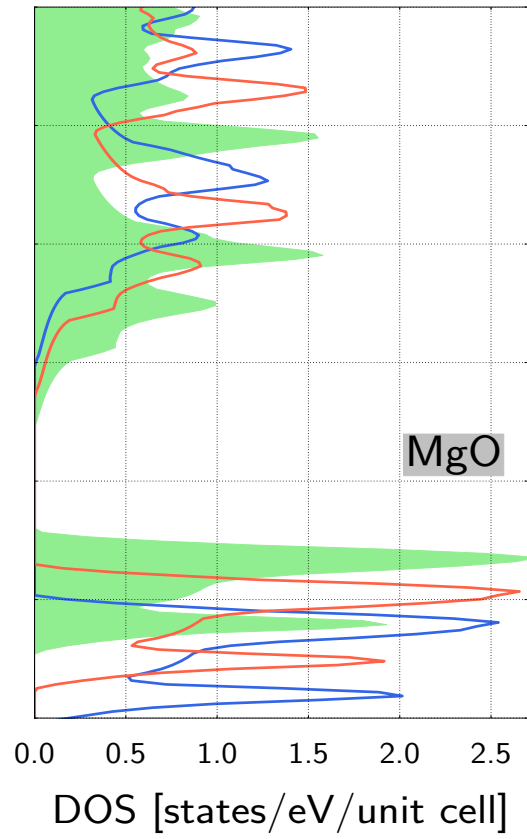
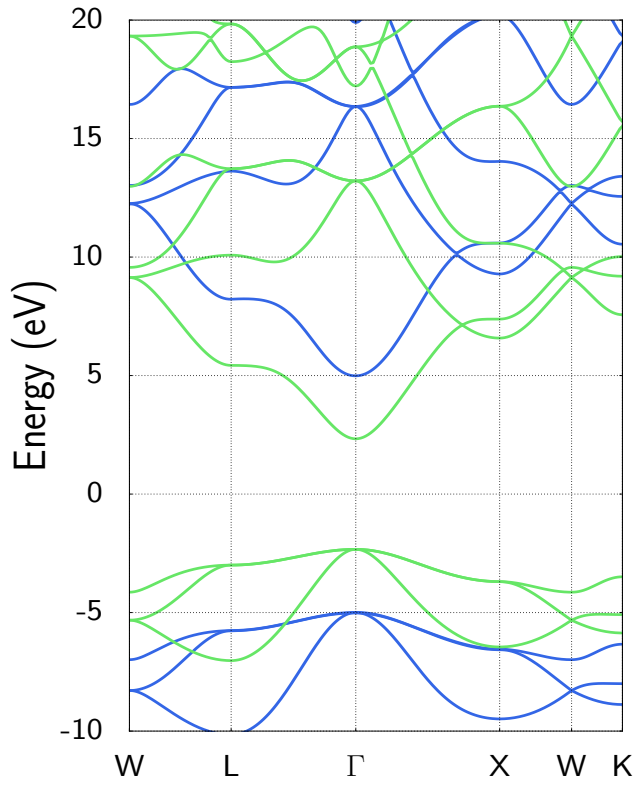
Table 7.4: Energy gaps,  $E_{\Delta}$  (eV), at  $\Gamma$ -point, and between  $\Gamma$  (VBM) and  $X$  (CBM) for the selected materials. For Si and C, the fundamental bandgap,  $E_g$ , is indirect with the CBM between  $\Gamma$  and  $X$  and values are provided separately. In the last row, the experimental values are corrected for zero-point renormalization and spin-orbit coupling, unless noted by a subscript  $e$ . The experimental bandgap of Ar and the corrected experimental values are taken from Ref. [95], with the exception of GaAs [12]. The experimental values for BN and CaO are taken from Ref. [96, 97], respectively.

$E_{\Delta}/\text{eV}$		SiC	Si	BN	MgO	CaO	LiF	Ar	C	GaAs
QSGW	$\Gamma - \Gamma$	8.35	3.64	12.61	9.97	8.68	17.10	15.33	8.41	2.24
	$\Gamma - X$	3.00	1.59	7.62	14.28	8.06	23.48	18.12	7.01	2.32
	$E_g$		1.39						6.23	
$G_0W_0$	$\Gamma - \Gamma$	7.47	3.18	11.18	7.46	6.54	13.86	12.99	7.33	1.28
	$\Gamma - X$	2.35	1.17	6.30	11.79	6.01	20.07	15.84	5.95	1.83
LDA	$\Gamma - \Gamma$	6.42	2.52	8.68	4.62	4.56	8.94	8.18	5.54	0.27
	$\Gamma - X$	1.29	0.60	4.35	8.91	3.48	14.55	10.85	4.41	1.34
Exp.		2.50	1.23	6.4 <sub>e</sub>	7.80	7.1 <sub>e</sub>	14.48	14.20 <sub>e</sub>	5.89	1.69









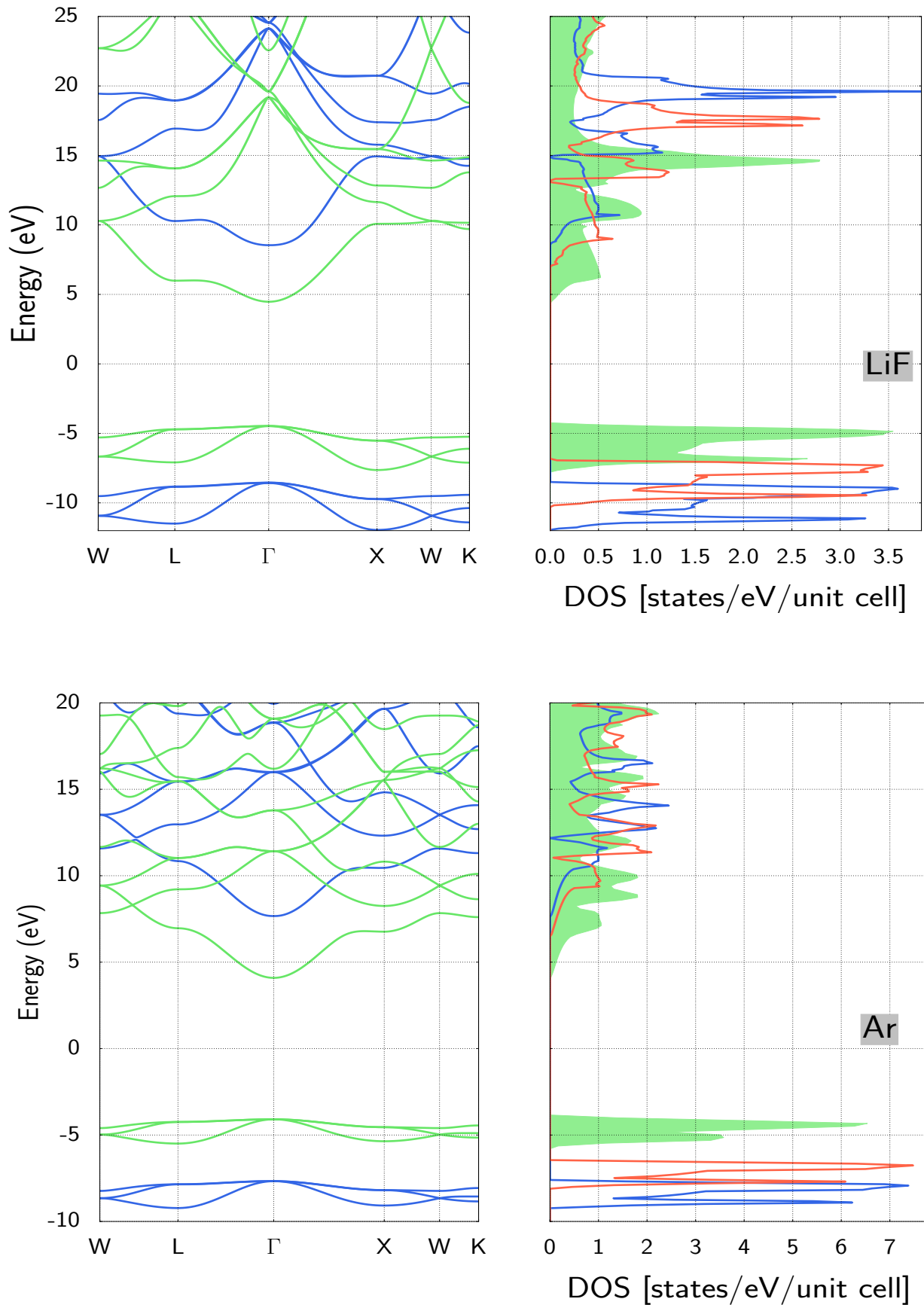


Figure 7.2: Bandstructure (left) and DOS diagram (right) of SiC, Si, BN, Diamond, GaAs, MgO, CaO, LiF, and Ar. The blue curves correspond to the QSGW results and the green curves correspond to the LDA results. In the DOS diagrams, the red curve corresponds to the  $G_0W_0$  results.

Figure 7.2 shows band diagrams and the densities of states for all considered materials. In general, the DOS from LDA,  $G_0W_0$ , and QSGW calculations present the same overall features for the valence bands, albeit shifted energies. With no exception, the VBM in QSGW is shifted downwards in energy with respect to  $G_0W_0$  and LDA, while the opposite is true for the CBM. Comparing the direct bandgap at the  $\Gamma$ -point and indirect bandgap along the  $X - \Gamma$  direction in Table 7.4, we see that the changes in these band energies due to self-consistency is not monotonic, *i.e.*, it is not a rigid shift relative to LDA. In the next, we look at different aspects in the bandstructures and DOS diagrams in individual examples.

In most cases, the shifts in energy relative to LDA due to the perturbative correction in  $G_0W_0$  follow the same trend as the QSGW results, *i.e.*, differences throughout the  $\mathbf{k}$ -grid, but with smaller changes. SiC is an exception to this trend, since the shift in energy in  $G_0W_0$  with respect to (wrt.) LDA is the same for both indirect and direct bandgaps (Table 7.4), unlike in QSGW. GaAs shows that when comparing QSGW and LDA results, the increases in the bandgaps are in a ratio 2:1 for the direct and the indirect bandgaps. For the  $G_0W_0$  results, the increase wrt. LDA is the same, meaning that in numbers, the change in the direct bandgap is 0.5 eV larger than in the indirect bandgap. In contrast, in QSGW this change amounts to  $\approx 1$  eV. Despite the same ratio,  $G_0W_0$  for GaAs is closer to a rigid shift, while QSGW shows more pronounced differences between the widenings of direct and indirect bandgap.

Like in QSGW, the differences between LDA bandgaps and  $G_0W_0$  bandgaps show dependency on the point in the  $\mathbf{k}$ -grid where the bandgap is taken. Noteworthy, for MgO the change in the direct bandgap is the same as in the indirect bandgap, for QSGW and  $G_0W_0$  results. In this case, we know that QSGW bandgaps at other points in the  $\mathbf{k}$ -grid (see Fig. 7.2) undergo changes to varying degrees relative to the LDA results. Therefore, we conclude there is no rigid shift for MgO in QSGW wrt. LDA. Regarding the energy values of the bandgaps, results from  $G_0W_0$ , in most instances, are closer to the experimental values than those calculated with QSGW (Table 7.4). However,  $G_0W_0$  results are prone to change depending on the underlying independent particle scheme, casting doubts on their reliability, which is thoroughly discussed in the literature [11, 46, 47].

In the QSGW results, the deviation of band energies with respect to experiment is not only present at the VBM and the CBM, but also in the low-energy states. As an example of the latter states, the energies of the  $3d$ -orbitals in GaAs show substantial improvement in QSGW results relative to the energies in LDA. As shown in Table 7.3, we use a large number of LOs taking up a broad range of energy parameters for QSGW and LDA calculations, enabling more flexibility to tailor the description of low-energy bands. Taking the energy of the valence band top,  $\Gamma_{1v}$ , as reference, the  $3d$ -orbitals lie 19.39 – 19.47 eV below the valence band edge in the QSGW results. This is in good agreement with the experimental value of 18.8 eV [98]. On the contrary, LDA puts these states at 14.94 eV below the reference,  $\approx 4$  eV away from experimental values.  $G_0W_0$  lowers the LDA energy values for the  $3d$ -orbitals to 18.1 below the reference. These values may also change with another starting point, but it is a substantial improvement over LDA.

We see that peaks from the QSGW results differ in both position and shape from their LDA counterpart. In the DOS from  $G_0W_0$  calculations, we see that this first perturbative correction shifts the LDA peaks closer to their position in the DOS from QSGW. Despite the difference in the positions of the peaks, the DOS for every material with both MBPT methods have, at least close to the gap, virtually the same shape for the valence band. For the conduction band, the DOS from  $G_0W_0$  calculations resembles in shape the one given by QSGW calculations, but to a lesser extent than for occupied states. In fact, the peaks in the  $G_0W_0$  and QSGW in the conduction band of diamond present disparate features, opposite to the situation for the valence band, where peaks are very similar. Instead, for the two oxides, MgO and CaO, the peaks in the DOS from both MBPT methods share the same height and show the same features in both the conduction and valence bands. Although the DOS diagram converges for calculations on denser  $\mathbf{k}$ -grids than the one presented here, the diagrams in Fig. 7.2 give a good qualitative picture.

In some QSGW calculations, the changes in curvature at the CBM and the VBM with respect to

LDA are very significant, like for GaAs (Fig. 7.2). For this compound, QSGW not only shifts the energy values of the bands, but also changes the slope of the band curve. This was also concluded from similar calculations of GaN [99] and GaAs [100]. For GaAs, the QSGW bands (Fig. 7.2) have a smaller curvature than it appears in the band diagram in Ref. [78]. However, in this publication, the QSGW implementation is modified by mixing the optimized potential  $v_{xc}^{opt}$  in the QSGW method (Eq. 4.2) with the LDA potential, possibly leading to a mismatch with our results. Comparing our band curve in the first conduction band at  $\Gamma$  for GaAs with the one reported by Chantis and coworkers [100], our results show a much larger change in slope relative to LDA. In this publication,  $v_{xc}^{opt}$  also included a portion of the LDA potential in some of the studied cases and the authors found that replacing a percentage of  $v_{xc}^{opt}$  with the LDA potential reduces the effective mass, or equivalently, increases the slope of the curve<sup>2</sup>. At least for GaAs, it appears that the difference in the slope of the band curve between LDA and QSGW may be inherent to the use of the potential  $v_{xc}^{opt}$ , which flattens the curvature. Despite the difference in curvature to our results, Chantis and coworkers report a (direct) fundamental gap, including spin-orbit coupling contribution, only  $\approx 0.4$  eV smaller than our result, *without* the mixing of both potentials.

The QSGW bandstructure of argon (Fig. 7.2) may appear to show a rigid shift of bands upon the LDA results, but a closer look shows that this is not the case. Hamann and Vanderbilt [91] discuss the differences in bandstructure in argon between LDA and QSGW schemes beyond the shift in energies. In line with our results, they observe, that the curvature of the bands in QSGW digress from the LDA bands, although, by and large, the general shape is kept. For all materials, the effect on the shape of the bands is less visible than the shift in energy, which we study next.

For argon, with weakly interacting atoms, and LiF, an ionic compound, the QSGW yields a very large correction over LDA values. Though, the increase in  $E_g$  for these materials is percentage-wise less than for the covalent material BN. In contrast to the two previous materials, the QSGW fundamental bandgaps in simpler semiconductors show a more moderate effect, in absolute terms, of self-consistency in LDA results. However, percentage-wise, the increase here is the same as for oxides. This means that in relative numbers, corrections to LDA bandgaps in large-bandgap semiconductors are not necessary larger than for small-bandgap semiconductors. Based on these comparisons, we do not observe a systematic increase in our QSGW bandgaps relative to LDA bandgaps. From our observations, the extent at which the band energies change between methods depends strongly on the material, and cannot be necessarily attributed to the size of the bandgap.

In the following, we address the overestimation of the fundamental bandgap  $E_g$  by the QSGW method with respect to experimental values (see Table 7.4). The widening of the bandgaps is the consequence of both a lowering of the valence bands and a shift upwards in the conduction bands, leading in all studied cases to gaps which are wider than in experiment. This phenomenon is already known from the literature, where the causes have often been discussed [12, 47, 82]. For instance, the fundamental QSGW bandgaps for SiC and GaAs are both overestimated  $\approx 0.5$  eV with respect to experiment, but the porcentual increase in  $E_g$  from LDA to QSGW is 43% and 12% for SiC and GaAs, respectively. In other words, for these examples, the absolute number in energy units by which the QSGW method widens the LDA bandgap does not show a clear correlation to the overestimation of  $E_g$  wrt. the experimental value. As an example, we take the (direct) fundamental bandgap  $E_g$  in argon and lithium fluoride. Within our sample set, we find the largest correction to  $E_g$  in argon (7.15 eV), with an overestimation of 1.13 eV to the experimental value. In LiF, the correction to  $E_g$  (8.16 eV) is larger than in argon, but the overestimation amounts to 2.62 eV (unlike in argon, here the experimental value is corrected for zero-point renormalization). We can conclude that we do not observe a systematic overestimation of the bandgaps.

This suggests that the causes behind the overvalued  $E_g$  depend on how many-body effects play out in different materials. The overestimation of  $E_g$  cannot be entirely explained by the size of the bandgap in the semiconductors or the degree of correction to the initial values; it is a rather complex

---

<sup>2</sup>Chantis and coworkers choose the amount of potential in QSGW to be replaced by LDA potential in order to reproduce the experimental  $E_g$  at 0 K.

interplay of causes. The reason behind the overestimation of the bandgaps is manifold, here we focus on three: (i) contributions from the zero-point renormalization (ZPR), (ii) spin-orbit coupling (SOC) effects and, (iii) lack of vertex corrections. Corrections to experimental fundamental bandgap, as expressed in Table 7.4, account for some of these aspects.

In our calculations, the atomic vibrations are neglected, *i.e.*, total absence of phonons, which affects some results more than others. The impact of electron-phonon coupling varies even among tetrahedral *sp*-semiconductors [101]. For instance, the electron-phonon coupling contributions play a more important role in the bandgap for diamond than in other elemental semiconductors, such as Si [102]. In the case of diamond, the ZPR correction *added* to the experimental  $E_g$  (Table 7.4) is 0.41 eV, while for Si this correction only amounts to 0.05 eV. This correction depends on the points in the Brillouin zone at which is calculated, and may not be available in the literature at specific directions in  $\mathbf{k}$ -space, which hampers the comparison between theory and experiment. Regarding the values of the ZPR corrections, there exist discrepancies in the literature. For diamond, Si and SiC, the corrections included in the experimental  $E_g$  in Table 7.4 stem from first-principle calculations, using the LDA potential in the DFT scheme [103, 104]<sup>3</sup>. As suggested by Antonius and coworkers for diamond [105], many-body effects have a considerable impact on the calculated corrections for the bandgap, leading to a correction of 0.628 eV to calculated  $E_g$ . *Subtracting* the latter correction for diamond to our  $E_g$ , it reduces to 5.60 eV, which indeed comes closer to the *non-corrected* experimental value  $E_g = 5.48$  eV [95]. With this in mind, we point out that the choice of ZPR correction may lead to misinterpretations of results. Nonetheless, its inclusion in the calculated electronic structure is a must in many cases, whereas in others it may be neglected [102].

In addition, the lattice also has an impact on the dielectric function in polar components. Atomic displacements in the lattice of polar compounds cause longitudinal and transversal optical phonons, affecting the electric field of the QP. The coupling of these optical modes to the electric field in the lattice contributes to the screening of the QP. Botti and Marques included this contribution to the screened Coulomb interaction of polar binary compounds on top of QSGW results [106] and found a significant narrowing of the bandgaps with respect to standard QSGW. For example, for LiF, the (direct) fundamental bandgap  $E_g$ , reduces from 15.81 eV to 13.69 eV and for MgO, it reduces from 8.94 eV to 7.71 eV. In our calculations, the bandgaps of MgO and LiF are 2 eV larger than in experiment (Table 7.4). From our set of materials, these are the materials with the largest measured longitudinal phonon frequency at the center of the Brillouin zone, *i.e.*, 0.081 eV for LiF and 0.089 eV for MgO [106]. This signals the importance of the coupling between the lattice and the electric field experienced by the QP, and the need to incorporate this effect when calculating the electronic structure of polar materials.

The second physical phenomenon omitted in the present calculations is SOC, proven of great importance in some cases [107]. The original GWA proposed by Hedin does not include a term in the Hamiltonian to make up for this phenomenon. The inclusion of SOC in QSGW calculations appears in the literature in either a perturbative or an iterative correction to the optimized Hamiltonian [92, 100, 108]. For the former scheme, the SOC term enters the optimized Hamiltonian in QSGW after it reached convergence, to return corrected eigenvalues. Following this approach, all-electron linear muffin-tin orbital (LMTO) calculations showed that the band splitting in GaAs due to SOC amounts to 0.366 eV for the first conduction band at  $\Gamma$  [100]. Similarly to the case of ZPR corrections, we find diverse values for the SOC correction for GaAs in the literature. Even among QSGW calculations, there are differences in SOC for GaAs, although these are moderate ( $\approx 0.03$  eV) [78, 109]. However, the SOC alters results (considerably) only in GaAs, therefore we do not consider it a major source of error in our results. For future improvements, we comment in the Conclusions on different ways to include SOC in the QSGW implementation in **exciting**.

The third aspect contributing to the overestimation of  $E_g$  relates to the polarizability in the RPA, see Sec. 3.4. Adopting this form of polarizability amounts to setting the vertex in Eq. 3.33 to one, *i.e.*, neglecting electron-hole interactions. Lack of such interactions leads to an underestimated

<sup>3</sup>For diamond, the ZPR correction was based on an extrapolation of experimental data using DFT results.

dielectric screening, which is reflected in the overestimation of the bandgap [110]. To make up for the lack of electron-hole interaction in the dielectric matrix, Chen and coworkers [111] included an exchange-correlation kernel in the polarizability in the QSGW implementation. The authors found that this indeed reduces the QSGW bandgaps of a vast number of semiconductors [111]. Results for C, Si, SiC and BN *without* vertex correction, reported in Ref. [111], depart in general by less than 0.2 eV from ours. On the other hand, when using the polarizability with the vertex correction, the results in this publication *with* depart by 0.3-0.5 eV for C, and SiC, and almost 1 eV for BN from our results. As an exception, the corrected result for Si in Ref. [111] is lower than our fundamental bandgap by 0.09 eV. The difference for MgO and GaAs between the uncorrected results and our results is 0.68 eV and 0.49 eV, respectively, while between the corrected results and our results is 1.67 eV and 0.73 eV. The findings in Ref. [111] are backed by QSGW calculations with a different exchange-correlation kernel [112]. Ref. [112] shows results prior to vertex corrections, which are less than 0.5 eV difference for C, SiC, SiC, BN, and GaAs and 0.8 eV for MgO apart from our results. After including the kernel in the polarizability, these differences are twice as large. Ref. [111] shows that including vertex correction in the iterative scheme closes the bandgap in Si and SiC by less than 0.4 eV, whereas in MgO by as much as 1 eV and in LiCl by 1.11 eV. Although the last compound is not included here, it serves as guidance for LiF. The vertex correction together with the above-mentioned lattice effects on the dielectric function for polar compounds, explain the large deviation of our  $E_g$  for LiF and MgO from experimental values. Generally, we anticipate a significant decrease on all our calculated energies by including a vertex correction, where the extent of its impact on the bandgaps is material-dependent.

The difficulty to cross-check our results with the literature is that the published results differ considerably among the different software packages. Bruneval and coworkers [47] claim that the deviation in results from pseudopotentials to those of all-electron methods is far from worrisome. In fact, the fundamental bandgap of Si reported by them ( $E_g = 1.47$  eV), employing pseudopotentials, lies close to our value (1.39 eV), also their reported indirect bandgap (1.60 eV) is specially close to our findings (1.59 eV). On the other hand, their result for the (direct) fundamental bandgap in argon (14.84 eV) deviates roughly half an eV from our result (15.33 eV). Comparing to another QSGW implementation based on pseudopotentials, results collected in Ref. [82] diverge strongly from our results, with differences exceeding 1 eV in several cases. However, the same authors, Shishkin and Kresse, using QSGW in a modified scheme than in the previous article, report  $E_g$  values within the RPA that are indeed closer to our results, but still smaller [112]. In the previous paragraph, commenting on vertex corrections, we discussed the non-corrected results in Ref. [112] for C, Si, SiC, and BN. In Ref. [112], they also reported  $E_g$  for argon, which is 0.4 eV lower than our result.

Reflecting on the methods behind the QSGW scheme, Gao [113] argues that the overestimation of  $E_g$  for BN (7.13 eV in his publication) may be also due to artifacts of pseudopotentials in the QSGW implementation. In any case, BN presents a larger overestimation of  $E_g$  with QSGW in our all-electron calculations than in published data from pseudopotentials calculations; this is not only true for  $E_g$  reported by Gao, but also in Ref. [112] (BN  $E_g = 7.14$  eV). This difference between all-electron and pseudopotential codes is more marked for materials with large bandgaps. Previously, discussing the work of Botti and Marques, and Chen and Pasquarello, we show that calculations based on pseudopotential for LiF and MgO return values of  $E_g$  at least  $\approx 1$  eV lower than ours, taking only the *uncorrected* values in this comparison. From all these references, we conclude that our results for simple semiconductors are roughly half an eV below pseudopotential results, with larger differences for wide bandgap materials.

With this in mind, we look at QSGW results in the literature within the all-electron realm to look into possible systematic divergences among results. The question is: *Is our implementation of QSGW on a par with others in the all-electron framework?* For the case of argon, literature for all-electron QSGW results is in indeed difficult to find. The precise value for the bandgap of CaO calculated with QSGW has not been reported<sup>4</sup>, and the experimental bandgap was measured 42

---

<sup>4</sup>In Ref. [10],  $E_g$  for CaO calculated with QSGW is plotted as a dot in Fig.1, but the values is not provided.

years ago. However, LMTO results on other materials are readily available, for which the bandgaps of Si, C, SiC, and GaAs are reported to be 1.25 eV, 5.97 eV, 2.53 eV and 1.97 eV, respectively [12]. To illustrate the dependence of QSGW results on the choice of the basis set, we compare our results with another implementation of QSGW using the LAPW method, though the self-energy there is linearized [114]. In this case, the results are: 1.41 eV, 6.71 eV, 3.08 eV, and 2.08 eV, hence much closer to our results than the LMTO results. Reference [114] also presents calculated bandgaps for MgO and LiF. For these two materials, our bandgaps are larger by ca. 0.3 eV for MgO and 0.5 eV for LiF compared to Ref. [114]; roughly a third of the deviation with respect to pseudopotential results.

From the perspective of the LAPW method, there are only few examples of the QSGW implementation. Yet, QSGW calculations using the full-potential linearized augmented-planewave (FLAPW) formalism have been tried on complex materials, but in a modified self-consistent scheme [115]. Also within the all-electron realm, Ref. [116] reports ionization potentials for molecules from QSGW calculations using the linear combination of atomic orbitals (LCAO) method. Faleev and coworkers compared QSGW results based on the LAPW and LMTO methods for silicon, and found that, for that particular case, the agreement between results was “generally excellent” [11].

To predict bandstructures with QSGW, particularly in the LAPW method, solutions to the overestimation of the bandgap were reviewed above. The array of different implementations may also affect the reproducibility and benchmarking of predicted electronic structures, which we also comment in the Conclusion.

## 7.4 Effect of Off-diagonal Matrix Elements

In this section, we look into an aspect specific to the QSGW method: the off-diagonal matrix elements of the self-energy, or  $nl$ -terms. To investigate the impact of these terms, we focus on their effect on the bandstructure. For this purpose, we performed two QSGW calculations following Eq. 4.2: (i) with state  $n$  equal to state  $l$ , *i.e.*, diagonal form of the self-energy matrix, and (ii) with  $n \neq l$ , *i.e.*, full self-energy matrix (standard QSGW).

Analyzing the results of both calculations, shown in Fig. 7.3, it is clear that the removal of off-diagonal terms opens the bandgaps. Moreover, unphysical features, such as the wrong VBM, may arise when neglecting these terms in the iterative scheme. The role of the off-diagonal terms in self-consistent  $GW$  calculations has already been discussed in literature. Using a self-consistent  $GW$  scheme similar to QSGW, Aguilera and coworkers [115] conclude that in some topological insulators, leaving out off-diagonal terms in the self-energy leads to “unphysical band dispersion in those parts of the Brillouin zone where the bands hybridize strongly”. In addition, the  $nl$ -terms in QSGW have proven to be also crucial to properly describe electronic states in molecules [117]. Here we study the effect of  $nl$ -terms in the bandstructure of Ar, SiC, diamond, and BN.

The degree of influence of the  $nl$ -terms is material dependent. For a simple sp-semiconductor such as SiC, the effect is less dramatic, which has also been observed when including  $nl$ -terms in a perturbative correction to IP eigenvalues [46]. Among the selected materials, argon shows the most pronounced effect due to the omission of  $nl$ -terms in the potential. Neglecting these terms leads to an unphysical indirect bandgap, with the VBM at  $\mathbf{k} = [0.0 \ 0.44 \ 0.44]$  starting from a direct LDA bandgap. On the contrary, including  $nl$ -terms in the self-energy returns a direct QSGW bandgap, shown in the inset for argon in Fig. 7.3, like it is observed in experiments.

In the case of SiC, the indirect bandgap calculated with the diagonal self-energy matrix is 3.87 eV, compared to 3.00 eV for the full matrix. For this simple semiconductor, the band curvature changes slightly near the band edge. For the fundamental bandgap  $E_g$  of diamond, the full-matrix case returns  $E_g = 6.23$  eV; that is 0.39 eV lower than in the diagonal matrix case. Physically, this means that here contributions from the self-energy between different states are less determinant than in the case of SiC. Figure 7.3 bottom right reflects a low degree of band mixing for diamond

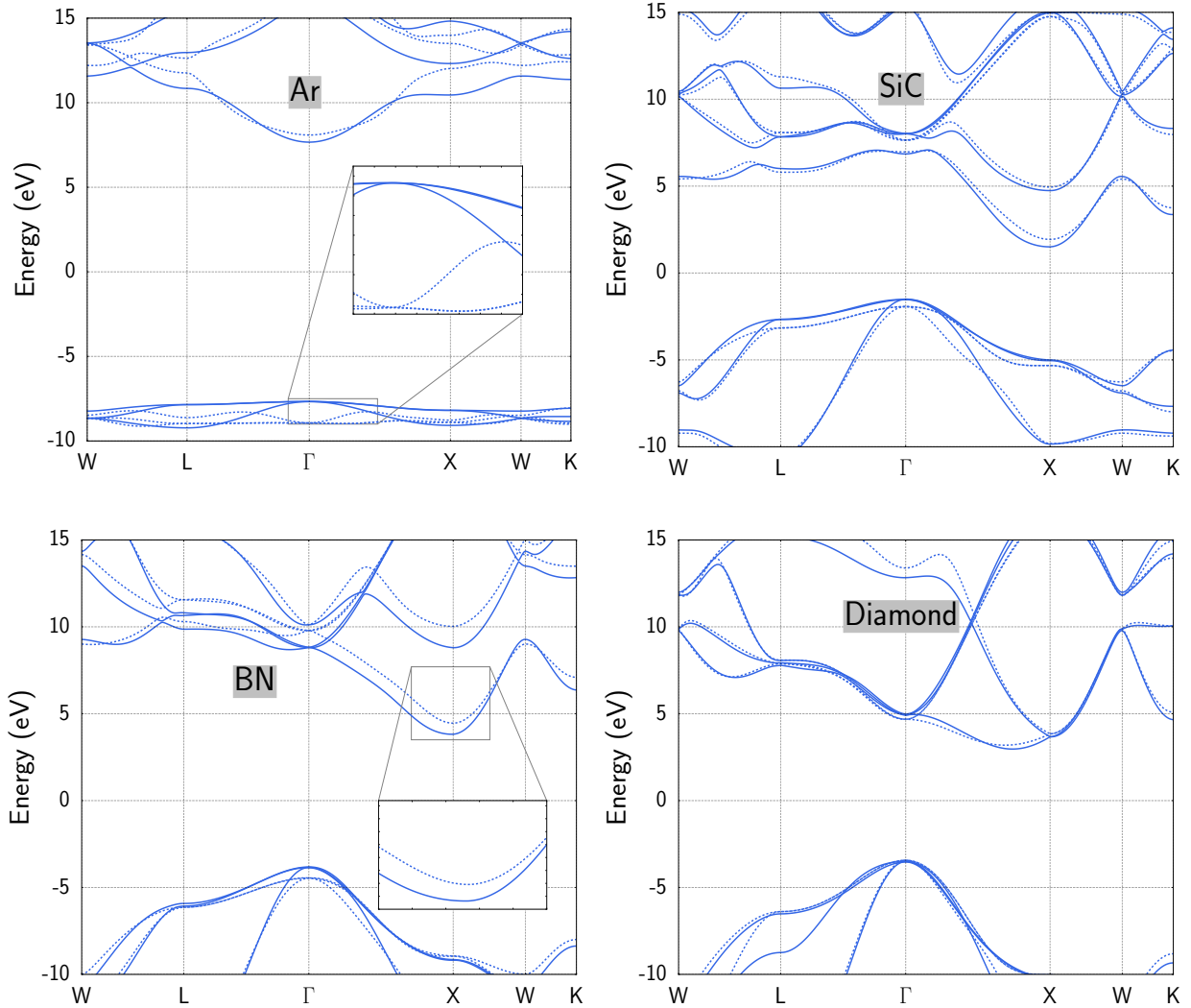


Figure 7.3: Bandstructures of Ar, SiC, BN, and diamond by means of QSGW employing the diagonal self-energy matrix (dashed line) and the full self-energy matrix (solid line).

compared to the other materials.

Like in SiC and diamond, in cubic boron nitride (Fig. 7.3 bottom left), the overall shape of the bands is barely affected by the  $nl$ -terms. However, the lack of off-diagonal contributions shifts the conduction band upwards and the valence band downwards relative to the standard QSGW, widening the fundamental bandgap by 1.3 eV. In this material, we also notice that a number of band crossings in the electronic structure vanish or reappear in one case with respect to the other. BN exemplifies an interesting aspect about the effect of  $nl$ -terms on the curvature of the first conduction band in the  $X - W$  direction: it depends on the direction in  $\mathbf{k}$ -space. From the inset for BN in Fig. 7.3, the slope of the curve in the full-matrix bandstructure is much steeper than in the diagonal-matrix counterpart, while coming from the opposite direction the slope presents less variation.

According to our results, the  $nl$ -terms in the self-energy play an important role, not only in shifting bands, but also in their curvature. In spite of their indisputable effect on many of our results, in some cases these terms are less determinant; the extent of their impact differs among materials. Contrary to these findings, Shishkin and coworkers report that the inclusion of off-diagonal terms in the QSGW Hamiltonian *increases* the bandgaps [82]. In addition, Ref. [50] shows that the numerical contribution from  $nl$ -terms is very small with respect to the diagonal elements. The findings in Ref. [50] were discussed in Sec. 4.2, where it was shown that  $nl$ -terms scale as  $\eta^{-3}$ , whereas diagonal terms scale as  $\eta^{-1}$ . Even if the values of the  $nl$ -terms are, in practice and theory, much smaller than

the diagonal elements, they may still have an impact.

We look at this last aspect in our results. To exemplify the ratio between diagonal and off-diagonal matrix elements, we concentrate on the three occupied states in BN and Diamond at the VBM. In both materials, these states are *degenerate* and belong to the *special* case introduced in Sec. 4.2. Considering the self-energy between these states, the optimized potential is calculated using matrix elements  $\langle n | \Sigma_{xc}(\epsilon_n) - v_{xc} | l \rangle$ , with  $\epsilon_l = \epsilon_n$ . While the diagonal components for BN and Diamond are of the order  $10^{-1}$  Ha, these degenerate  $nl$ -terms are of orders  $10^{-3}$  Ha. To compare with the *non-degenerate*  $nl$ -terms, we consider now the first unoccupied states  $l$  and the previous valence states at VBM, which we denote  $n$ . We look at the values of  $\Sigma_{nl}$  taken with respect to these states. BN and diamond show marked differences: the former shows these  $nl$ -terms have magnitude up to  $10^{-2}$  Ha, and the latter shows a maximum value in the order of  $10^{-4}$  Ha. In practice, off-diagonal terms are much smaller than the diagonal elements, backing the mathematical argument given by Ismail-Beigi [50]. However, there are difference between degenerate and non-degenerate off-diagonal matrix elements. Both semiconductors share the same ratio between diagonal and degenerate  $nl$ -terms. The difference is given by the non-degenerate  $nl$ -terms, which in BN approach the diagonal terms in value, whereas in diamond they have a negligible contribution to the final optimized potential.

Taking an arbitrary  $\mathbf{k}$ -point at  $[0 \ 0.5 \ 0]$  in diamond and in BN, we investigate non-degenerate  $nl$ -terms, with  $n$  for occupied state and  $l$  for the first unoccupied states. Some of these terms reach values of  $10^{-1}$  Ha in both materials, a higher value than non-degenerate  $nl$ -terms at  $\Gamma$ . Although these higher numbers make up only a small portion of the total number of  $nl$ -terms, they hint to some level of  $\mathbf{k}$ -dependency in the off-diagonal matrix elements. The diagonal and degenerate  $nl$ -terms at this  $\mathbf{k}$ -point show the same magnitudes as in  $\Gamma$ .

For argon, with low overlap between atomic orbitals, the  $nl$ -terms from degenerate states are very small for occupied states. At the high-symmetry point closest to  $\mathbf{k} = [0.0 \ 0.44 \ 0.44]$  (VBM for the diagonal-matrix case), the value of  $\Sigma_{nn}$  for the highest occupied valence band is higher in the full matrix than in the diagonal matrix. However, numerous contributions from non-degenerate  $nl$ -terms, with values of orders ranging from  $10^{-1}$  to  $10^{-3}$  Ha, balance the large diagonal terms and lower the eigenvalue of this state at  $\mathbf{k} = [0.0 \ 0.44 \ 0.44]$  relative to the  $\Gamma$  point. This returns the VBM of the full-matrix calculation in Fig. 7.3. On the other hand, off-diagonal contributions at  $\Gamma$  are negligible and do not lower nor increase the eigenvalue with respect to the diagonal-matrix result.

Besides the literature referenced in this section, to date little has been studied on the effects of  $nl$ -terms in solids. These elements, absent in  $G_0W_0$  and LDA, have an important physical meaning: the mixing of states. In the case of the noble solid, we observe that off-diagonal terms prove essential to describe the electronic structure. In fact, Bruneval and coworkers [47] compared the wavefunctions of argon in LDA and QSGW calculations and show that away from high-symmetry points, the overlap between them is poor for the conduction bands.

## Effective Masses

Analyzing the electronic structure in Sec. 7.3, we discussed the changes in the bandstructures in QSGW with respect to LDA. The slope of the dispersion and the curvature of the band vary depending on the chosen electronic-structure method. Consequently, the effective masses extracted from the dispersion also varies with the given methods. In the literature, effective masses calculated with QSGW show good agreement with experiment [78, 99, 100, 118].

We calculated the longitudinal electron effective masses,  $m_e^*$ , for Si, BN, and diamond from the dispersion curve in the interpolated bandstructure. For silicon, where the longitudinal direction is  $(1 \ 0 \ 0)$ ,  $m_e^*$  is 0.81, in units of the free electron mass,  $m_o$ . Compared to the experimental value ( $0.91m_o$ ), our result underestimates the real effective mass [119]. This underestimation is present also in diamond for the standard (full self-energy matrix) QSGW calculation, see Table 7.5. From literature, the longitudinal  $m_e^*$  calculated with QSGW for GaN [99] and for diamond [118] are smaller

than in experiment, while for GaAs (with the correction to  $v_{xc}^{opt}$  explained in Sec. 7.3), is only slightly under the measured value [78].

Additionally, we calculated the effective mass of the heavy hole,  $m_h^*$ , for BN and diamond in the (1 0 0) direction at the CBM. Unfortunately, it is difficult to draw a general trend for the ratio between  $m_e^*$  and  $m_h^*$  based only on two materials. As well, for diamond, the discrepancies among experimental values, and also theoretical results, hinder the comparison of such ratio to published data.

Table 7.5: Effective masses in the  $\Gamma - X$  direction for diamond and BN employing the full self-energy matrix (first column) and diagonal self-energy matrix (second column), in units of the free electron mass  $m_o$ . References to experimental [120, 121] and theoretical [118, 122, 123] data are given in the last column.

	Full QSGW		Diag. QSGW		Reference values			
	$m_e^*$	$m_h^*$	$m_e^*$	$m_h^*$	$m_e^*$		$m_h^*$	
C	1.05	0.77	1.65	0.65	1.4 [120]	1.56 [121]	0.32 [118]	0.50 [122]
BN	0.81	0.76	0.50	1.13	0.81 [123]		0.54 [123]	

As explained in the previous section, the band dispersion changes when excluding  $nl$ -terms. SiC and BN, zinc blende structures with longitudinal direction  $\Gamma - X$ , show very similar response to the inclusion of  $nl$ -terms. For the VBM, the heavy hole is heavier for the diagonal self-energy calculations, as the curvature is smaller than in the bandstructure given by the full self-energy, see Table 7.5. Regarding the effect of  $nl$ -terms at the VBM, the dispersion changes markedly for BN (inset Fig. 7.3) in one direction more than the other. The  $nl$ -terms are important not only to predict energies, but also the effective masses. This may explain, in part, the differences between effective masses from  $G_0W_0$  and QSGW calculations reported in the literature [10, 118].

In the case of diamond, the band curvature at VBM is slightly affected by  $nl$ -terms, as reflected in the hole effective mass  $m_h^*$  in the (1 0 0) direction. A drawback when calculating  $m_h^*$  for diamond is that the dispersion at the VBM is less parabolic, adding uncertainty to our results. For  $m_e^*$  in diamond, the result from the diagonal self-energy calculation is closer to the experimental value than the result with the full matrix. This quantity was also calculated by Löfås and coworkers [118] using QSGW, shown in Table 7.5. This publication reports a longitudinal effective electron mass of  $1.2 m_o$  calculated with QSGW, which indeed is close to our standard QSGW result of  $1.05 m_o$ . The calculation of  $m_e^*$  in diamond demands a finer  $\mathbf{k}$ -grid, because the CBM lies away from a high-symmetry point, challenging the Wannier interpolation in that vicinity. Despite this aspect, our results give a qualitative picture of the effect of  $nl$ -terms on the effective masses of diamond.

## 7.5 Starting-Point Dependence

Despite its success in predicting the electronic structure of many materials, the  $G_0W_0$  method suffers from an intrinsic flaw: the dependence on the underlying eigenvectors and eigenvalues, referred to as *starting-point dependence*. The IP schemes treat the particle interactions through different mean-fields (see Sec. 2.2), depending on the approximation. Reportedly,  $G_0W_0$  results show noticeable variations depending on the previously chosen IP scheme **exciting** [95, 124]. As explained in Chapter 4, self-consistency cures the starting-point dependence of perturbative corrections. Contrary to this argument, Liao and Carter [125] did find a considerable starting-point dependence in QSGW for hematite  $Fe_2O_3$ . However, the vast majority of publications, referenced below, show that QSGW cures the starting-point dependence. This is indeed the case for our QSGW calculations on Ar, SiC, and C, employing three initial choices of exchange-correlation potential: PBE0, HFA, LDA. We chose these materials in order to sample bandgaps with very different sizes.

As depicted in Fig. 7.4, the QP eigenvalues in the case of argon are practically the same for all three starting points bandstructures. The same holds for diamond and silicium carbide; the indirect  $\Gamma - X$  bandgap for these materials vary almost negligibly among the different starting-points, see Table 7.6.

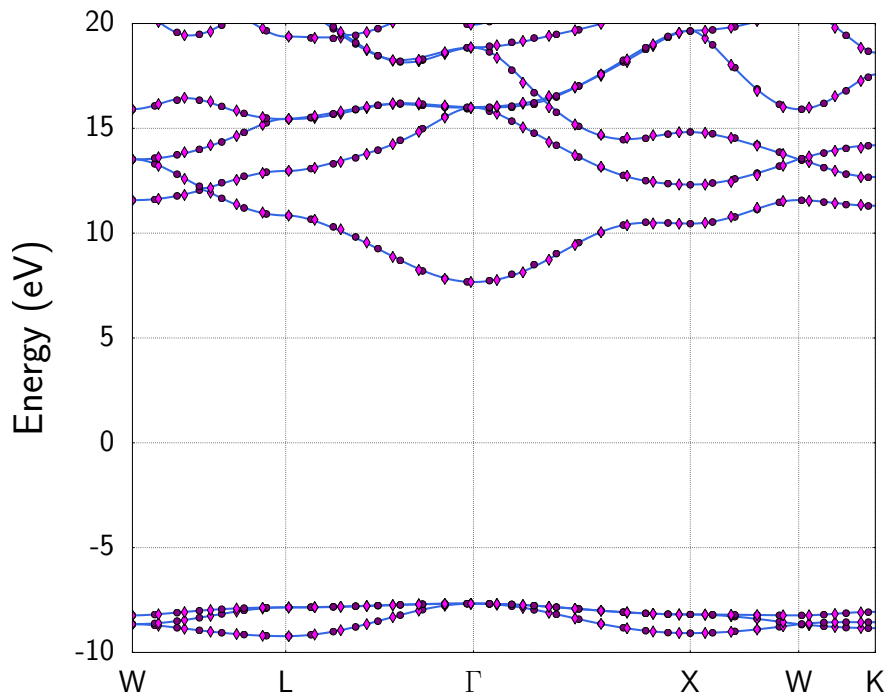


Figure 7.4: Calculated bandstructure of solid argon with QSGW@LDA (solid blue line), QSGW@HF (purple circles), and QSGW@PBE0 (pink diamonds).

Table 7.6:  $E_{\Delta}$  (eV) at high-symmetry points for C, SiC, and Ar together with the number of iterations till convergence. As reference, the two last columns show the results of the  $G_0W_0$  calculations on top of LDA and PBE0 results, taken from Ref. [95].

	QSGW@LDA		QSGW@PBE0		QSGW@HF		$G_0W_0$ @LDA	$G_0W_0$ @PBE0
	$E_{\Delta}$	Iterations	$E_{\Delta}$	Iterations	$E_{\Delta}$	Iterations	$E_{\Delta}$	$E_{\Delta}$
C $\Gamma$ -X	7.01	6	7.00	7	6.99	10	5.95	6.26
SiC $\Gamma$ -X	3.00	5	3.03	8	3.03	6	2.43	3.13
Ar $\Gamma$ - $\Gamma$	15.33	5	15.34	4	15.33	3	12.99	13.28

Supported by these findings, we conclude that, in these cases, the self-consistency cures the starting-point dependence on the initial  $G_0$ . On the contrary,  $G_0W_0$  results show that the perturbative corrections vary considerably depending on the initial choice of the exchange-correlation potential (for example, 0.7 eV difference in results for SiC).

It is not evident from Table 7.6 that the closer the underlying results from IP schemes are to, for instance, the experimental value, the fewer the number of iterations needed for convergence. Insulators such as Argon do profit from initial results (first iteration) using HFA. For this material, the initial  $E_g$  (direct  $E_{\Delta}$  in Table 7.6) in the QSGW@HF calculation is 14.96 eV, very close to the converged value, and thus this calculation requires such a low number of iterations.

Yet, the same is not true for diamond, where the initial indirect bandgap in the QSGW@PBE0 calculation (6.10 eV), although much closer to the final value than in the QSGW@LDA (4.12 eV), converges more slowly. Most counterintuitive is the case of SiC, where the fundamental bandgap

$E_g$  (the indirect  $E_\Delta$  in Table 7.6) in the QSGW@PBE0 case is 2.07 eV, *i.e.*, the closest to the final result, but the fastest converging calculation is QSGW@LDA, with an initial  $E_g$  of 1.25 eV. In fact, the QSGW@HF calculation for SiC starts with  $E_g = 5.19$  eV, and still converges faster than QSGW@PBE0. In contrast, Koval and coworkers studied convergence of QSGW@LDA and QSGW@HF on small molecules, in an all-electron scheme, and found that both calculations took the same number of iterations to reach convergence [116].

In line with our results, the starting-point independence is also tested for other types of hybrid functionals. Examples of QSGW calculations on complex oxides with the Heyd-Scuseria-Ernzhof (HSE) functional as initial potential show that different input parameters return the same  $E_g$  [126]. In a study performing QSGW calculations on oxides, the initial GGA potential combined diverse initial values of the Hubbard-type correction  $U$ , and here as well the final results were only weakly dependent on the amount of  $U$  involved [127]. Also in molecules, Kaplan and coworkers [117] found that the converged results in QSGW did not vary when calculated on top of PBE with different proportions of exact exchange. These studies together with our observations hint at the generality of the QSGW results, which are not bound to the initial parametrization of the potential in the IP scheme. However, choosing the right starting point may save some iterations in QSGW, which is computationally very involved, like in the case of argon.

## 7.6 Charge Density

The charge density is a telling property, its distribution in space is related to the nature of the chemical bond between atoms. For example, in ionic compounds the electronic density is more present closer to the electronegative atoms than in covalent compounds. Thus, the accurate description of the material depends on the electronic density distribution given by the electron wavefunctions, as defined in Eq. 2.15. DFT provides wavefunctions which are close to the QP wavefunctions [7], however for some cases, poor overlap between both wavefunctions shows they differ considerably [47]. Through the iterative update of the wavefunctions, we expect a change in the charge density distribution going from the Kohn-Sham (KS), employing LDA, to the QSGW method. To investigate the effect of self-consistency on the density, we plot the charge-density difference  $\Delta\rho(\mathbf{r})$  between LDA and QSGW calculations, which in theory reads:

$$\Delta\rho(\mathbf{r}) = N \int |\Psi^{\text{LDA}}(\mathbf{r})|^2 - |\Psi^{\text{QP}}(\mathbf{r})|^2 d\mathbf{r}_2 \cdots d\mathbf{r}_N. \quad (7.1)$$

Different isovalues, corresponding to a specific value of  $\Delta\rho(\mathbf{r})$  in space, were chosen to better visualize where in the unit cell the larger and smaller changes in density take place.

We take as a first example the salt LiF, a highly ionic compound with a large difference in electronegativity between the components. For the electronic-density calculations we take a dense grid, 400 points in each spatial direction, allowing for a careful follow up on density displacements due to self-consistency on top of LDA. Regarding the LDA results as the initial electron density, we infer that the many-body iterative scheme produces a shift in density towards the atoms, at expense of some of the density from the inter-atomic space.

The three isosurfaces in Fig. 7.5 depict the charge-density difference in LiF between calculations. For the higher isovalue, the isosurface in Fig. 7.5 (c) shows that, in contrast to the LDA density, in the QSGW results the space between ions is less filled with charge density, whereas the vicinity of the anion holds a higher charge density. In fact, Kaplan and coworkers have shown that QSGW gives a dipole moment in good agreement with experiment, while DFT (using PBE) underestimates it [117]. For low-energy states in the QSGW and LDA calculations, we remove the  $1s$  state of lithium from the core states and treat it as a valence state. This approach allows us to tailor the description of semi-core states by including LOs, whose linearization energies are in the range of  $-40$  eV. Through the iterations, the first occupied valence state lowers its energy by 10 eV from its initial LDA value,

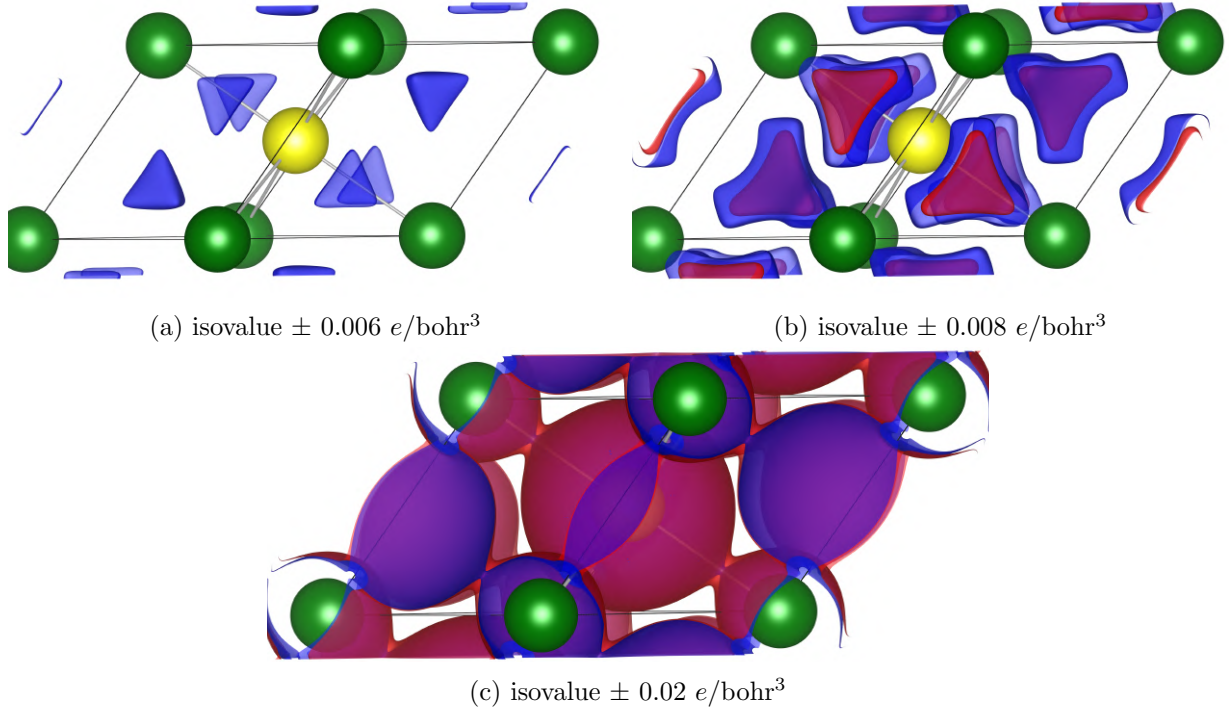


Figure 7.5: Charge-density differences between QSGW and LDA calculations for LiF. Positive difference is blue, and negative is red. Yellow spheres depict fluorine, while green spheres represent lithium atoms.

explaining the shift in electron density towards the nuclei. However, at low  $\Delta\rho$ , Fig. 7.5 (a), we see a modest increase in density at inter-atomic spaces. At this small isovalue ( $\pm 0.006 e/\text{bohr}^3$ ), the number of non-zero scalar points is much smaller than for the two other isovalues. This shows that the total change in density for LiF takes place mostly in large amounts in the spaces surrounding the atoms.

Although there is plenty of DFT electronic structure calculations on calcium oxide, listed in Ref. [128], it has been less studied with MBPT methods [129], making it difficult to compare our results with the literature. From x-ray spectra, we know that the charge density at a distance of 0.18 bohr from the nucleus is about four times higher around calcium than around oxygen [130]. In QSGW, the metal atom experiences an increase in charge density around it relative to LDA. On the other hand, in Fig. 7.6 (a), a cross section cut around the oxygen atom—at isovalue  $\pm 0.01 e/\text{bohr}^3$ —shows that the *immediate neighborhood* around the oxygen is less populated with electronic charge than in the QSGW calculations. Apart from this small region, QSGW calculations enhance a larger electronic density around calcium and oxygen atoms.

The situation away from the red-sphere (see Fig. 7.6) around the oxygen is somewhat different. Band widths of the O(2s) and O(2p) orbitals calculated with LDA are larger by  $\approx 0.5$  eV than band widths extracted from electron momentum spectroscopy measurements (EMS) [131]. QSGW cures in part the delocalization of these electrons in LDA, by adding density to the surroundings of oxygen, clearly represented by the positive  $\Delta\rho$  at the center in Fig. 7.6 (b). At higher isovalues, the number of scalar values in the grid, which are positive, are fewer in number than at lower isovalues. This means that charge depletion after the QSGW iterations occurs in small amounts and re-distribution of charge is moderate. For the rest,  $\Delta\rho(\mathbf{r})$  in CaO resembles the case of LiF; by implementing the optimized potential, charge density moves away from interstitial space and closer to the alkali-metal atom, confirming a localization of electronic density when going from the mean-field approach to the many-body iterative scheme.

From all the  $\Delta\rho(\mathbf{r})$  points in the volumetric data, those in the LiF are much higher valued—two orders of magnitude—than in CaO. This points to less overlap between initial and converged total wavefunction in LiF than in the oxide, see Eq. 7.1. Isosurfaces at higher values in CaO tend to

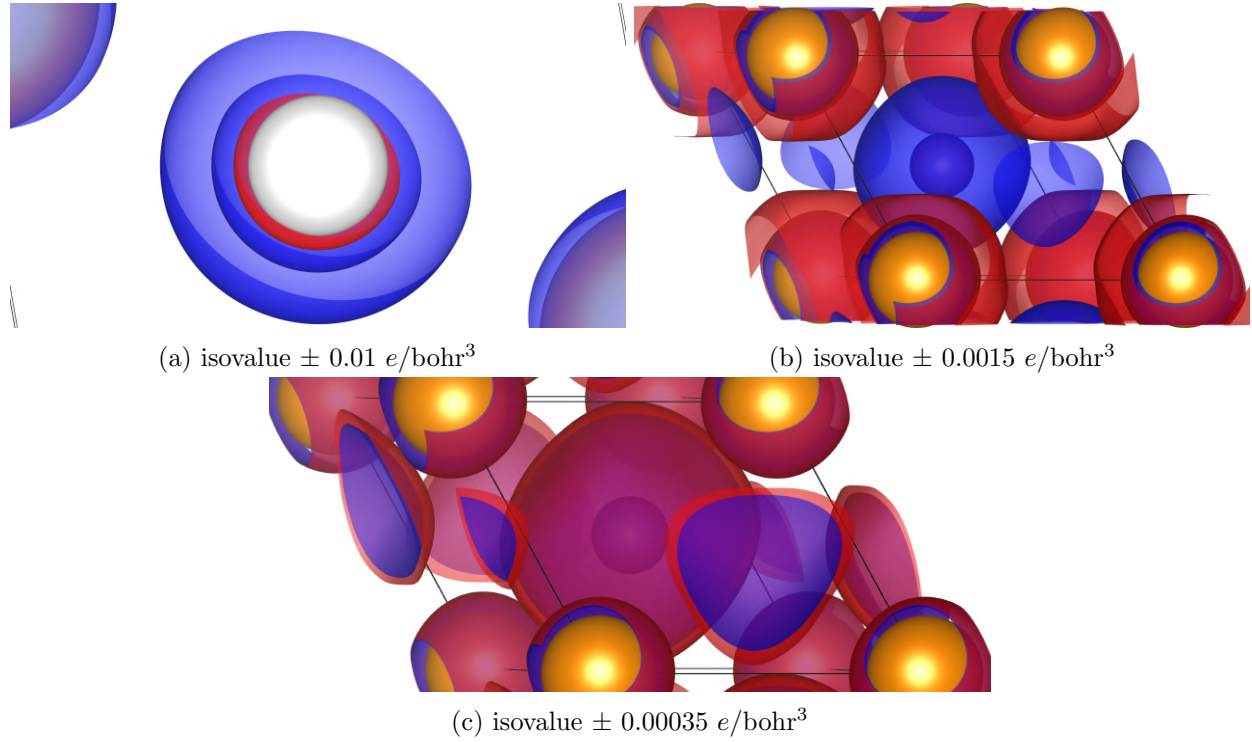


Figure 7.6: Charge-density difference plot for CaO. The center atom, in white, is oxygen. Orange spheres depict the calcium atoms, positioned at the corners of the unit cell.

disappear, but the opposite trend is true for the salt. At isovalues of  $\pm 0.15 e/\text{bohr}^3$ , where a positive charge-density difference surrounds fluorine and a negative surrounds lithium, the density difference is still clearly visible, although much less present than compared to Fig. 7.5 (c). In other words, the shift in density for the LiF takes place mostly by removing larger amounts of density from determined regions of space, and re-distributing to different regions in the unit cell to varying degrees.

## 7.7 Quasiparticle Wavefunctions

As mentioned in the previous section, the wavefunctions of the LDA calculations may differ from their counterparts in the QSGW method. However, for a number of semiconductors, we know from literature that the wavefunctions in LDA serve as a good starting point for MBPT calculations. To know how LDA and QSGW wavefunctions compare to each other, we are interested in studying this aspect in more detail in MgO, where this aspect has not been yet studied. For this purpose, we focus on particular electronic states in magnesium oxide, rather than looking at the whole density. We plot the square modulus of the wavefunction in space, *i.e.*, the probability amplitude distribution, for both the LDA wavefunction (LDA-WF) and the quasiparticle wavefunction (QP-WF) at the CBM and the VBM.

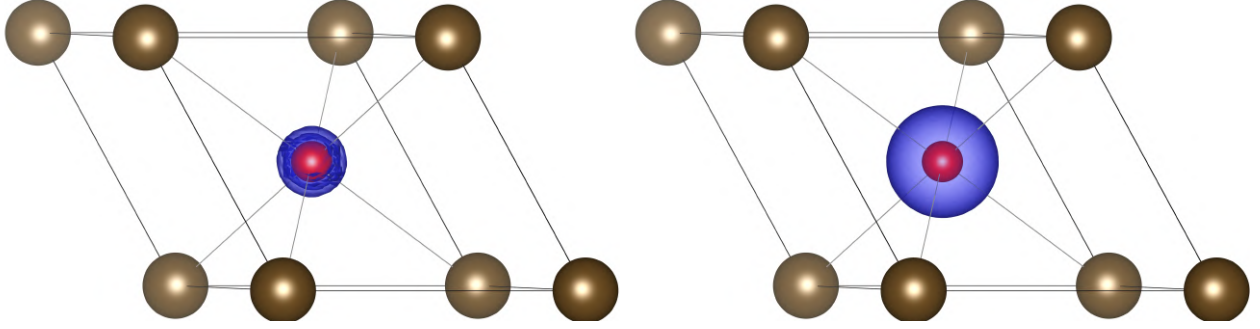


Figure 7.7: The figure shows the isosurface (blue) of the squared norm of the LDA-WF (left) and QP-WF (right) at  $\Gamma$  for the first conduction band in MgO. The isovalue has been chosen as  $3 \cdot 10^{-4} e/\text{bohr}^3$ . Brown spheres at the corners depict the magnesium atoms, and the red sphere at the center represents oxygen.

In MgO, the CBM obtained from QSGW is shifted up 2.30 eV with respect to LDA. On that account, we expect the state at the CBM to become less attached to the center of the atom. Accordingly, the lowest conduction state, plotted in Fig. 7.7, is visibly more delocalized when calculated with QSGW than LDA. For this analysis, we took the largest isovalue for which the isosurface is visible for both calculations. For the highest probability amplitude, the LDA-WF on the left remains very close to the oxygen atom, while the QP-WF on the left spreads out. This delocalization is also present at the VBM (Fig. 7.9), but to a higher-order isovalue, *i.e.*, larger probability amplitude.

The VBM in MgO is formed by hybridization of oxygen  $p$ -orbitals, which form three degenerated bands. To compare the LDA-WF and the QP-WF, we look at one  $p$ -orbital in the highest occupied band at the  $\Gamma$  point, plotted in Fig. 7.8 with both panels rotated with respect to the previous figure. In this last example, we also choose the largest isovalue for which the isosurface is visible. It appears that the  $p$ -orbital is more delocalized in QSGW calculations, although it lies at lower energy (see bandstructure of MgO in Fig. 7.2). To achieve a thorough conclusion, we need to complete the observation by looking at the sum of the squared norms of the three degenerate states.

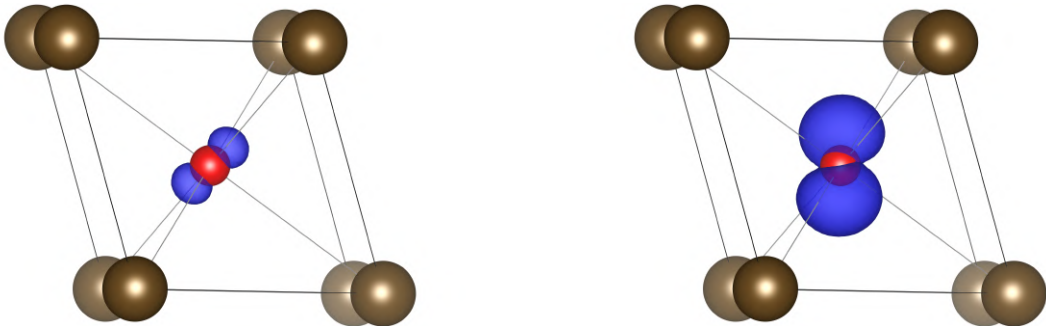


Figure 7.8: The figure shows the isosurface of the squared norm of the  $p$ -orbital state in LDA (right) and in QSGW (left) at  $\Gamma$  for the highest occupied band in MgO. The isovalue has been chosen as  $1 \cdot 10^{-3} e/\text{bohr}^3$ . Different rotations in space of the unit cell with respect to Fig. 7.7 are meant to facilitate visual comparison. Color code like in Fig. 7.7.

For a wide range of isovalues, the sum of the squared norms of the three degenerate electronic states,  $\psi$ , at the VBM has a spherical shape, which besides being slightly larger for the QP-WF, does not differ much between methods. However, the differences are at the very high and very low values of probability amplitudes. At larger probability amplitudes, as displayed in Fig. 7.9, the isosurface at the VBM calculated with QSGW forms a sphere around the oxygen, while the LDA-WF does not return probability amplitudes in this range. According to these observations, the probability

of finding the charge near the oxygen is higher in QSGW than in LDA. Despite the difference in magnitude, the probability amplitudes at the VBM show the same *trend* in both methods; the closer to the oxygen, the higher the probability to find the electron. We ask the question whether the QP-WF may be more localized than the LDA-WF. In order to refute or accept this hypothesis, we look at the behavior of the  $|\psi|^2$  isosurface at much lower isovalues.

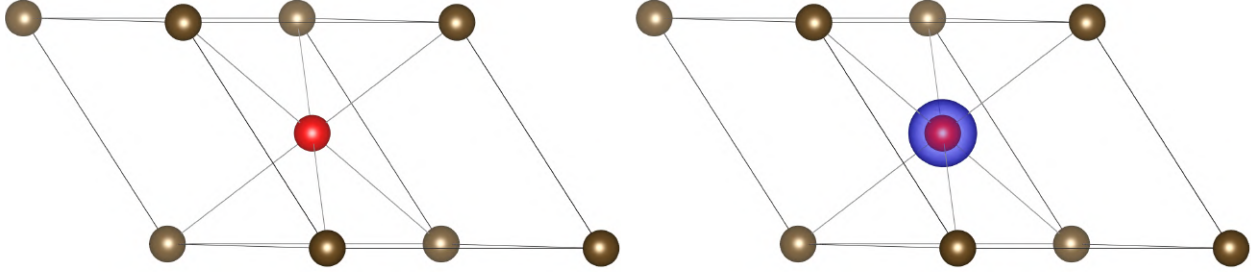


Figure 7.9: The figure shows the isosurface of the squared norms of the of the three degenerate LDA-WFs (left) and QP-WFs (right) at  $\Gamma$  for the highest occupied band in MgO. The isovalue has been chosen as  $5 \cdot 10^{-3} e/\text{bohr}^3$ . Color code like in Fig. 7.7. The spheres depicting atoms have reduced radii compared to the last figure.

Figure 7.9 and Fig. 7.10 show two extrema in the spatial grid of the volumetric data. Physically, this means we look at when the probability of finding the electron is very high and when it is very low. Relative to QSGW results, the isosurface of  $|\psi|^2$  in LDA exhibits a similar spherical shape around the oxygen for isovalues around  $1 \cdot 10^{-3}$  (not plotted here). On the contrary, at very small values of  $|\psi|^2$  (Fig. 7.10), we see the isosurface covering a larger area for LDA results, *i.e.*, in QSGW calculations the probability amplitude decreases more abruptly when moving away from the oxygen atom.

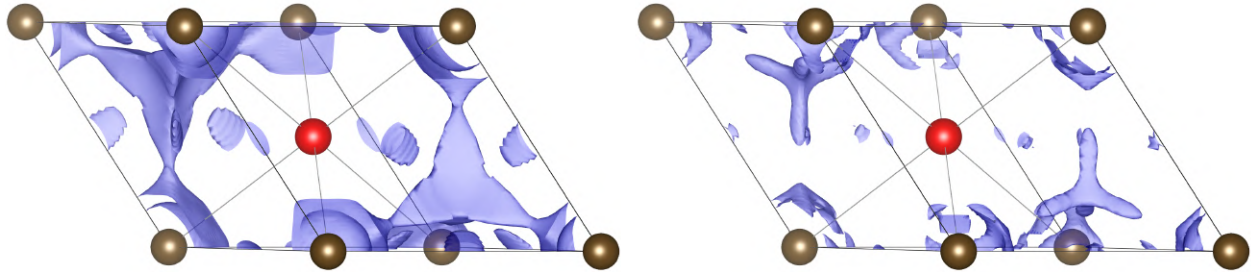


Figure 7.10: The figure shows the isosurface of the squared norms of the of the three degenerate LDA-WFs (right) and QP-WFs (left) at  $\Gamma$  for the highest occupied band in MgO. The isovalue has been chosen as  $1 \cdot 10^{-6} e/\text{bohr}^3$ . Color code like in Fig. 7.7.

Comparing the probability amplitude at these two values (Fig. 7.9 and Fig. 7.10), we conclude that the charge at the VBM by means of QSGW gathers around oxygen, while its presence in the space between atoms is less probable. On the other hand, the probability amplitude in LDA is more evenly distributed in space than in QSGW. We conclude that, at the VBM, LDA shows larger delocalization of the charge as in QSGW. In QSGW, the probability of finding the electron near oxygen is much higher than in LDA.



# Chapter 8

## Conclusions and Outlook

In this doctoral work, we have successfully implemented the quasiparticle self-consistent GW (QSGW) method in **exciting**, employing the linearized augmented planewaves (LAPW) method. We calculated the electronic structure of nine materials and, by means of the Wannier interpolation, obtained their bandstructures and the densities of states. Characteristic of the QSGW method is the inclusion of off-diagonal terms in the self-energy matrix. To study the contribution of these matrix elements to the overall electronic structure, we perform additional electronic structure calculations using the diagonal self-energy matrix in four cases, comparing QSGW results obtained with the full and the only-diagonal self-energy matrix. Additionally, we included calculations of effective masses on diamond and boron nitride. To investigate the starting-point (in)dependence of the QSGW method, we performed QSGW calculations in Ar, BN, diamond, and SiC based on three different initial mean-field schemes. We conclude that the final results vary negligibly with respect to the initial eigenvectors and eigenvalues. To complete the picture of the electronic structure, we look into the total charge density and probability amplitudes of electronic states in QSGW relative to LDA. To investigate the first aspect, we took lithium fluoride and calcium oxide to exemplify the changes in the electronic density of LDA calculations caused by the iterative scheme in QSGW. As for the probability amplitudes, we chose magnesium oxide to show the behavior of the wavefunction at the valence band minimum and conduction band maximum, using the QSGW method in contrast to the initial wavefunction given by LDA calculations.

The implementation of the QSGW method in **exciting** offers new possibilities to include every core state at all stages of the calculations. In addition, the inclusion of local orbitals is available for semi-core and valence electrons. Due to these features and the basis functions in the LAPW method, the radial functions  $u_{l\alpha}(r, E_{l\alpha})$  appear very often in our implementation, with the search for the energy parameter carried out either previously to or in the first iteration of the QSGW calculation. To calculate the radial functions, the local potential entering the Schrödinger radial equation makes use of the electronic density. Although this procedure is standard in DFT, it is not possible in the implementation of QSGW, due to the non-locality of the potential in this approach. The electronic density given by the optimized potential in QSGW does not necessarily return physically valid solutions when inserted in the local potential of the radial equation. Therefore, the radial functions remain fixed in the QSGW implementation. This opens the door to a new challenge: how to effectively update radial functions —together with their derivatives— participating in the basis set of the LAPW and APW methods, and local orbitals. As well, we express operators in many-body perturbation theory (MBPT) as matrices in the mix basis representation, which includes an integral of the product of three radial functions. It remains unknown at which extent the fixed integral affects the final outcome of the calculations. Because of all these aspects, it is desirable to be able to update radial functions according to the *updated* density throughout the iterations. Likewise, if radial functions were updated, the energy parameters of these functions could also be re-optimized on demand, as the case may be.

From the computational perspective, the next step is to work with symmetrized quantities in our implementation, such as Coulomb interaction, dielectric function, and polarizability. This measure would improve the numerical accuracy among degenerate states and speed up considerably our calculations by reducing the points in reciprocal space involved in the calculations. On top of the symmetrization, which would benefit the already parallelized structure over  $\mathbf{k}$ -points, we consider parallelizing the code for the integration in the correlation self-energy. In this way, every frequency

---

point would correspond to a MPI process.

Finally, we address the faults in the predictions of the electronic structure. Although our results are in good agreement with the literature, the bandgaps are overestimated compared to experiment. As exposed in Sec. 7.3, there are three main reasons for the overestimated fundamental bandgaps. Preferably, the corrections to the zero-point renormalization could be calculated with **exciting**, at the degree of theory suitable for each case; it may be DFT or MBPT, depending on the material. This way, we could bypass the discrepancies among published corrections. As well, for future improvements on our implementation, the electron-phonon coupling can be integrated in the optimized Hamiltonian, either as a final or an iterative correction.

The current QSGW implementation in **exciting** is designed to unite all the features of the code, so that the secular equation in the self-consistent scheme can gather contributions from other parts of the code. This applies for the addition of an exchange-correlation kernel to the polarizability operator in QSGW. This can be done in **exciting** using the exchange-correlation kernel implemented in the code, modified as proposed by Chen or Shishkin [111, 112]. This last possibility offers a cure for the lack of vertex corrections, which play an important role in results concerning polar compounds. Analogous, spin-orbit coupling, which translates into an extra term in the Hamiltonian, namely the spin-orbit operator, can be included in future QSGW calculations, either perturbatively or iteratively. In order to include spin-orbit coupling in **exciting**, we solve the second-variational secular equation, as explained by Gulans and coworkers [58]. A clear outlook to our current QSGW implementation is to perform this calculation on top of the optimized Hamiltonian.

The QSGW implementation in **exciting** is not a separated tool working with additional scripts: it is nested in the basic structure of the code. Therefore, eigenvectors are written as usual output files, and all features in **exciting** may use them as input for post-processing or as starting points for other calculations. For the case of external post-processing analysis, alternative interpolation schemes may be tested, specially for effective masses where the dispersion curve is non-parabolic. To account for excitonic effects, the BSE, already available in **exciting** [132], can be applied on top of the converged wavefunctions and energies in QSGW.

Regarding the analysis of wavefunctions, we can gain new information by looking at the overlap between LDA and QSGW eigenvectors at other  $\mathbf{k}$ -points besides  $\Gamma$ . A, perhaps, better assessment of bonds and hybridization can be reached by looking and comparing wavefunctions from the full and diagonal self-energy, to study the effect of band mixing.

The natural outlook of this project is to calculate the electronic structure of complex materials. For surfaces and interfaces, this goal will be reached in the near future by optimizing the current implementation as suggested above. Besides symmetrization and parallelization, the code may gain efficiency from better practices for memory allocation. For more complex crystalline solids, the present QSGW implementation in **exciting** is up to the challenge and ready for use.

On a final note, we conclude that the present research has contributed to understanding the impact of the QSGW method on the calculated electronic structure of solids using an all-electron basis set. The electronic structures presented here show considerable improvement relative to their LDA counterpart. Compared to  $G_0W_0$ , the QSGW method cures the starting-point dependence, and it also provides quasiparticle wavefunctions. In this PhD project, we have added new results to calculations on electronic structure by means of the QSGW method within the LAPW framework, an approach, which despite being less represented in literature, is very promising.





# Appendices



# Appendix A

## The Variational Method

The time-independent Schrödinger equation in Dirac's notation,  $\hat{H}|\Phi\rangle = E|\Phi\rangle$ , has infinite solutions, which we label with a greek letter. The eigenvectors are orthonormal and, assuming they form a complete set, we employ them as a basis set. The matrix elements of  $H$  in this basis are  $\langle\Phi_\beta|\hat{H}|\Phi_\alpha\rangle = E\delta_{\alpha\beta}$ . Any vector  $|\tilde{\Phi}\rangle$  sharing the same boundary conditions as the set  $\{\Phi_\alpha\}$  can be expressed as a linear combination of these eigenvectors,  $|\tilde{\Phi}\rangle = \sum_\alpha c_\alpha|\Phi_\alpha\rangle$ , with coefficients  $c_\alpha$ .

### A.1 Variational Principle

$|\tilde{\Phi}\rangle$  is the wavefunction of the many-body system, and as such is normalized:  $\langle\tilde{\Phi}|\tilde{\Phi}\rangle = 1$ . Inserting the completeness requirement,  $\sum_\alpha|\Phi_\alpha\rangle\langle\Phi_\alpha| = 1$  and, accounting for the orthonormality of the basis, we arrive at:

$$\langle\tilde{\Phi}|\tilde{\Phi}\rangle = \sum_{\alpha\beta}\langle\tilde{\Phi}|\Phi_\alpha\rangle\langle\Phi_\alpha|\Phi_\beta\rangle\langle\Phi_\beta|\tilde{\Phi}\rangle = \sum_{\alpha\beta}\langle\tilde{\Phi}|\Phi_\alpha\rangle\delta_{\alpha\beta}\langle\Phi_\beta|\tilde{\Phi}\rangle = \sum_\alpha|\langle\Phi_\alpha|\tilde{\Phi}\rangle|^2 = 1. \quad (\text{A.1})$$

We write  $E_0$  for the expectation value of the Hamiltonian with respect to the ground state. Unless the wavevector describes the groundstate, *i.e.*,  $|\tilde{\Phi}\rangle = |\tilde{\Phi}_0\rangle$  the expectation value of the Hamiltonian with respect to  $|\tilde{\Phi}\rangle$  will be higher than  $E_0$ .

$$\langle\tilde{\Phi}|\hat{H}|\tilde{\Phi}\rangle = \sum_{\alpha\beta}\langle\tilde{\Phi}|\Phi_\alpha\rangle\langle\Phi_\alpha|\hat{H}|\Phi_\beta\rangle\langle\Phi_\beta|\tilde{\Phi}\rangle = \sum_{\alpha\beta}\langle\tilde{\Phi}|\Phi_\alpha\rangle E\delta_{\alpha\beta}\langle\Phi_\beta|\tilde{\Phi}\rangle = \sum_\alpha E_\alpha|\langle\Phi_\alpha|\tilde{\Phi}\rangle|^2 \quad (\text{A.2})$$

Because  $E_\alpha \geq E_0$ , we can write  $\langle\tilde{\Phi}|\hat{H}|\tilde{\Phi}\rangle \geq \sum_\alpha E_0|\langle\Phi_\alpha|\tilde{\Phi}\rangle|^2 = E_0 \sum_\alpha|\langle\Phi_\alpha|\tilde{\Phi}\rangle|^2 = E_0$ . As long as  $|\tilde{\Phi}\rangle$  is an approximate solution to the ground state, the expectation value of the energy will be higher than true groundstate energy. The better the approximation, the closer it is to the true minimum energy. Provided the trial wavefunction  $|\tilde{\Phi}\rangle$  depends on known parameters, we can vary those to reach the minimum value of the Hamiltonian's expectation value.

### A.2 Linear Variational Problem

The set of parameters in the trial function  $|\tilde{\Phi}\rangle$  will necessarily enter the function  $\langle\tilde{\Phi}|\hat{H}|\tilde{\Phi}\rangle$ . The latter is a rather complicated function and impedes finding the set of parameters to minimize itself. Instead, we take a linear combination representation of the trial function with fix basis set of  $N$  functions and equal number of *variable* coefficients

$$|\tilde{\Phi}\rangle = \sum_i^N c_i|\Psi_i\rangle. \quad (\text{A.3})$$

We assume the basis functions are real and orthonormal. We normalize our trial function:

$$\langle \tilde{\Phi} | \tilde{\Phi} \rangle = \sum_{ij} c_i c_j \langle \Psi | \Psi \rangle = \sum_i c_i^2 = 1. \quad (\text{A.4})$$

With help of Lagrange's method of undetermined multipliers the problem reduces to a matrix diagonalization, restricting the search to suitable coefficients, rather than the whole set of parameters<sup>1</sup>. We organize the coefficients  $c_i$  in a vector  $\mathbf{c}$  and the eigenvalues in a diagonal matrix  $\mathbf{E}$ . Re-writing  $\hat{H}$  in its  $N \times N$  matrix representation  $\mathbf{H}$ —in the basis of  $\{|\Psi\rangle\}$ — and constructing a matrix  $\mathbf{C}$  with the vectors  $\mathbf{c}$  made up by the coefficients as columns, we arrive at the standard problem for the matrix  $\mathbf{H}$ :

$$\mathbf{HC} = \mathbf{CE}, \quad (\text{A.5})$$

which returns  $N$  orthonormal solutions. The lowest eigenvalue corresponds to the approximate solution to the real groundstate, with the remaining energy values representing upper bounds to the successive excited states.

---

<sup>1</sup>The proof can be find in ref. [23], pages 34-35

# Appendix B

## Second Quantization and Pictures in Quantum Mechanics

The theoretical representation of many-body systems in quantum field physics proves to be a useful framework for condensed matter as well. Therefore we make use of the notation found in this theory; namely the second quantization. In this appendix we briefly present the main concepts and terminology. Chapter 2 in Ref. [37] accounts for a detailed description of this formulation. This Appendix is restricted to half-spin, indistinguishable particles, *i.e.*, fermions.

### B.1 Fock Space

A single-particle state,  $|\alpha\rangle$ , has a distinctive set of quantum numbers. According to Pauli's principle, this state cannot be occupied by more than one particle at the time and are normalized such that  $\langle\alpha|\beta\rangle = \delta_{\alpha\beta}$ . For a particular state, there are  $N!$  physically equivalent ways to arrange the set of states,  $\{|\alpha_i\rangle, i = 1 \dots N\}$ . Working with such large determinants impedes calculating matrix elements of operators smoothly. It is convenient to change to occupation number representation, also known as *second quantization*. We change to a vector space, *Fock space*, which is the sum of the vacuum state,  $|0\rangle$ , the single-particle states  $\{|\alpha\rangle\}$ , and the complete set of antisymmetric states. Each single-particle state has an occupation number  $n$ , with value 0 or 1, so that a state  $|\alpha_i\rangle$  is represented also as  $|n_i\rangle$ . In Fock space, states with different occupation numbers are orthogonal.

### B.2 Creation and Annihilation Operators

Operators such as position or momentum operators act on a  $N$ -particle system to return a  $N$ -particle system. In order to move away from a space with fixed particle number, we introduce two operators: the creation  $a_i^\dagger$  and the annihilation  $a_i$  operators. The former creates a particle in state  $|\alpha_i\rangle$  and the latter, its adjoint, removes a particle in this state. On acting on a  $N$ -particles system, these operators return an antisymmetric  $N\pm 1$ -particles state. The most important relations are:

$$a_i^\dagger |n_1 \dots, n_i, \dots\rangle = \begin{cases} (-1)^{S_i} |n_1 \dots, n_i + 1, \dots\rangle, & n_i = 0 \\ 0, & n_i = 1 \end{cases} \quad (\text{B.1})$$

$$a_i |n_1 \dots, n_i, \dots\rangle = \begin{cases} (-1)^{S_i} |n_1 \dots, n_i - 1, \dots\rangle, & n_i = 1 \\ 0, & n_i = 0 \end{cases} \quad (\text{B.2})$$

$S_i$  is equal to  $\sum n_j$ , with  $j = 1, \dots, i - 1$ . This makes the prefactor take the appropriate sign whenever there is an exchange of operators by bringing  $a_i$  or  $a_i^\dagger$  to position  $i$ . The action of the annihilation operator on an empty state renders zero. Likewise, the creation of an electron on an occupied state gives zero, thus respecting Pauli's principle. In line with this principle, if the creation operator acts twice on the same state returns zero. The order in which these operators appear plays

an important role, giving rise to the following anticommutation rules:

$$\{a_i, a_j\} = 0, \quad \{a_i^\dagger, a_j^\dagger\} = 0, \quad \{a_i, a_j^\dagger\} = \delta_{ij}. \quad (\text{B.3})$$

From these anticommutation rules, we define the particle number operator, which by acting on the total state returns the number of particles occupying a particular state:

$$\hat{n}_i |n_1 \dots n_i \dots\rangle = a_i^\dagger a_i |n_1 \dots, n_i, \dots\rangle = n_i |n_1 \dots, n_i, \dots\rangle \quad (\text{B.4})$$

$$\sum_i n_i = N \quad (\text{B.5})$$

## Field operators

Alternatively, second quantization creation and annihilation operators can be recast into other operators with the same properties. These are called creation field operator  $\hat{\psi}^\dagger(\mathbf{r})$  and annihilation field operator  $\hat{\psi}(\mathbf{r})$ , which create and annihilate respectively a particle at position  $\mathbf{r}$ . Using a complete basis set  $\{\psi_i\}$ , we can construct a linear combination with the annihilation and creation operators:

$$\hat{\psi}^\dagger(\mathbf{r}) = \sum_i \psi_i^\dagger(\mathbf{r}) a_i^\dagger, \quad (\text{B.6})$$

$$\hat{\psi}(\mathbf{r}) = \sum_i \psi_i(\mathbf{r}) a_i \quad (\text{B.7})$$

The complete basis is the independent-particle states,  $\{\psi_i(\mathbf{r})\}$ , where  $i = 1 \dots N$ , being formally  $N = \infty$ . To differentiate these operators from wavefunctions, we mark them with a hat everywhere in this thesis. For these operators, it yields the following anticommutation rules:

$$\{\hat{\psi}(\mathbf{r}), \hat{\psi}(\mathbf{r}')\} = 0, \quad \{\hat{\psi}^\dagger(\mathbf{r}), \hat{\psi}^\dagger(\mathbf{r}')\} = 0, \quad \{\hat{\psi}(\mathbf{r}), \hat{\psi}^\dagger(\mathbf{r}')\} = \delta(\mathbf{r} - \mathbf{r}') \quad (\text{B.8})$$

## B.3 Schrödinger Picture

In the Schrödinger picture, the state,  $|\alpha(t)\rangle$  carries the time-dependence. The states in this reference frame obey the time-dependent Schrödinger equation:

$$i\hbar \frac{\partial}{\partial t} |\alpha(t)\rangle = \hat{H} |\alpha(t)\rangle, \quad (\text{B.9})$$

where  $\hat{H}$  may or may not include a time-dependent potential, otherwise only the state holds the time-dependency. If the wavefunction of the system at any initial time  $t_0$  is known, we can deduce the later state of the system using the evolution operator in the Schrödinger picture,  $U_S$ :

$$|\alpha(t)\rangle = U_S(t, t_0) |\alpha(t_0)\rangle \quad (\text{B.10})$$

$$U_S(t, t_0) = e^{-i \int_{t_0}^t \hat{H}(t') dt' / \hbar} \quad (\text{B.11})$$

$$U_S(t - t_0) = e^{-i(t-t_0)\hat{H}/\hbar} \quad (\text{B.12})$$

Equation B.11 equals Eq. B.12 if  $\hat{H}$  is time-independent. An important property of the evolution operator is that it is unitary, and its action on a state corresponds to a unitary transformation. Also,

$U_S(t_0, t_0) = I$ , where  $I$  is the identity matrix, and  $U_S(t, t_0) = U_S^\dagger(t_0, t)$ .

## B.4 Heisenberg Picture

In the Heisenberg picture the states are static, also equal to a state in the Schrödinger picture at a time  $t_\alpha$ , which we set to 0. The time-dependence in this reference frame is entirely upon the operators. Operators and states in this picture are labeled with a subscript  $H$ . States in this representation relate to those in the Schrödinger picture by:

$$|\alpha_H(t)\rangle = e^{-i\hat{H}t}|\alpha(t)\rangle = e^{-i\hat{H}t}U_S(t-0)|\alpha\rangle = |\alpha\rangle, \quad (\text{B.13})$$

confirming the time-independence of the states in the Heisenberg picture. An operator in the Heisenberg picture,  $\hat{O}_H$ , relates to the static operator in the Schrödinger picture as:

$$\hat{O}_H(t) = e^{i\hat{H}t/\hbar}\hat{O}_S e^{-i\hat{H}t/\hbar}, \quad (\text{B.14})$$

which inserted in the equation of motion returns:

$$i\hbar \frac{\partial}{\partial t} \hat{O}_H = i\hbar \left[ \frac{\partial}{\partial t} e^{i\hat{H}t/\hbar} \right] \hat{O}_S e^{-i\hat{H}t} + i\hbar e^{i\hat{H}t/\hbar} \hat{O}_S \left[ \frac{\partial}{\partial t} e^{-i\hat{H}t/\hbar} \right] = [\hat{O}_H, \hat{H}] = e^{i\hat{H}t/\hbar} [\hat{O}_S, \hat{H}] e^{-i\hat{H}t/\hbar}, \quad (\text{B.15})$$

which confirms that if  $\hat{O}_S$  and  $\hat{H}$  commute, then  $\hat{O}_H$  reduces to a constant of motion. Specially important in Chapter 3, the field operators in the Heisenberg picture relate to their definition in Schrödinger picture in appendix B.2:

$$\hat{\psi}(\mathbf{r}, t) = U_S^\dagger(t)\hat{\psi}(\mathbf{r})U_S(t) \quad , \quad \hat{\psi}^\dagger(\mathbf{r}, t) = U_S^\dagger(t)\hat{\psi}^\dagger(\mathbf{r})U_S(t) \quad (\text{B.16})$$

Because the time argument distinguishes the Heisenberg picture from the Schrödinger picture, we leave out the subscript  $H$  for field operators.

## B.5 Interaction Picture

Also known as Dirac picture, this framework is particularly useful when the Hamiltonian is divided in two parts:  $\hat{H} = \hat{H}_0 + \hat{V}$ , with  $\hat{H}_0$  a time-independent, non-interacting Hamiltonian and  $\hat{V}$  the interaction among particles, where generally both operators do not commute and the order of appearance is important. A usual choice of  $\hat{H}_0$  is an independent-particle Hamiltonian, such as the Kohn-Sham Hamiltonian, and the interaction  $\hat{V}$  in the electronic calculation cases is the full Coulomb potential. Time-dependency in this picture falls on both wavefunctions and operators, marked with subscript  $I$ . The state of the system in the interaction picture relates to  $\hat{H}_0$  and the state in the Schrödinger picture, it reads:

$$|\alpha_I(t)\rangle = e^{i\hat{H}_0 t/\hbar}|\alpha(t)\rangle. \quad (\text{B.17})$$

We insert this state in the equation of motion, and using the result of Eq. B.9, we arrive at:

$$i\hbar \frac{\partial}{\partial t} |\alpha_I(t)\rangle = \hat{V}(t)|\alpha_I(t)\rangle. \quad (\text{B.18})$$

Because  $|\alpha_I(t)\rangle$  evolves according to the action of the evolution operator in this picture, and comparing it with equation Eq. B.17, we define the evolution operator and its equation of motion in the interaction picture:

$$|\alpha_I(t)\rangle = \hat{U}_I(t, t_0)|\alpha_I(t_0)\rangle = e^{i\hat{H}_0 t/\hbar} e^{-i\hat{H}(t-t_0)/\hbar} e^{i\hat{H}_0 t_0/\hbar} |\alpha_I(t_0)\rangle \quad (\text{B.19})$$

$$i\hbar \frac{\partial}{\partial t} \hat{U}_I(t, t_0) = \hat{V}(t) \hat{U}_I(t, t_0) \quad (\text{B.20})$$

$$\hat{U}_I(t, t_0) - \hat{U}_I(t_0, t_0) = -\frac{i}{\hbar} \int_{t_0}^t \hat{V}(t') \hat{U}_I(t', t_0) dt' \quad (\text{B.21})$$

From the evolution of the state, we see that  $\hat{U}_I(t_0, t_0) = 1$ . Together with this property, and by iterating  $\hat{U}_I$  in Eq. B.21, we write the expansion of the evolution operator. To keep the right order of the operators in the expansion, we make use of the time-order operator,  $T$ :

$$\hat{U}_I(t, t_0) = 1 + \left(\frac{i}{\hbar}\right) \int_{t_0}^t \hat{V}(t') dt' + \left(\frac{i}{\hbar}\right)^2 \int_{t_0}^t \int_{t_0}^{t'} \hat{V}(t') \hat{V}(t'') dt' dt'' + \dots \quad (\text{B.22})$$

$$= \sum_{n=0}^{\infty} \left(\frac{i}{\hbar}\right)^n \int_{t_0}^t \int_{t_0}^{t_1} \dots \int_{t_0}^{t_n} \hat{V}(t_1) \hat{V}(t_2) \dots \hat{V}(t_n) dt_1 dt_2 \dots dt_n \quad (\text{B.23})$$

$$= \sum_{n=0}^{\infty} \left(\frac{i}{\hbar}\right)^n \frac{1}{n!} \int_{t_0}^t dt_1 \int_{t_0}^{t_1} dt_2 \dots \int_{t_0}^{t_n} dt_n T [\hat{V}(t_1) \hat{V}(t_2) \dots \hat{V}(t_n)] \quad (\text{B.24})$$

$$= T \left[ e^{\frac{-i}{\hbar} \int_{t_0}^t \hat{V}(t') dt'} \right] \quad (\text{B.25})$$

The first line in the expansion is the direct iteration of Eq. B.21, then the sum in the second line arises from the term by term summation of the expansion. The prefactor in the third line above is due to the number of possibilities how to arrange the operators and the integration variables (see page 57 in Ref. [38] or appendix A in Ref. [37]). Finally, the power-series expansion gives a compact version of the evolution operator. This last form is used in the diagrammatic expansion of  $G$  in Sec. 3.3.1.

## Appendix C

### Spherical Harmonics

This project employs spherical harmonics functions for the (L)APW+LO method, as well as for the construction of mixed basis set in the QSGW implementation and the Laplacian expansion of the Coulomb interaction. The definition of this function in spherical coordinates is:

$$Y_l^{|m|}(\theta, \phi) = (-1)^m \sqrt{\frac{2l+1}{4\pi}} \sqrt{\frac{(l-|m|)!}{(l+|m|)!}} P_l^{|m|}(\cos\theta) e^{im\phi}, \quad \begin{cases} l = 1, 2, \dots \\ m = -l, \dots, 0, \dots, l. \end{cases} \quad (\text{C.1})$$

where  $P_l^{|m|}(\cos\theta)$  is the Legendre polynomial. Two important relations are: the complex conjugated  $Y_l^{-m}(\theta, \phi) = (-1)^m [Y_l^m(\theta, \phi)]^*$  and the inverse  $Y_l^m(\hat{\mathbf{r}}') = (-1)^l Y_l^m(-\hat{\mathbf{r}}')$ . The Rayleigh equation defines a plane wave at a position  $\mathbf{r}$  an expansion about a vector  $\mathbf{r}_\alpha$  into spherical harmonics:

$$e^{i\mathbf{k}\cdot\mathbf{r}} = e^{i\mathbf{k}\cdot\mathbf{r}_\alpha} 4\pi \sum_{l=1}^{\infty} \sum_{m=l}^{-l} i^l j_l(kr') Y_l^{|m|}(\theta, \phi) Y_l^{|m|}(\theta_i, \phi_i) = e^{i\mathbf{k}\cdot\mathbf{r}_\alpha} 4\pi \sum_{l=1}^{\infty} \sum_{m=l}^{-l} i^l j_l(kr') Y_l^{|m|}(\hat{\mathbf{r}}') Y_l^{|m|}(\hat{\mathbf{k}}), \quad (\text{C.2})$$

with  $\mathbf{r}' = \mathbf{r} - \mathbf{r}_\alpha$  and  $r' = |\mathbf{r} - \mathbf{r}_\alpha|$ . The  $j_l$  is the Bessel function, and the  $\hat{\mathbf{k}}$  and  $\hat{\mathbf{r}}'$  are unitary vectors in the direction of  $\mathbf{k}$  and  $\mathbf{r}'$ , respectively. These directions are also given by angles  $\theta_i$ ,  $\phi_i$  and  $\theta$ ,  $\phi$ , respectively. A useful relation is the product of two spherical harmonics:

$$Y_l^m(\hat{\mathbf{r}}) Y_{l'}^{m'}(\hat{\mathbf{r}}) = \sum_{L=|l-l'|}^{l+l'} \sum_{M=-L}^L \mathcal{G}_{l_1 m_1; l_2 m_2}^{lm} Y_L^M(\hat{\mathbf{r}}), \quad (\text{C.3})$$

The Gaunt's coefficients  $\mathcal{G}$ , examined in Ref. [133], define the integral over three spherical harmonics:

$$\mathcal{G}_{l_1 m_1; l_2 m_2}^{lm} = \int Y_l^m(\hat{\mathbf{r}}) Y_{l'}^{m'}(\hat{\mathbf{r}}) Y_L^M(\hat{\mathbf{r}}) d(\hat{\mathbf{r}}) \quad (\text{C.4})$$

The addition theorem, or expansion theorem, can be combined with the previous properties of spherical harmonics to return:<sup>1</sup>

$$\frac{4\pi}{2L'+1} \frac{1}{|\mathbf{r}_1 - \mathbf{r}_2|^{L'+1}} Y_{L'}^{M'}(\hat{\mathbf{e}}_{\mathbf{r}_1 - \mathbf{r}_2}) = (-1)^{L'+M} \sum_{l=0}^{\infty} \sum_{m=-l}^l C_{L'l}^{M'm} \frac{r_1^l}{r_2^{L'+l+1}} Y_l^m(\hat{\mathbf{r}}_1) \left[ Y_{L'+l}^{m-M'}(\hat{\mathbf{r}}_2) \right]^*, \quad (\text{C.5})$$

$$C_{L'l}^{M'm} = (4\pi)^{3/2} \frac{1}{\sqrt{(2L'+1)(2l+1)[2(L'+1)+1]}} \sqrt{\frac{(L'+l+m-M')!(L'+l-m+M')!}{(L'+M')!(L'-M')!(l+m)!(l-m)!}}. \quad (\text{C.6})$$

<sup>1</sup>An easy version of its derivation is in Ref.[134]. Being  $\gamma$  the angle between  $\Omega_1$  and  $\Omega_2$ , then:

$$P_l^{m=0}(\cos\gamma) = \frac{4\pi}{2l+1} \sum_m [Y_l^m(\Omega_1)]^* Y_l^m(\Omega_2)$$

## Appendix E

# Pade's Approximants

The idea behind the Pade's Approximants is to match the Taylor series expansion of a particular function as far (in number of terms) as possible [135]. For that purpose, we approximate the value of a function to a rational fraction. Henri Pade defined the approximants  $L, M$  as approximants to a function  $A(x)$  of the form:

$$[L/M] = P_L(x)/Q_M(x) \quad (\text{E.1})$$

where  $P_L(x)$  is a polynomial of degree at most  $L$  and  $Q_M(x)$  is a polynomial of degree at most  $M$  [136]. The polynomial in the denominator is subject to the normalization condition  $Q_M(0) = 1$ . For a given set,  $\{z_i\}$ , of  $n$  points in the complex plane, there is a series expansion of a function associated with each point in the set. The representation of the function for a complex point  $z_i$  is:

$$\sum_{j=0}^{m_i-1} u_{ij}(z - z_i)^j + O[(z - z_i)^{m_i}]. \quad (\text{E.2})$$

For the fitting of a function with these characteristics, we search for a rational fraction  $P_L(z)/Q_M(z)$ . The degrees of the numerator and the denominator satisfy:

$$L + M = n = \sum_{i=1}^n m_i - 1 \quad (\text{E.3})$$

To fit a rational fraction to a set of function values, we use the Thiele's reciprocal difference method [137]. Following this scheme, we get a fraction-type expansion of a function  $\Sigma$ :

$$\Sigma(z) = \frac{a_0}{1 + \frac{(z-z_0)a_1}{1 + \frac{(z-z_1)a_2}{\ddots \frac{(z-z_{n-1})a_n}{1 + \frac{(z-z_n)a_{n+1}}{g_{n+1}(z)}}}}}, \quad (\text{E.4})$$

where  $\Sigma(z_0) = a_0$ . For the values at the points to be fitted, we define:

$$g_0(z) = \Sigma(z) \quad , \quad g_n(z) = \frac{g_{n-1}(z_{n-1}) - g_{n-1}(z)}{(z - z_{n-1})g_{n-1}(z)}, \quad (\text{E.5})$$

with  $n \geq 2$ . We find  $a_n = g_n(z_n)$  given by the recursion above.  $\Sigma$  is then generated for a fit on  $n$  points by means of the following recursion formulas, where  $P = A$  and  $Q = B$  are of orders  $L = (n - 2)/2$  and  $M = n/2$ , respectively:

$$\Sigma_n = \frac{A_n}{B_n} \quad , \quad \frac{A_{n+1}}{B_{n+1}} = \frac{A_n + (z - z_n)a_{n+1}A_{n-1}}{B_n + (z - z_n)a_{n+1}B_{n-1}}, \quad (\text{E.6})$$

with  $A_{-1} = 0$ ,  $B_{-1} = 1$ ,  $A_0 = a_0$  and  $B_0 = 1$ .

# List of Tables

6.1	Most important equations for the three blocks constituting the $v_{ij}$ matrix. . . . .	58
6.2	Computational requirements for QSGW calculations in the case of BN. For the matrix elements in the correlation self-energy, saved as complex numbers—they count as double floating points— each entry takes up 16 bytes of memory. . . . .	65
7.1	Selected materials together with their structure types and lattice parameters, $a$ , and the corresponding input parameters that enter the calculations. Here we use the abbreviation $RGK$ for $R_{MT} \mathbf{G} + \mathbf{k} _{max}$ . . . . .	68
7.2	Total number of local orbitals per unit cell for each material considered in this work.	70
7.3	Configuration of LOs in GaAs for the first three $l$ -channels. For each atom, in the left column there is the set-up of the LOs and at the right the linearization energy value $E_{nl}$ (Ha) for state $n$ and angular momentum $l$ . . . . .	70
7.4	Energy gaps, $E_{\Delta}$ (eV), at $\Gamma$ -point, and between $\Gamma$ (VBM) and $X$ (CBM) for the selected materials. For Si and C, the fundamental bandgap, $E_g$ , is indirect with the CBM between $\Gamma$ and $X$ and values are provided separately. In the last row, the experimental values are corrected for zero-point renormalization and spin-orbit coupling, unless noted by a subscript $e$ . The experimental bandgap of Ar and the corrected experimental values are taken from Ref. [95], with the exception of GaAs [12]. The experimental values for BN and CaO are taken from Ref. [96, 97], respectively. .	71
7.5	Effective masses in the $\Gamma - X$ direction for diamond and BN employing the full self-energy matrix (first column) and diagonal self-energy matrix (second column), in units of the free electron mass $m_o$ . References to experimental [120, 121] and theoretical [118, 122, 123] data are given in the last column. . . . .	83
7.6	$E_{\Delta}$ (eV) at high-symmetry points for C, SiC, and Ar together with the number of iterations till convergence. As reference, the two last columns show the results of the $G_0W_0$ calculations on top of LDA and PBE0 results, taken from Ref. [95]. . . . .	84

# List of Figures

2.1	Time-line of selected contributions to quantum calculations. . . . .	18
3.1	The diagram at the right represents the right-hand side of the Dyson equation for $G$ (black propagation line). $G_0$ is the grey propagation line and $\Sigma$ is the dark circle. Analogous, the diagram at the left corresponds to the rhs of the Dyson equation for $W$ (wiggly line). $v$ is the dashed line and $P$ is represented by the dark ellipse. . . . .	34
5.1	3D representation of space partition of the unit cell in the APW method. Spherical coordinates define angles between arbitrary position vector $\mathbf{r}$ (green) and $x$ -axis (black). In red, $\mathbf{r}_\alpha$ is the position vector of the center of the nucleus, $\mathbf{R}_{MT}$ is the MT radius. Positions in space are saved in a grid within the MT. . . . .	46
6.1	Flowchart of the QSGW implementation in <b>exciting</b> . The starting point is the independent particle Hamiltonian $H_0$ . In the first iteration, which is not explicitly included in the figure, exchange-correlation potential and the resulting output $\{\psi_{m\mathbf{k}}^{\text{IP}}(\mathbf{r}), \epsilon_{m\mathbf{k}}^{\text{IP}}\}$ correspond to an IP scheme. The optimized potential in the violet block, defined in Eq. 4.2, is the central quantity in the QSGW method. . . . .	56
7.1	Convergence of the bandgap energy (solid line), and the band energies of the VBM (dotted dashed line) and of the CBM (dashed line) for the QSGW calculations. The first iteration corresponds to the initial KS calculation and is not shown in the plots. . . . .	69
7.2	Bandstructure (left) and DOS diagram (right) of SiC, Si, BN, Diamond, GaAs, MgO, CaO, LiF, and Ar. The blue curves correspond to the QSGW results and the green curves correspond to the LDA results. In the DOS diagrams, the red curve corresponds to the $G_0W_0$ results. . . . .	75
7.3	Bandstructures of Ar, SiC, BN, and diamond by means of QSGW employing the diagonal self-energy matrix (dashed line) and the full self-energy matrix (solid line). . . . .	81
7.4	Calculated bandstructure of solid argon with QSGW@LDA (solid blue line), QSGW@HF (purple circles), and QSGW@PBE0 (pink diamonds). . . . .	84
7.5	Charge-density differences between QSGW and LDA calculations for LiF. Positive difference is blue, and negative is red. Yellow spheres depict fluorine, while green spheres represent lithium atoms. . . . .	86
7.6	Charge-density difference plot for CaO. The center atom, in white, is oxygen. Orange spheres depict the calcium atoms, positioned at the corners of the unit cell. . . . .	87
7.7	The figure shows the isosurface (blue) of the squared norm of the LDA-WF (left) and QP-WF (right) at $\Gamma$ for the first conduction band in MgO. The isovalue has been chosen as $3 \cdot 10^{-4} e/\text{bohr}^3$ . Brown spheres at the corners depict the magnesium atoms, and the red sphere at the center represents oxygen. . . . .	88
7.8	The figure shows the isosurface of the squared norm of the $p$ -orbital state in LDA (right) and in QSGW (left) at $\Gamma$ for the highest occupied band in MgO. The isovalue has been chosen as $1 \cdot 10^{-3} e/\text{bohr}^3$ . Different rotations in space of the unit cell with respect to Fig. 7.7 are meant to facilitate visual comparison. Color code like in Fig. 7.7. . . . .	88

- 7.9 The figure shows the isosurface of the squared norms of the of the three degenerate LDA-WFs (left) and QP-WFs (right) at  $\Gamma$  for the highest occupied band in MgO. The isovalue has been chosen as  $5 \cdot 10^{-3} e/\text{bohr}^3$ . Color code like in Fig. 7.7. The spheres depicting atoms have reduced radii compared to the last figure. . . . . 89
- 7.10 The figure shows the isosurface of the squared norms of the of the three degenerate LDA-WFs (right) and QP-WFs (left) at  $\Gamma$  for the highest occupied band in MgO. The isovalue has been chosen as  $1 \cdot 10^{-6} e/\text{bohr}^3$ . Color code like in Fig. 7.7. . . . . 89

# Bibliography

- [1] M. Born and R. Oppenheimer, *Ann. Physik* **84**, 457 (1927).
- [2] P. Hohenberg and W. Kohn, *Phys. Rev.* **136**, B864 (1964).
- [3] E. Eberhard and R. Dreizler, *Density functional theory : an advanced course*, Springer, Heidelberg [u.a.], 2011.
- [4] J. P. Perdew and S. Kurth, *A Primer in Density Functional Theory*, Springer, Berlin, 2003.
- [5] L. Hedin, *Phys. Rev.* **139**, A796 (1965).
- [6] W. G. Aulbur, L. Jonsson, and J. W. Wilkins, *Solid State Physics* **54**, 1 (2000).
- [7] M. S. Hybertsen and S. G. Louie, *Phys. Rev. B* **34**, 5390 (1986).
- [8] G. Onida, L. Reining, and A. Rubio, *Rev. Mod. Phys.* **74**, 601 (2002).
- [9] F. Aryasetiawan and O. Gunnarsson, *Rep. Prog. Phys.* **61**, 237 (1998).
- [10] M. van Schilfgaarde, T. Kotani, and S. Faleev, *Phys. Rev. Lett.* **96**, 226402 (2006).
- [11] S. V. Faleev, M. van Schilfgaarde, and T. Kotani, *Phys. Rev. Lett.* **93**, 126406 (2004).
- [12] T. Kotani, M. van Schilfgaarde, and S. V. Faleev, *Phys. Rev. B* **76**, 165106 (2007).
- [13] E. Schrödinger, *Ann. der Phys.* **384**, 489 (1926).
- [14] K. Capelle, *Braz. J. Phys.* **36**, 1318 (2006).
- [15] O. R. N. Laboratory, Oak Ridge Leadership Computing Facility *Summit*, 2018, <https://www.olcf.ornl.gov/summit/>.
- [16] F. Giustino, *Materials Modelling using Density Functional Theory*, Oxford University Press, 2014.
- [17] E. Engel and R. M. Dreizler, *Density Functional Theory: An Advanced Course (Theoretical and Mathematical Physics)*, Springer, 2011.
- [18] R. M. Martin, *Electronic Structure: Basic Theory and Practical Methods*, Cambridge University Press, 2008.
- [19] D. R. Hartree, *Math. Proc. Camb. Philos. Soc.* **24**, 89 (1928).
- [20] F. Bloch, *Z. für Physik* **52**, 555 (1929).
- [21] J. C. Slater, *Phys. Rev.* **34**, 1293 (1929).
- [22] V. Fock, *Z. für Physik* **61**, 126 (1930).
- [23] A. Szabo and N. S. Ostlund, Dover Publications, New York, USA, 1996.
- [24] L. H. Thomas, *Proc. Camb. Phil. Soc.* **23**, 542 (1926).
- [25] E. Fermi, *Z. Phys.* **48**, 73 (1928).
- [26] W. Kohn and L. J. Sham, *Phys. Rev.* **140**, A1133 (1965).

- [27] J. P. Perdew and K. Schmidt, AIP Conference Proceedings **577**, 1 (2001).
- [28] J. P. Perdew, K. Burke, and M. Ernzerhof, Phys. Rev. Lett. **77**, 3865 (1996).
- [29] C. Adamo and V. Barone, J. Chem. Phys. **110**, 6158 (1999).
- [30] A. M. Zagoskin, *Quantum theory of many-body systems : techniques and applications*, Graduate texts in physics, Springer, Cham [u.a.], 2. ed. edition, 2014.
- [31] D. Pines and P. Nozières, *The Theory of Quantum Liquids. Volume 1*, W. A. Benjamin, Inc., New York, 1966.
- [32] L. D. Landau, Soviet Physics JETP **3**, 920 (1957).
- [33] V. P. Slin, Soviet Physics JETP **6**, 920 (1958).
- [34] J. M. Luttinger and J. C. Ward, Phys. Rev. **118**, 1417 (1960).
- [35] E. N. Economou, *Green's functions in quantum physics*, Springer, Berlin [u.a.], 3. ed. edition, 2006.
- [36] R. M. Martin, L. Reining, and D. M. Ceperley, *Interacting electrons: theory and computational approaches*, Cambridge University Press, Cambridge, 2016.
- [37] W. H. Dickhoff and D. Van Neck, *Many-Body Theory Exposed! : Propagator Description of Quantum Mechanics in Many-Body Systems*, World Scientific Publishing Company, 2nd edition, 2008.
- [38] A. L. Fetter and H. D. Walecka, *Quantum Theory of Many-Particle Systems*, McGraw-Hill, 1971.
- [39] J. Hubbard, Proceedings of the Royal Society of London A: Mathematical, Physical and Engineering Sciences **240**, 539 (1957).
- [40] G. W. Pratt, Phys. Rev. **118**, 462 (1960).
- [41] J. Grotendorst, S. Blügel, and D. Marx, editors, *Computational Nanoscience: Do It Yourself!*, volume 31, FZJ, John von Neumann Institute for Computing, Jülich, 2006, Record converted from VDB: 12.11.2012.
- [42] D. Bohm and D. Pines, Phys. Rev. **82**, 625 (1951).
- [43] D. Pines and D. Bohm, Phys. Rev. **85**, 338 (1952).
- [44] D. Bohm and D. Pines, Phys. Rev. **92**, 609 (1953).
- [45] D. Pines, Phys. Rev. **92**, 626 (1953).
- [46] M. van Schilfgaarde, T. Kotani, and S. V. Faleev, Phys. Rev. B **74**, 245125 (2006).
- [47] F. Bruneval, N. Vast, and L. Reining, Phys. Rev. B **74**, 045102 (2006).
- [48] D. Tamme, R. Schepe, and K. Henneberger, Phys. Rev. Lett. **83**, 241 (1999).
- [49] B. Holm and U. von Barth, Phys. Rev. B **57**, 2108 (1998).
- [50] S. Ismail-Beigi, J. Phys.: Cond. Matter **29** (2017).
- [51] S. Ismail-Beigi, *Justifying quasiparticle self-consistent schemes via gradient optimization in Luttinger-Ward theory*, 2014, arXiv:1406.0772[cond-mat.mtrl-sci].
- [52] S. Ismail-Beigi, Phys. Rev. B **81**, 195126 (2010).

- 
- [53] J. C. Slater, Phys. Rev. **51**, 846 (1937).
- [54] S. Cottenier, *Density Functional Theory and the family of (L)APW methods: a step-by-step introduction*, 2nd edition, 2013.
- [55] D. J. Singh, *Planewaves, Pseudopotentials, and the LAPW Method*, Springer, New York, 2nd. edition, 2006.
- [56] O. K. Andersen, Phys. Rev. B **12**, 3060 (1975).
- [57] O. Andersen, Solid State Commun. **13**, 133 (1973).
- [58] A. Gulans et al., J. Phys.: Condens. Matter **26**, 363202 (2014).
- [59] C. Ambrosch-Draxl, Physica Scripta **2004**, 48 (2004).
- [60] D. Singh, Phys. Rev. B **43**, 6388 (1991).
- [61] E. Sjöstedt, L. Nordström, and D. J. Singh, Solid State Comm. **114**, 15 (2000).
- [62] F. Aryasetiawan and O. Gunnarsson, Phys. Rev. B **49**, 16214 (1994).
- [63] T. Kotani and M. van Schilfgaarde, Solid State Commun. **121**, 461 (2002).
- [64] H. Jiang et al., Comp. Phys. Commun. **184**, 348 (2013).
- [65] X. Li, *All-electron  $G_0W_0$  code based on FP-(L)APW+lo and applications*, PhD thesis, Free University, 2008.
- [66] C. Friedrich, A. Schindlmayr, and S. Blügel, Comp. Phys. Comm. **180**, 347 (2009).
- [67] C. Ambrosch-Draxl and J. O. Sofo, Comp. Phys. Commun. **175**, 1 (2006).
- [68] M. Betzinger, C. Friedrich, and S. Blügel, Phys. Rev. B **81**, 195117 (2010).
- [69] F. Liu et al., J. Comp. Physics **286**, 1 (2015).
- [70] B. Farid, R. Daling, D. Lenstra, and W. van Haeringen, Phys. Rev. B **38**, 7530 (1988).
- [71] S. Lebègue, B. Arnaud, M. Alouani, and P. E. Bloechl, Phys. Rev. B **67**, 155208 (2003).
- [72] R. W. Godby, M. Schlüter, and L. J. Sham, Phys. Rev. Lett. **56**, 2415 (1986).
- [73] R. W. Godby, M. Schlüter, and L. J. Sham, Phys. Rev. B **37**, 10159 (1988).
- [74] G. Baym and L. P. Kadanoff, Phys. Rev. **124**, 287 (1961).
- [75] V. Anisimov, *Strong Coulomb Correlations in Electronic Structure Calculations*, Advances in Condensed Matter Science, Taylor & Francis, 2000.
- [76] W. H. Press, B. P. Flannery, S. A. Teukolsky, and W. T. Vetterling, *Numerical Recipes in Fortran 77*, Cambridge Univ. Press, 2005.
- [77] S. Massidda, M. Posternak, and A. Baldereschi, Phys. Rev. B **48**, 5058 (1993).
- [78] D. Deguchi, K. Sato, H. Kino, and T. Kotani, Jpn. J. Appl. Phys. **55**, 051201 (2016).
- [79] F. Kaplan, F. Weigend, F. Evers, and M. J. van Setten, J. Chem. Theory Comput. **11**, 5152 (2015).
- [80] V. N. Staroverov, G. E. Scuseria, J. Tao, and J. P. Perdew, Phys. Rev. B **69**, 075102 (2004).
- [81] C. R. Hubbard, H. E. Swanson, and F. A. Mauer, J. Appl. Crystallogr. **8**, 45 (1975).

- [82] M. Shishkin and G. Kresse, *Phys. Rev. B* **75**, 235102 (2007).
- [83] A. Grüneis, G. Kresse, Y. Hinuma, and F. Oba, *Phys. Rev. Lett.* **112**, 096401 (2014).
- [84] P. Richet, H.-K. Mao, and P. M. Bell, *J. Geophys. Res. Solid Earth* **93**, 15279 (1988).
- [85] T. Hom, W. Kiszczek, and B. Post, *J. Appl. Crystallogr.* **8**, 457 (1975).
- [86] A. S. Cooper, *Acta Crystallographica* **15**, 578 (1962).
- [87] D. Nabok, A. Gulans, and C. Draxl, *Phys. Rev. B* **94**, 035118 (2016).
- [88] N. Marzari and D. Vanderbilt, *Phys. Rev. B* **56**, 12847 (1997).
- [89] I. Souza, N. Marzari, and D. Vanderbilt, *Phys. Rev. B* **65**, 035109 (2001).
- [90] J. I. Mustafa, S. Coh, M. L. Cohen, and S. G. Louie, *Phys. Rev. B* **92**, 165134 (2015).
- [91] D. R. Hamann and D. Vanderbilt, *Phys. Rev. B* **79**, 045109 (2009).
- [92] I. Aguilera, C. Friedrich, and S. Blügel, *Phys. Rev. B* **91**, 125129 (2015).
- [93] S. Tillack and C. Draxl, To be published .
- [94] S. Tillack, Implementation and application of maximally localized wannier functions within the (l)apw+lo method, Master's thesis, Humboldt University, Berlin, 2018.
- [95] R. Rodrigues Pela, U. Werner, D. Nabok, and C. Draxl, *Phys. Rev. B* **94**, 235141 (2016).
- [96] N. Izyumskaya et al., *Advanced Electronic Materials* **3**, 1600485 (2017).
- [97] R. Whited, C. J. Flaten, and W. Walker, *Solid State Communications* **13**, 1903 (1973).
- [98] L. Ley, R. A. Pollak, F. R. McFeely, S. P. Kowalczyk, and D. A. Shirley, *Phys. Rev. B* **9**, 600 (1974).
- [99] A. Svane et al., *Phys. Rev. B* **82**, 115102 (2010).
- [100] A. N. Chantis, M. van Schilfgaarde, and T. Kotani, *Phys. Rev. Lett.* **96**, 086405 (2006).
- [101] M. Cardona, *Solid State Commun.* **133**, 3 (2005).
- [102] F. Giustino, S. G. Louie, and M. L. Cohen, *Phys. Rev. Lett.* **105**, 265501 (2010).
- [103] B. Monserrat, G. J. Conduit, and R. J. Needs, *Phys. Rev. B* **90**, 184302 (2014).
- [104] B. Monserrat and R. J. Needs, *Phys. Rev. B* **89**, 214304 (2014).
- [105] G. Antonius, S. Poncé, P. Boulanger, M. Côté, and X. Gonze, *Phys. Rev. Lett.* **112**, 215501 (2014).
- [106] S. Botti and M. A. L. Marques, *Phys. Rev. Lett.* **110**, 226404 (2013).
- [107] F. Aryasetiawan and S. Biermann, *Phys. Rev. Lett.* **100**, 116402 (2008).
- [108] D. Åberg, B. Sadigh, and P. Erhart, *Phys. Rev. B* **85**, 125134 (2012).
- [109] T. Cheiwchanngangij and W. R. L. Lambrecht, *Phys. Rev. B* **84**, 035203 (2011).
- [110] R. Del Sole, L. Reining, and R. W. Godby, *Phys. Rev. B* **49**, 8024 (1994).
- [111] W. Chen and A. Pasquarello, *Phys. Rev. B* **92**, 041115 (2015).
- [112] M. Shishkin, M. Marsman, and G. Kresse, *Phys. Rev. Lett.* **99**, 246403 (2007).

- [113] S.-P. Gao, *Computational Materials Science* **61**, 266269 (2012).
- [114] A. L. Kutepov, V. S. Oudovenko, and G. Kotliar, *Comp. Phys. Commun.* **219**, 407 (2017).
- [115] I. Aguilera, C. Friedrich, G. Bihlmayer, and S. Blügel, *Phys. Rev. B* **88**, 045206 (2013).
- [116] P. Koval, D. Foerster, and D. Sánchez-Portal, *Phys. Rev. B* **89**, 155417 (2014).
- [117] F. Kaplan et al., *J. Chem. Theory Comput.* **12**, 2528 (2016).
- [118] H. Löfås, A. Grigoriev, J. Isberg, and R. Ahuja, *AIP Advances* **1**, 032139 (2011).
- [119] M. A. Green, *Journal of Applied Physics* **67**, 2944 (1990).
- [120] F. Nava, C. Canali, C. Jacoboni, L. Reggiani, and S. Kozlov, *Solid State Commun.* **33**, 475 (1980).
- [121] N. Naka, K. Fukai, Y. Handa, and I. Akimoto, *Phys. Rev. B* **88**, 035205 (2013).
- [122] L. S. Pan and D. R. Kania, editors, *Diamond Electronic Properties and Applications*, Springer, 2013.
- [123] Y.-N. Xu and W. Y. Ching, *Phys. Rev. B* **44**, 7787 (1991).
- [124] F. Bruneval and M. A. L. Marques, *J. Chem. Theory Comput.* **9**, 324 (2013), PMID: 26589035.
- [125] P. Liao and E. A. Carter, *Phys. Chem. Chem. Phys.* **13**, 15189 (2011).
- [126] J. E. Coulter, E. Manousakis, and A. Gali, *Phys. Rev. B* **88**, 041107 (2013).
- [127] S. Das, J. E. Coulter, and E. Manousakis, *Phys. Rev. B* **91**, 115105 (2015).
- [128] M. Bolorizadeh, V. Sashin, A. Kheifets, and M. Ford, *J. Electron. Spectros. Relat. Phenomena* **141**, 2738 (2004).
- [129] A. Yamasaki and T. Fujiwara, *Phys. Rev. B* **66**, 245108 (2002).
- [130] G. Vidal-Valat, J. P. Vidal, and K. Kurki-Suonio, *Act. Cryst. A* **34**, 594602 (1978).
- [131] V. A. Sashin, H. E. Dorsett, M. A. Bolorizadeh, and M. J. Ford, *J. Chem. Phys.* **113**, 8175 (2000).
- [132] S. Sagmeister and C. Ambrosch-Draxl, *Phys. Chem. Chem. Phys.* **11**, 4451 (2009).
- [133] E. Weniger and E. Steinborn, *Comp. Phys. Comm.* **25**, 149 (1982).
- [134] G. B. Arfken, H. J. Weber, and F. E. Harris, Chapter 16 - Angular Momentum, in *Mathematical Methods for Physicists*, edited by G. B. Arfken, H. J. Weber, and F. E. Harris, pages 773–814, Academic Press, Boston, 7th edition, 2013.
- [135] Baker George A, *Essentials of Padé approximants*, New York : Acad. Press, 1975.
- [136] H. Padé, *Annales scientifiques de l'École Normale Supérieure* **9**, 3 (1892).
- [137] H. J. Vidberg and J. W. Serene, *J. Low Temp. Phys.* **29**, 179 (1977).